

POLITECNICO DI TORINO

Master Course in Biomedical Engineering

Master Thesis

Development and characterization of the coating for stimulating penetrating microelectrodes



Candidate

Daniela Galliani

Supervisors

Prof. Danilo Demarchi

Prof. Diego Ghezzi

Co-supervisors

Ing. Gian Luca Barbruni

PhD. Adele Fanelli

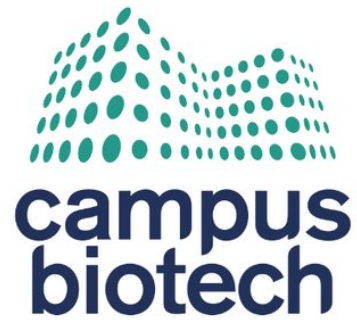
A thesis submitted in fulfilment of the requirements for the Master's degree in Biomedical Engineering Laboratory of Medtronic Chair in Neuroengineering (LNE)

October 2022

in collaboration with

ÉCOLE POLYTECHNIQUE FÉDÉRALE DE LAUSANNE
CAMPUS BIOTECH

EPFL



Abstract

In 2020, the world health organization estimated that 43.3 million people worldwide are blind. The principal causes of blindness are Retinitis Pigmentosa, Age-Related Macular Degeneration, infection, or trauma. Visual prostheses create an artificial sense of vision by stimulating the neural pathway at some point beyond the lesion site. While retinal prostheses are the most widely used, cortical prostheses offer the advantage of treating most of the blindness causes. Moreover, the cortex represents a large accessible area that allows for the placement of multiple electrodes, increasing the number of stimulation sites. Nevertheless, the system is nowadays constrained by wires which limit to one hundred the maximum number of electrodes, which leads to a reduction of the spatial selectivity of the stimulation. One possible solution to this problem can be found in the “Smart Neural Dust” concept. This cortical prosthesis is developed by using a freestanding array of thousands of individually addressable CMOS- μ electrodes for the wireless stimulation of the visual cortex.

The main goal of this master’s thesis is to develop, characterize and optimize a coating material for the commercial Pt/Ir penetrating μ electrodes used in the Smart Neural Dust system. The ultimate goal is to reduce their impedance magnitude and to increase their charge injection capacity, thus being capable to deliver $\pm 50 \mu\text{A}$ to efficiently stimulate the visual cortex.

PEDOT:PSS, IrO_x and PtBlack coatings were compared by means of cyclic voltammetry, impedance spectroscopy and voltage transient characterization. Despite PEDOT:PSS providing the highest charge injection capacity, PtBlack was chosen for its high reproducible electrodeposition process. The electrochemical performances of PtBlack coated electrodes were investigated for different exposed geometrical surface areas (GSAs) and the optimal trade-off was found in electrodes with a 75 μm tip length, leading to an overall exposed area of around 1800 μm^2 . Finally, long-term stimulation tests were performed to evaluate the electrodes stability after millions of pulses. The robustness of the electrodes was proved by means of voltage transient measurement and morphological characterization.

Despite further work is needed to optimize the coating, PtBlack offers a good coating solution for pursuing in vivo tests to validate the stimulation protocols.

Abstract

Nel 2020, l'organizzazione mondiale della sanità ha stimato che 43,3 milioni di persone nel mondo sono cieche; le principali cause di cecità sono la Retinite Pigmentosa, la degenerazione maculare legata all'età, le infezioni o i traumi. Attualmente, le protesi visive sono in grado di ricreare un senso della vista artificiale stimolando il percorso neurale a valle del sito della lesione. Nonostante, ad oggi, le protesi retiniche siano le più utilizzate, quelle corticali permettono di trattare la maggior parte delle cause di cecità. Inoltre, la corteccia presenta un'ampia area accessibile consentendo il posizionamento di più elettrodi e, di conseguenza, l'aumento del numero di siti di stimolazione. Tuttavia, il sistema è oggi vincolato da un sistema di connessione a fili che limita a cento il numero massimo di elettrodi posizionabili, il che porta ad una riduzione della risoluzione spaziale della stimolazione. Una soluzione a tale problema può essere trovata nel concetto di "Smart Neural Dust", una protesi corticale sviluppata utilizzando un array indipendente di migliaia di elettrodi CMOS indirizzabili individualmente per la stimolazione wireless della corteccia visiva.

L'obiettivo principale di questa tesi di Laurea Magistrale è sviluppare, caratterizzare e ottimizzare un materiale di rivestimento per i elettrodi commerciali a punta in Pt/Ir utilizzati nel sistema Smart Neural Dust. Lo scopo è quello di ridurre il modulo dell'impedenza e aumentare la loro capacità di iniezione di carica, essendo così in grado di fornire $\pm 50 \mu\text{A}$ per stimolare efficientemente la corteccia visiva.

I rivestimenti in PEDOT: PSS, IrOx e PtBlack sono stati confrontati mediante voltammetria ciclica, spettroscopia di impedenza e voltage transient. Nonostante il PEDOT:PSS fornisca la più alta capacità di iniezione di carica, il PtBlack è stato scelto per il suo processo di elettrodeposizione ad alta riproducibilità. Le prestazioni elettrochimiche dei elettrodi rivestiti con PtBlack sono state studiate per diverse aree di superficie geometrica (GSA) e il compromesso ottimale è stato trovato in elettrodi con una punta conduttiva di circa $75 \mu\text{m}$, che genera un'area esposta complessiva di circa $1800 \mu\text{m}^2$. Infine, sono stati eseguiti test di stimolazione a lungo termine per valutare la stabilità dei elettrodi dopo milioni di impulsi. La robustezza degli elettrodi è stata dunque dimostrata mediante la misurazione del voltage transient e la caratterizzazione morfologica.

Nonostante sia necessario un ulteriore lavoro per ottimizzare il rivestimento, PtBlack offre una buona soluzione di rivestimento per l'esecuzione di test in vivo per validare i protocolli di stimolazione.

Acknowledgements

Before proceeding with the discussion, I would like to spend a few words to thank all those who have been a huge support during these academic years and throughout this research .

First of all, I would like to express my gratitude to Professor Danilo Demarchi for giving me the great opportunity to carry out the thesis abroad and to Professor Diego Ghezzi who welcomed me in his research group and has always been available to help and advise me.

A special thanks goes to Adele Fanelli and Gian Luca Barbruni for being immensely patient and for the essential support you have shown me not only for professional matters. I would like to thank the LNE people for being welcoming, easy and nice to talk to and for always engaging in incredibly stimulating conversations.

I can't find the right words to thank my family, my mom, dad and brother, who despite all the little misunderstandings, and maybe even thanks to them, helped me grow into the person I am today, with love and respect and never judging me, letting me take the wrong decisions every now and then.

Thanks to Nonna Nunzia, Nonna Maria and Zia Anna, for being a role model showing me how to be kind and truthful. I'll always look up to you and try to learn as much as I can.

Thanks to Dennis for always being the first person I want to talk to when I'm happy or sad, making my day always at least a little bit better.

And finally, thanks to all my friends for being my family. To the old ones, because everytime we're together you remind me of how easy it is to just be myself. To the new ones, because you made this city a place incredibly easy to love and unbelievable hard to leave.

I love you all.

*To all those I love
you are the most important part of my life*

Table of Contents

List of Tables	VIII
List of Figures	IX
Acronyms	XIV
1 Introduction	1
1.1 Visual pathway	1
1.2 Causes of blindness	2
1.3 Impact of neural stimulation	3
1.3.1 Visual prostheses	4
1.3.2 Challenges of the cortical approach	4
1.4 Smart neural dust	5
1.4.1 Overview of the main project	6
1.4.2 Overview of the Master Thesis	6
2 3D μelectrodes in neural prostheses	8
2.1 Functionality of 3D μ electrodes	8
2.2 Materials for 3D μ electrodes	10
2.2.1 Metals	10
2.2.2 Silicon	10
2.2.3 Oxides and nitrides	11
2.2.4 Carbon-based materials	11
2.2.5 Conductive polymers	12
2.2.6 Hybrid composites	12
2.3 Current penetrating clinical and research probes	14
2.3.1 Stereoelectroencephalography and DBS probes	14
2.3.2 Microwires	15
2.3.3 Carbon fibers	15
2.3.4 Utah arrays	16
2.3.5 Multisite silicon arrays	17
2.3.6 Neural dust	18
3 Materials and Methods	20
3.1 Microelectrodes	20
3.2 Coating materials	21
3.2.1 PEDOT:PSS	21

3.2.2	PtBlack	22
3.2.3	IrOx	22
3.3	Electrochemical characterization	23
3.3.1	CV	23
3.3.2	EIS	24
3.3.3	Charge injection test	25
3.4	Long-term stimulation	27
3.5	Bipolar microelectrodes	28
3.6	Visual inspection	28
3.6.1	Optical microscopy	28
3.6.2	SEM imaging	29
3.7	Brain-like agarose gel	29
4	Results and discussion	31
4.1	Electrochemical characterization	31
4.1.1	Uncoated microelectrodes	31
4.1.2	PEDOT:PSS	32
4.1.3	PtBlack	33
4.1.4	IrOx	34
4.1.5	Comparison	35
4.2	Visual inspection	36
4.2.1	Uncoated μ electrodes	36
4.2.2	PEDOT:PSS	37
4.2.3	PtBlack	37
4.3	Electrode area	38
4.3.1	Uncoated microelectrodes	39
4.3.2	PtBlack	40
4.4	Comparison with current penetrating stimulating clinical and research probes	44
4.5	Bipolar microelectrodes	47
4.5.1	Electrochemical characterization	47
4.6	Visual inspection	48
4.7	Long-term stimulation	49
4.7.1	Experiment 1	50
4.7.2	Experiment 2 - Experiment 3	52
4.7.3	Experiment 4	53
4.8	Visual inspection	59
4.9	Insertion in the brain-like agarose gel	60
5	Conclusions and prospects	62
A	Matlab Codes	64
A.1	Charge Storage Capacity	64
A.2	Charge Injection Capacity	65

List of Tables

2.1	Summary of the characteristics of the materials used in neural interfaces.	13
2.2	Summary of the current penetrating devices	19
4.1	Comparison of penetrating stimulating μ electrodes.	46

List of Figures

1.1	Visual pathway [4]	2
1.2	Visual pathway parts. A) Retina [6]. B) optic nerve, optic chiasm and optic tract [7]. C) Lateral geniculate nucleus [5]. D) Visual cortex [8]	3
1.3	Age-standardized prevalence of blindness in adults aged 50 years and older from 1990 to 2020 [9]	3
1.4	Comparison of the visual field in normal conditions and pathological ones.	4
1.5	(A) Cross section of the retina showing the three different of stimulating in the retinal prostheses: 1. Epiretinal, 2. Subretinal, 3. Suprachoroidal. (B) Optic nerve prostheses. (C) LGN prostheses. (D) Cortical prostheses. [16]	5
1.6	Main project.	6
2.1	Simplified electrical circuit of the biointerface, R_m and C_m for the membrane, R_e and C_e for the electrode and R_{seal} present due to the incomplete coupling of electrode-membrane [24]	9
2.2	A) Nanostructured Pt coating deposited under DC conditions on a conically shaped probe. B) SEM image of silicon microelectrode array. C) SEM images of IrOx film after 1000 cycles of potential sweeps. D) Cross-sectional SEM image of TiN coating on Si-wafer. E) SEM images of the side view CNT fibers. F) Cross-sectional SEM image of the aligned characteristic features of graphene microfibers. G) SEM image of a top view of 3D-nanostructured BDD. H) SEM image of fabricated 3D PEDOT-based arrays. I) SEM image of a PEDOT-CNT hybrid nanocomposite. [24]	13
2.3	Typical SEEG and DBS probe [40]	14
2.4	Microwire structure [40]	15
2.5	Carbon fiber [40]	15
2.6	Utah array A) Full array, and B) Single probe with a close view of the tip [40].	16
2.7	Utah slanted array [51].	17
2.8	Multisite silicon probe [40]	17
3.1	Conductive tip GSA	21
3.2	A) Aqueous solution of 0.1 wt% EDOT and 4 wt% PSS in DI; B) Ag AgCl reference electrode on the left and Pt counter electrode on the right; C) Ivium potentiostat.	22

3.3	A) PtBlack solution; B) Precision LCR meter; C) Configuration used for electrodeposition.	22
3.4	Three-electrode configuration, starting from the left: Ag AgCl wire, working μ electrode and Pt wire.	23
3.5	Schematic diagram of the three electrodes configuration with the Ivium potentiostat to compute EIS measurements [53]	25
3.6	Schematic diagram of the three electrodes configuration with the Ivium potentiostat to compute VT measurements.	26
3.7	Cathodic first, balanced biphasic pulse at $\pm 50 \mu\text{A}$ current.	26
3.8	Stimulation protocol.	27
3.9	A) LEICA S9i; B) LEICA DVM6.	28
3.10	SEM SU5000	29
3.11	A) 0.25% w/v agarose solution in DI water and rhodamine B; B) Brain-like mold.	30
4.1	A) CV average \pm SEM of PtIr 500 k Ω μ electrodes, and B) EIS average \pm SDM of PtIr 500 k Ω μ electrodes.	31
4.2	PEDOT:PSS first attempt on 500 k Ω electrode A) CV, and B) EIS.	32
4.3	PEDOT:PSS second attempt on 500 k Ω electrode A) CV, and B) EIS.	32
4.4	Comparison between PEDOT:PSS and PtIr (500 k Ω μ electrodes) A) CV of the three μ electrodes with a close up to show in detail the first attempt of PEDOT:PSS and PtIr, B) CSC_c , C) EIS impedance and phase shift of the three μ electrodes, and D) Impedance magnitude values @ 10 Hz, 100 Hz and 1 kHz.	33
4.5	PtBlack on 500 k Ω electrode A) CV, and B) EIS.	34
4.6	Comparison between PtBlack and PtIr (500 k Ω μ electrodes) A) CV of the two μ electrodes, B) CSC_c , C) EIS impedance and phase shift of the two μ electrodes, and D) Impedance magnitude values @ 10 Hz, 100 Hz and 1 kHz.	34
4.7	A) Comparison between the CV measurements of PtIr, PtBlack and the two attempts of PEDOT:PSS 500 k Ω μ electrodes with a close up to better show the differences between PtIr, PtBlack and the first attempt of PEDOT:PSS, and B) CSC_c values.	35
4.8	Comparison between the EIS measurements (impedance magnitude and phase shift) of PtIr, PtBlack and the two attempts of PEDOT:PSS 500 k Ω μ electrodes, and B) impedance magnitude values @ 10, 100 and 1000 Hz with a close up @ 1 kHz.	36
4.9	Images of the bare μ electrode A) optical image, B) SEM, and C) SEM image to compute the area.	36
4.10	Optical images of PEDOT:PSS A) first attempt, B) second attempt, and C) third attempt.	37
4.11	Optical images of PEDOT:PSS A) first attempt, B) second attempt, and C) third attempt.	37
4.12	Optical microscope image of PtBlack coated μ electrodes.	38
4.13	SEM images of PtBlack coated μ electrodes and zoom up to 2 μm scale.	38

4.14	A) CV average \pm SEM for the four sets of PtIr μ electrodes, B) CSC_c average \pm SEM computed for the for sets of μ electrodes. C) CIC estimated as the 5% of the CSC_c	39
4.15	A) EIS magnitude curves calculated as average \pm SDM for the four sets of PtIr μ electrodes, B) EIS phase shift curves calculated as average \pm SDM for the four sets of PtIr μ electrodes, and C) Impedance magnitude values @ 1 kHz.	40
4.16	A) EIS magnitude and phase shift curves calculated as average \pm SDM for the four sets of PtIr μ electrodes, and B) Impedance magnitude values @ 1 kHz.	41
4.17	A) CV average \pm SEM for the four sets of PtBlack μ electrodes, B) CSC_c average \pm SEM computed for the for sets of μ electrodes.	42
4.18	Voltage transient measurements A) GSA of 334 μm^2 , B) GSA of 850 μm^2 , C) GSA of 1600 μm^2 , and D) GSA of 7550 μm^2	43
4.19	Voltage transient measurement with a 0 V bias.	43
4.20	Electrochemical measurements before and after linking two μ electrodes together calculated over 10 μ electrodes. A) CV, B) CSC_c , C) EIS, and D) impedance magnitude.	48
4.21) Voltage transient, and B) E_{mc} and E_{ma}	48
4.22	Visual inspection of the bipolar μ electrodes. A) Images taken with optical microscope, and B) SEM images.	49
4.23	Adjusting CV and EIS curves by eliminating the peaks. A) CV, and B) impedance magnitude.	50
4.24	CV measurement for the first long-term stimulation experiments. A) CV curves, and B) CSC_c values.	51
4.25	EIS measurements for the first long- term stimulation experiment. A) EIS magnitude and phase shift curves, and B) impedance magnitude values at 1 kHz.	51
4.26	Voltage transient measurement for the first long-term stimulation experiments. A) Voltage transient curves, and B) E_{mc} and E_{ma} values.	52
4.27	CV curves and CSC_c for the second long-term stimulation experiment. A) Stimulation μ electrode of the first pair, B) stimulating μ electrode of the second pair, and C) reference μ electrode of the second pair.	53
4.28	EIS curves and impedance magnitude values for the second long-term stimulation experiment. A) Stimulation μ electrode of the first pair, B) stimulating μ electrode of the second pair, and C) reference μ electrode of the second pair.	54
4.29	Voltage transient curves and E_{mc} and E_{ma} values for the second long-term stimulation experiment. A) Stimulation μ electrode of the first pair, B) stimulating μ electrode of the second pair, and C) reference μ electrode of the second pair.	55
4.30	Final graphs for the second and third long-term stimulation experiments. A) CSC_c , B) impedance magnitude at 1 kHz, and C) E_{mc} and E_{ma} values.	56

4.31	CV measurements for the stimulating μ electrodes of the two pairs of the fourth experiment. A) CV curves for the first pair, B) CSC_c for the first pair, C) CV curves for the second pair, and D) CSC_c for the second pair.	56
4.32	EIS measurements for the stimulating μ electrodes of the two pairs of the fourth experiment. A) EIS curves for the first pair, B) impedance magnitude values for the first pair, C) EIS curves for the second pair, and D) impedance magnitude values for the second pair.	57
4.33	Voltage transient measurements for the stimulating μ electrodes of the two pairs of the fourth experiment. A) Voltage transient curves for the first pair, B) E_{mc} and E_{ma} values for the first pair, C) voltage transient curves for the second pair, and D) E_{mc} and E_{ma} values for the second	58
4.34	Bar plot for the maximum injectable currents for stimulating and counter μ electrode for both the pairs of the fourth long-term stimulation experiment.	58
4.35	Final graphs for the fourth long-term stimulation experiments. A) Stimulating μ electrodes (1) CSC_c , 2) impedance magnitude at 1 kHz, and 3) E_{mc} and E_{ma} values), and B) counter μ electrodes (1) CSC_c , 2) impedance magnitude at 1 kHz, and 3) E_{mc} and E_{ma} values). . . .	59
4.36	SEM images. A) Before the long-term stimulation, B) stimulating μ electrode after the long-term stimulation, and C) counter μ electrode after the long-term stimulation.	59
4.37	A) Brain-like agarose gel, and B) μ electrode insertion.	60
4.38	Electrochemical measurements performed before and after the insertion in the brain-like agarose gel. A) CV curves, B) CSC_c values, C) EIS curves, and D) impedance magnitude values.	61
4.39	SEM images. A) Before the insertion in the brain-like agarose gel, and B) after the insertion in the brain-like agarose gel.	61

Acronyms

WHO

World Health Organization

IAPB

International Agency for the Prevention of Blindness

RGC

Retinal Ganglion Cells

LNG

Lateral Geniculate Nucleus

V1

Primary Visual Cortex

AMD

Age-related Macular Degeneration

RP

Retinitis Pigmentosa

ES

Electrical Stimulation

SCS

Spinal Cord Stimulator

DBS

Deep Brain Stimulator

VNS

Vagus Nerve Stimulator

SNS

Sacral Nerve Stimulator

TMS

Transcranial Magnetic Stimulator

FDA

Food and Drug Administration

CIL

Charge Injection Test

EIS

Electrochemical Impedance Spectroscopy

SEM

Scanning Electron Microscopy

BMI

Brain Machine Interface

MEA

Microelectrodes Array

SNR

Signal to Noise Ratio

GSA

Geometric Surface Area

PEDOT:PSS

Poly(3,4-ethylenedioxythiophene) Polystyrene Sulfonate

IrOx

Iridium Oxide

PtBlack

Platinum Black

DI

Deionized Water

CV

Cyclic Voltammetry

CSC

Charge Storage Capacity

CSC_c

Cathodic Charge Storage Capacity

CSC_a

Anodic Charge Storage Capacity

CIC

Charge Injection Capacity

VT

Voltage Transient

CP

Conductive Polymer

CNTs

Carbon Nanotubes

RMS

Root Mean Square

SWNTs

Single Wall Nanotubes

MWNTs

Multi Wall Nanotubes

BDD

Boron doped diamond

PPy

Poly(pyrrole)

PEDOT

poly(3,4-ethylenedioxythiophene)

PSS

Polystyrene Sulfonate

SEEG

Stereoelectroencephalography

UEA

Utah Electrode Array

USEA

Utah Slanted Electrode Array

CNS

Central Nervous System

PNS

Peripheral Nervous System

SDM

Standard Deviation

PW

Pulse Width

Chapter 1

Introduction

Vision impairment is considered to be one of the ten most widespread causes of disability [1]. In 2020, in occasion of the World Sight Day, “VISION 2020: The Right to Sight”, a joint global initiative born in 1999 between the World Health Organization (WHO) and the International Agency for the Prevention of Blindness (IAPB) which aim was to eliminate the preventable blindness cases by 2020, estimated that 43.3 million people worldwide are blind, and a significative percentage of these cases cannot be prevented [2]. Vision impairment has both a relevant personal and economic impact; adults showing vision loss have lower rates of workforce participation and productivity and higher rates of anxiety. Furthermore, alongside the increased medical care expenses, the productivity loss must be considered, which in 2018 was estimated at \$410.7 billion ppp, of which \$43.6 billion ppp was due to blindness [3].

In the fight against blindness we have different resources, such as visual prostheses. Before describing the state of the art of these prostheses it is fundamental to understand the operation of the visual system.

1.1 Visual pathway

The visual pathway, showed in Figure 1.1, refers to the ensemble of the anatomical structures responsible for the conversion of light into action potentials that can be processed by the brain, specifically by the visual cortex. generic figure The first key point in the processing of the visual stimuli is the retina, the 200 μm thick most internal membrane of the eyeball, composed of about 126 million photoreceptors cells, rods and cones, whose stimulation by the light triggers photosensitive chemical reactions generating action potentials. The stimulus then travels through neurotransmitters reaching the retinal ganglion cells (RGC) and thus the optic nerve. The optic nerve is a dense nerve, made up of more than one million nerve fibers, formed by the convergence of axons of the RGC, and it functions as a bridge that transfers the afferent pulses from the retina to the brain. Within the middle fossa the optic nerves from each eye unite to form the optic chiasm from which the same axons that originate in the RGC layers continue through the optic tract until most of them synapse with neurons in the lateral geniculate nucleus (LNG). The LNG receives both information from the retina and sends them to the primary visual

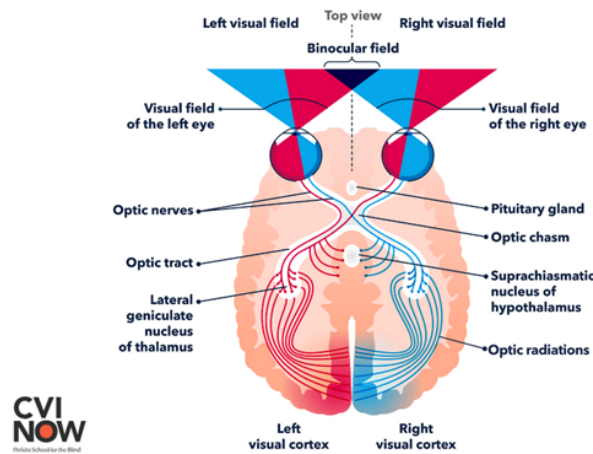


Figure 1.1: Visual pathway [4]

cortex (V1) through the optic radiations and receives many feedback connections from the primary visual cortex. The visual cortex represents 55% of the entire cortical area [5]. The main purpose of the V1 is to receive, segment and integrate visual information which is later sent to other regions of the brain in order to be analyzed. The components of the visual pathway are shown below in Figure 1.2.

1.2 Causes of blindness

By 2020, as shown in Figure 1.3, the major causes of blindness worldwide are cataract (13.4 million) and uncorrected refractive error (8 million), which combined contribute to 55% of blindness in adults aged 50 years and older [9]. Both diseases could be preventable, while among the non-preventable diseases the leading causes of blindness are age-related macular degeneration (AMD) and retinitis pigmentosa (RP).

AMD is a disease of neurosensory retina and retinal pigment epithelium responsible for more than 14% of the worldwide blindness [9] which leads to a loss of central vision [10]. The primary risk factors for AMD are age and smoking.

RP includes a set of hereditary retinal diseases that feature degeneration of rods and cones photoreceptors, starting from mid-periphery of the visual field [11]. Figure 1.4 compares the visual field in normal and pathological conditions.

New strategies are being investigated to restore vision in patients affected by retinal degeneration, such as gene therapy, optogenetics and cell transplant, but currently the only applicable strategy is the electric stimulation. Therefore, the next subchapter will focus on the working principles of neural stimulation and how it is exploited in visual prostheses.

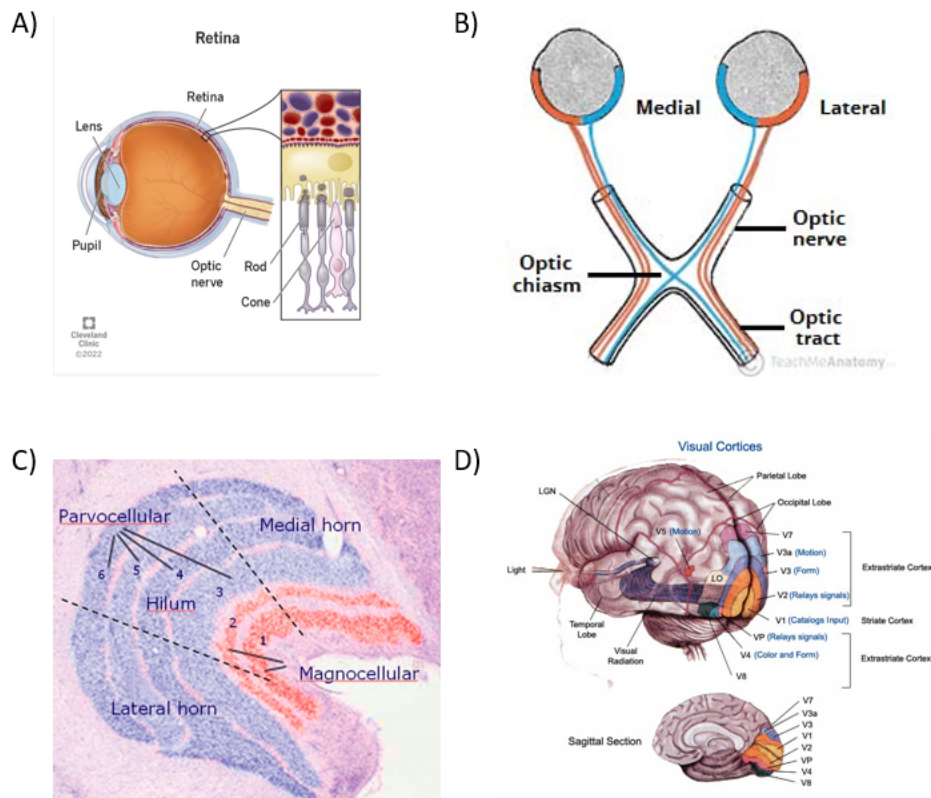


Figure 1.2: Visual pathway parts. A) Retina [6]. B) optic nerve, optic chiasm and optic tract [7]. C) Lateral geniculate nucleus [5]. D) Visual cortex [8]

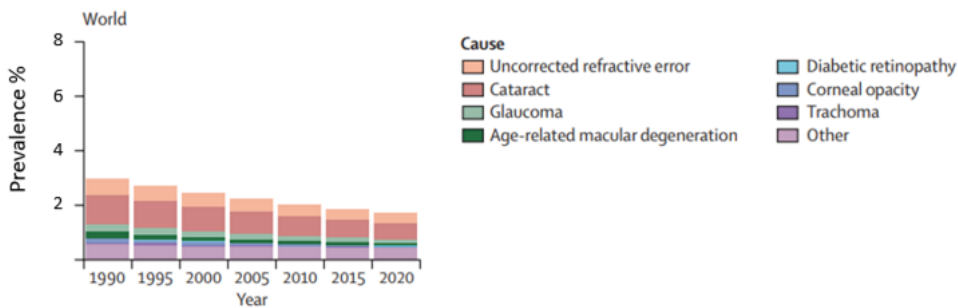


Figure 1.3: Age-standardized prevalence of blindness in adults aged 50 years and older from 1990 to 2020 [9]

1.3 Impact of neural stimulation

Neuromodulation is defined as an interventional field of medicine that alters neuronal signal transmission by implanted devices, either electrically or chemically, in order to excite, inhibit or tune the activities of neurons or neural networks to produce therapeutic effect [12]. In 1967 Shealy et al. introduced a totally implantable device



Figure 1.4: Comparison of the visual field in normal conditions and pathological ones.

using electrical stimulation (ES) in the dorsal column to treat pain, marking the beginning of the ES as we know it today [13]. The neurostimulation market can be segmented based on the product type into spinal cord stimulators (SCS), deep brain stimulators (DBS), vagus nerve stimulators (VNS), sacral nerve stimulators (SNS) and transcranial magnetic stimulators (TMS). The neuromodulation devices market is expected to grow with a CAGR of 6.5% over the forecast period of 2019-2028 [14]. Despite SCS holding the biggest share of the neuromodulation market, visual prostheses market is predicted to grow with a healthy CAGR of 10.1% during the forecast period 2019–2026 [15].

1.3.1 Visual prostheses

Since blindness can result from the alteration of one or more elements along the visual pathway, visual prostheses can create an artificial sense of vision by stimulating the neurons of the pathway at some point beyond the lesion site. As shown in Figure 1.5, it is possible to identify four different prosthetic design based on their target organ: retinal prostheses, optic nerve prostheses, lateral geniculate nucleus prostheses and cortical prostheses.

Second Sight Medical Products Inc’s Argus II Retinal Prosthesis was approved in 2011 by the European Union receiving the CE mark and in 2013 by the FDA becoming the first clinical visual prostheses [16]. Retinal prostheses are the most widely used and the most prevalent in the market. The retinal approach can only restore vision in those patients who suffer from damage of the photoreceptors, while stimulating the cortex can offer the advantage of artificial vision in most conditions of blindness. At this time, four project of cortical prostheses are in clinical evaluation: The Orion I (Second Sight Medical Products Inc), the GENNARIS (Monash Vision Group), the CORTIVIS (Miguel Hernández University of Elche), and the ICVP (Illinois University of Technology)[17]. Despite being a fascinating solution, cortical prostheses can present various drawbacks.

1.3.2 Challenges of the cortical approach

Löwenstein and Borchardt reported in a case study in 1918 that visual perception was elicited via electrical stimulation of the visual cortices of wounded soldiers who were able to see flickering light perceptions [18]. Despite cortical prostheses have come a long way, nowadays there are still several challenges that need to be addressed.

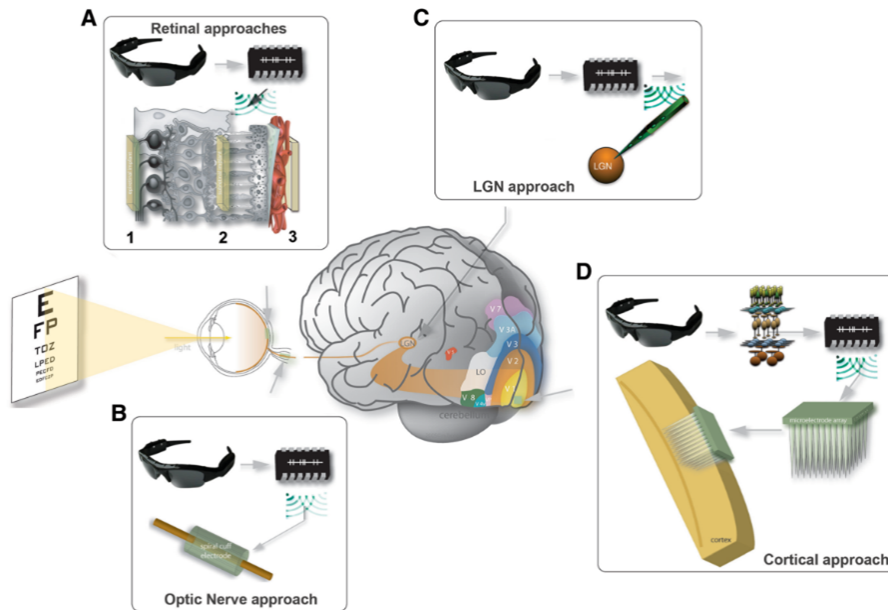


Figure 1.5: (A) Cross section of the retina showing the three different of stimulating in the retinal prostheses: 1. Epiretinal, 2. Subretinal, 3. Suprachoroidal. (B) Optic nerve prostheses. (C) LGN prostheses. (D) Cortical prostheses. [16]

Subjects testing is a crucial point of the development of a device, but, being cortical approach invasive, it is not ethical to perform visual testing on patients who show residual vision. Another dilemma when designing a cortical prostheses is the choice between surface electrodes and intracortical electrodes. While the former shows a better long-term reliability, the latter has a better spatial selectivity, and it needs a lower stimulation threshold but requires a more invasive surgery and more damage can occur to neurons due to the mechanical mismatch.

One of the major advantages of the cortical approach is the large accessible area that theoretically would allow the placement of many electrodes. Nevertheless, currently due to the presence of the wiring it is possible to place only about one hundred of electrodes reducing the spatial resolution of the stimulation.

A possible solution to some of the above-mentioned issues is embodied by the “Smart neural dust” concept.

1.4 Smart neural dust

The concept of smart dust was first reported in 1999 by J. M. Kahn, R. H. Katz and K. S. J. Pister from University of California, Berkeley, with the intent to achieve impressing performance in terms of sensor functionality and communications capabilities in a volume of a few cubic millimeters [19]. The concept of smart neural dust proved itself interesting in biological applications since the early stages. In 2013 a group of researchers from UC Berkely proposed a new brain machine interface with the name of “Neural dust” for brain monitoring [20]. In 2018 a new paper from S. Carrara and P. Georgiou followed expanding the concept as “Body dust” for the

telemetry of human metabolic conditions [21].

1.4.1 Overview of the main project

The aim of the research project in which this Master Thesis takes place is to develop a freestanding array of thousand individually addressable CMOS- μ electrodes for the wireless stimulation of the visual cortex. The whole system, as shown in Figure 1.6, is composed as follows:

1. **Video camera and image processing:** first an external camera captures the images which are processed and segmented.
2. **External base station:** RF SWIPT base station that generates, modulates and amplifies the signal. A 3-coild inductive link is used to achieve wireless power transfer.
3. **CMOS- μ electrodes:** the single miniaturized CMOS implant, placed on the visual cortex, stimulates a population of neurons to induce phosphene perception.

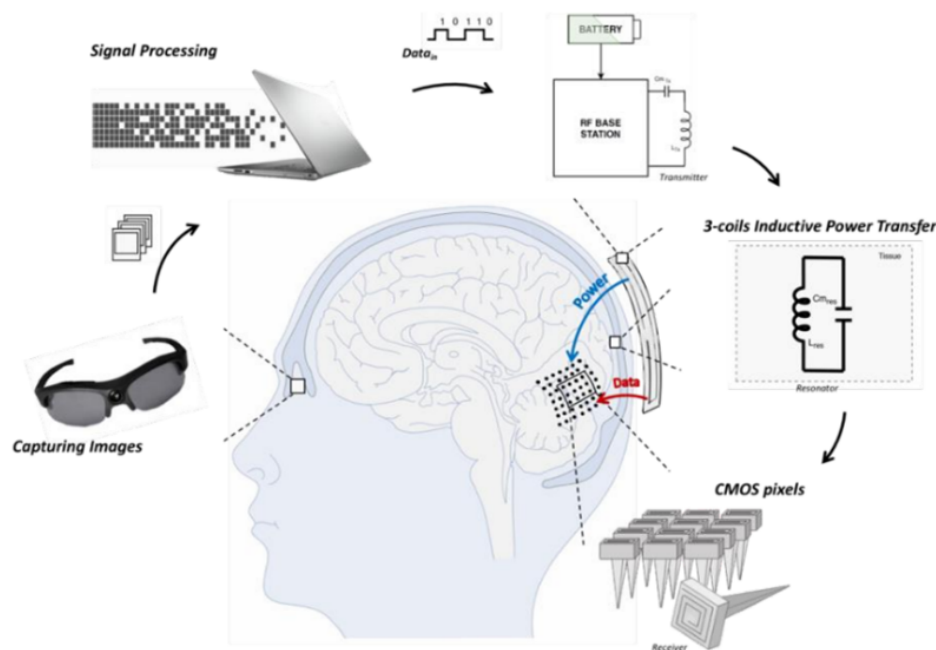


Figure 1.6: Main project.

1.4.2 Overview of the Master Thesis

The main aim of the thesis is to develop, characterize and optimize a coating material for penetrating commercial PtIr μ electrodes. The goal is to both reduce their impedance magnitude and increase their injectable charge to obtain an injectable current of $\pm 50 \mu\text{A}$ to stimulate the visual cortex [22]. The desired current is constrained by the maximum current obtainable with the implemented wireless

power transfer system, which is around 40 μA . All the tests on the coating were performed with a 50 μA current to operate within a safety margin. The target organ is the layer 4c of the visual cortex situated at 1.5 mm depth that extends for about 100 μm , constraining the maximum length of the exposed tip of the $\mu\text{electrodes}$.

Three different coating materials were compared:

1. PEDOT:PSS (poly(3,4-ethylenedioxythiophene) polystyrene sulfonate): a material widely used in neural interfaces because of its high CIC (Charge Injection Capacity) and its low Young's module which leads to a better mechanical matching with the tissue;
2. IrOx (Iridium Oxide): the most used coating material for $\mu\text{electrodes}$ characterized by this particula conical shape;
3. PtBlack (Platinum Black): a material easy to deposit, biocompatible and with good electrochemical performances.

The choice of the coating was mainly dependent on the charge injection limit (CIL) of the material and the quality of the deposition obtainable. Consecutively, the most appropriate area for the exposed conductive tip has been investigated. Once the two above mentioned parameters have been set, the $\mu\text{electrodes}$ have been linked in pairs with an interelectrode distance of about 100 μm to mimic the in vivo configuration. Long-term stimulation tests have been performed on the bipolar $\mu\text{electrodes}$ to test their stability when stimulated by multiple trains of pulses. Furthermore, the $\mu\text{electrodes}$ were observed through both optical and SEM imaging. Finally, electrochemical measurements and SEM (Scanning Electron microscope) imaging were performed before and after the insertion of the $\mu\text{electrodes}$ in a brain-like agarose gel to test the adhesion of the coating to the tip.

Chapter 2

3D μ electrodes in neural prostheses

Neuroprosthetics is a branch of neuroscience focused on the development of devices known as brain-machine interface (BMI) to either restore a lost neural function, as in visual prostheses, or to decrease the effect of an impairing condition, such as Parkinson's disease or epilepsy. One of the most critical components of a BMI is the μ electrode array (MEA) which role is to act as an interface between the neural tissue, i.e., the neurons, and all the electronics behind. Neural μ electrodes can have two purposes: to record neural signals with high signal to noise ratio (SNR) and to stimulate the neurons.

Neural recordings prove useful to develop prostheses that could provide cognitive control and to determine the output of implanted stimulating μ electrodes, such as in adaptive DBS. In recording μ electrodes it is crucial to achieve both good spatial resolution and sensitivity to be able to detect small potential changes. To do so the area and the impedance of the μ electrodes play a key role. A wide range of materials have been used including stainless steel, tungsten, platinum, platinum-iridium, iridium oxide and PEDOT [23].

On the other hand, the clinical usefulness of stimulating μ electrodes relies on the ability to chronically provide safe levels of therapeutic stimulation. Thus, stimulating μ electrodes have to be selected based on their injectable charge, which needs to be enough to evoke the wanted response without damaging the electrode or the tissue, and their spatial selectivity.

Stimulating μ electrodes can either be of surface (2D) or penetrating (3D). The following paragraphs will concentrate on 3D μ electrodes, firstly discussing how the structure improve their functionality, next focusing on the materials and finally presenting the current penetrating clinical and research probes.

2.1 Functionality of 3D μ electrodes

A biointerface represents an interface between two systems, a living organism and an electrode, with two different communication methods. An electrode, as a nonbiological object, can inject charge using two different mechanisms: faradaic charge transfer

involving the oxidation or the reduction of some species on the electrode surface and capacitive charge transfer using the electrical double layer formed at the surface. Materials can be classified based on the mechanism through which they deliver the charge, which can be capacitive (Tantalum, Titanium nitride, AIROF), faradaic (PEDOT, IrOx, SIROF) or a combination of the two, defined as pseudocapacitive (platinum, platinum-iridium). Considering the two mechanisms, the biointerface composed by an electrode, a membrane, and the cleft, is represented by an electrical circuit in Figure 2.1.

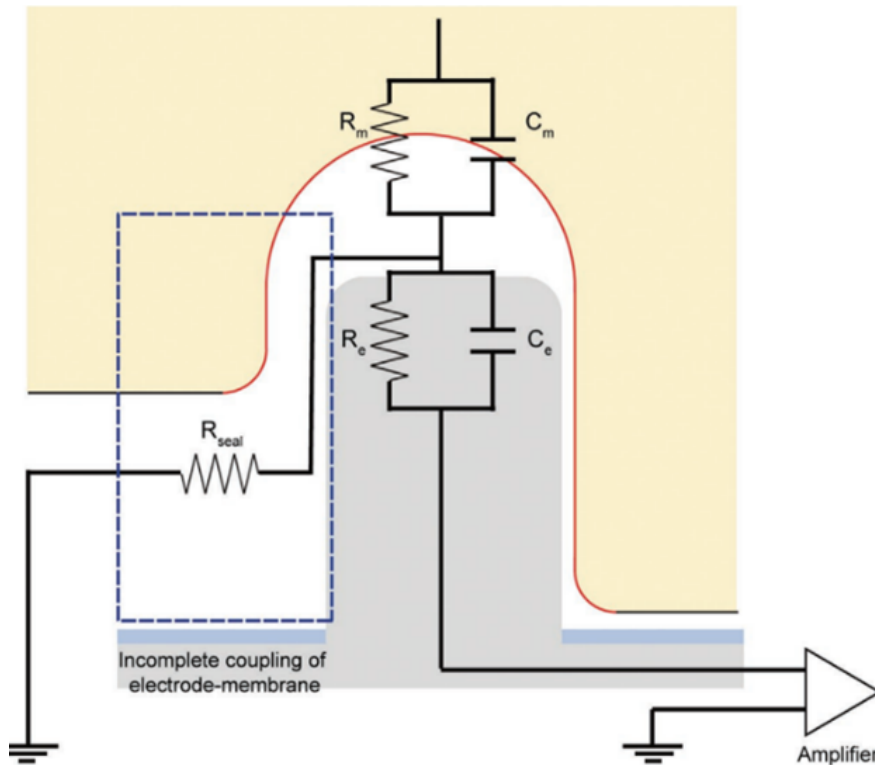


Figure 2.1: Simplified electrical circuit of the biointerface, R_m and C_m for the membrane, R_e and C_e for the electrode and R_{seal} present due to the incomplete coupling of electrode-membrane [24]

Seal resistance, R_{seal} , is the resistance against the leakage current due to the incomplete coupling of electrode-membrane. To have an efficient biointerface communication, it is necessary to have a low electrode impedance, obtainable through a large surface area, and a high seal resistance value, obtainable through a large junction area. 2D electrodes show significant limitations in both requirements, while 3D geometry allows to increase both the area of the electrode and the area of the junction. The placement of 3D electrodes requires a more invasive surgery but it will result in an enhanced quality of the recordings, an increased spatial selectivity and decreased stimulation threshold.

2.2 Materials for 3D μ electrodes

The materials used in bioelectronics must be biocompatible, non-toxic and should evoke minimum immune response. The materials can be distinguished in inorganic (including metals, silicon, oxides and nitrides, and carbon-based materials), organic (conductive polymers) and hybrid composites. Figure 2.2 shows one example SEM image for each group of materials and Table 2.1 provides a summary of the characteristics of the below discussed materials.

2.2.1 Metals

Noble metals, such as tungsten, platinum, iridium, and gold, are widely used in neural interface owing to their chemical inertness, biocompatibility, and good electrical properties. However, metals have three major drawbacks: their high Young's modulus leads to mechanical mismatch with the tissue causing inflammation, their relatively high impedance in a biological environment, and the easy ionization occurring on the metal surface, resulting in low capability of charge injection [24]. For example, platinum has a charge injection limit of around 50-150 $\mu\text{C}/\text{cm}^2$ while the needed charge density for retinal stimulation is reported to be around 50-350 $\mu\text{C}/\text{cm}^2$ [24]. The metal surface can be modified to increase the effective surface area as a solution to these limitations. Various studies worked towards that direction. Boehler et al. increased the effective surface area of cone shaped μ electrodes by forming nanostructured platinum, resulting in an impedance which was 28 times lower than the initial value [25]. Abbot et al. deposited platinum black on a platinum electrode to add nanometer-scale roughness which resulted in a decrease of the pristine electrode impedance of approximately two orders of magnitude [26]. Another possible solution to improve the properties of the material is to create compounds by mixing two metals, such as platinum-iridium alloys.

Recently, soft bioelectronics has been investigated in order to minimize tissue damage. In this regard, attempts have been made to use liquid metals as soft bioelectrode material, i.e., gallium-based liquid metals and their alloys [24].

2.2.2 Silicon

Silicon is a biocompatible and chemically inert material with semiconductive properties. The rapid development of silicon microfabrication technology, such as surface and bulk micromachining techniques, has made it possible to use it as a material for 3D bioelectronics. Exploiting the crystallinity of silicon, 3D μ electrodes with sub-micrometer resolution can be formed by synthesizing silicon nanowires or by anisotropic etching [24]. Yoo et al. presented a silicon-based 3D bioelectrode by epitaxially growing a $\langle 111 \rangle$ direction single crystal silicon nanowire on a Si (111) wafer [27].

Similarly to metals, silicon has a high Young's modulus (165 GPa), comparable to that of platinum, which causes mechanical mismatch with the tissue provoking inflammation. On the other hand, a rigid material is easier to insert during the surgery.

2.2.3 Oxides and nitrides

During bioelectrical recordings, there is a charge transfer from the tissue to the electrode making it unlikely for irreversible reactions to happen. Recording electrodes are limited mainly by their impedance. On the other hand, during neural stimulation the charge transfer happens from the electrode to the tissue, increasing the probability to have irreversible reactions. To avoid this, one possible solution is to coat the bare electrode with an iridium oxide (IrOx) layer. The thin film of IrOx formed on the metal surface undergo a valence change between Ir³⁺ and Ir⁴⁺, increasing greatly the ability to inject charge by reversible faradaic reactions [23]. Other two examples of oxides are tantalum oxide (Ta_2O_5) and titanium oxide (TiO_2).

Titanium nitride (TiN) is an electrically conductive oxide deposited by sputtering that presents a high effective surface area and a CIL comparable to that of IrOx [24].

2.2.4 Carbon-based materials

Carbon-based materials, such as CNT_s , graphene and diamond, can be synthesized into small, 3D structures characterized by mechanical flexibility, strength, anticorrosive properties, electrochemical inertness, and electrical conductivity, making them suitable for neural interfaces.

CNT_s can be used in neural interfaces, both as single-wall CNT_s ($SWNT_s$) and multiwall CNT_s ($MWNT_s$). Being standard CNT_s prepared in vacuum intrinsically fragile, for their use in Neuroprosthetics, CNT_s are prepared through layer-by-layer methods to obtain robust and durable structures. Despite their promising properties, $CCNT_s$ can cause biocompatibility issues, as reported by several studies [28] [29]. To overcome this problem and still maintain their interesting properties, surface coatings can be used.

Graphene is an interesting material in Neuroprosthetics because, in addition to the properties that it has in common with the other carbon-based materials, it shows a large specific surface area that can be easily functionalized and be fabricated with straightforward and inexpensive methods. An example of the suitability of graphene for μ electrodes array (MEA) is given by the work of Wang et al. who developed a thin $1 \mu m^2$ platinum-coated porous graphene fiber with low impedance (8.7 M) and high CIL ($\sim 10 mC/cm^2$ [30]. Park et al. fabricated a transparent graphene bioelectrode useful in optogenetic applications [31].

Diamond presents minimum cytotoxicity and through CVD methods it is possible to grow it as micro or nanocrystalline coating. Unfortunately, diamond has a large band gap making it an electrical insulator. To make it suitable for neural prostheses applications, diamond materials have been doped with boron, resulting in a p-type semiconductor. This boron-doped diamond (BDD) has been used, for example, by Piret et al. to develop 3D nanostructured electrodes used for the recording of the electrophysiology of hippocampal cells [32].

2.2.5 Conductive polymers

Mechanical mismatch between the tissue and the electrode is a major inconvenience mostly when talking about long term recording and stimulation, and foreign body response. To minimize the mismatch the Young's modulus of the material used for the electrodes needs to be as close as possible to that of the tissue; this is possible using polymers. Polymers can be used both for substrate or isolators, as polyimide or Parylene, and for electrodes, as conductive polymers (CP_s).

CP_s can transfer charge by both ionic and electronic mechanisms, and it is possible to incorporate dopants to enhance their conductivity. The most used CP_s in bio-electronic are poly(pyrrole) (PP_y) and poly(3,4-ethylenedioxythiophene) (PEDOT) [33], while the most used dopants are poly(styrene sulfonate) (PSS), paratoluene sulfonate and a range of perchlorate ions [34].

PPy is coated easily through electrodeposition and increases the electrode's surface area and its electrical conductivity, although, unfortunately, is not suitable for long term application because it can show signs of loss of electrochemical activity [24]. PEDOT is a valid alternative since it presents a high electrical conductivity and a superior electrochemical stability. PEDOT is often seen in combination with PSS, as in the study of Zhang et al. and Yuk et al. [35],[36].

2.2.6 Hybrid composites

The new frontier of biointerface is to develop μ electrodes with increased stability, improved biological responses and mechanical matching while maintaining their functionality. In this context, the surface of inorganic material electrodes can be easily modified using organic components. Composites can be fabricated by dual combinations of hydrogels and all the materials above discussed. Below several works about hybrid composites are mentioned.

Carretero et al. fabricated an electrode made by IrOx and carbon nanotube (CNT) reaching a root mean square (RMS) value of surface roughness 100 times greater than the RMS roughness of the single IrOx [37].

Ferlauto et al. developed a PEDOT:PSS/Alginate microelectrodes characterized by low impedance and high CIC [38].

Hydrogels can be also used to reduce reactive responses to CNT_s interfaces, in this regard $SWNT_s$ have been combined with a matrix of PEDGMA obtaining electrodes with optimal adhesion properties and good electrochemical performances [39].

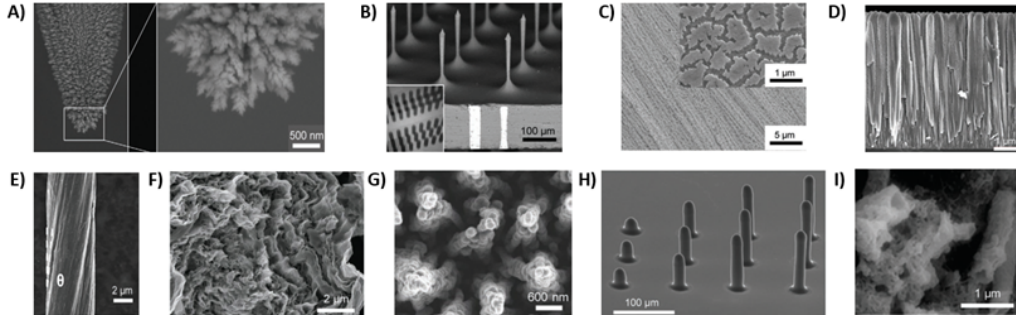


Figure 2.2: A) Nanostructured Pt coating deposited under DC conditions on a conically shaped probe. B) SEM image of silicon microelectrode array. C) SEM images of IrOx film after 1000 cycles of potential sweeps. D) Cross-sectional SEM image of TiN coating on Si-wafer. E) SEM images of the side view CNT fibers. F) Cross-sectional SEM image of the aligned characteristic features of graphene microfibers. G) SEM image of a top view of 3D-nanostructured BDD. H) SEM image of fabricated 3D PEDOT-based arrays. I) SEM image of a PEDOT–CNT hybrid nanocomposite. [24]

Material	Charge transfer mechanism	CIC [mC/cm^2]	REF.	
Metals	Pt	Faradaic/Capacitive	0.05-0.15	[23]
	PtIr			
Oxides and Nitrides	SIROF	Faradaic	1-5	[23]
	AIROF	Faradaic	1-5	
	TiN	Capacitive	~1	
Carbon-based	CNT_s			[23][24]
	Graphene	Capacitive	1.6-10	
	Diamond			
CP_s	PEDOT	Faradaic	~15	[23]
	PP_y			

Table 2.1: Summary of the characteristics of the materials used in neural interfaces.

2.3 Current penetrating clinical and research probes

Below the current clinical and research probes are discussed to provide historical context and comparison. Table 2.2 provides a summary of the characteristics of the listed probes.

2.3.1 Stereoelectroencephalography and DBS probes

Stereoelectroencephalography (SEEG) and DBS probes, which typical structure is shown in Figure 2.3, are characterized by a long cylindrical shape with an outer diameter ranging from 0.86 mm to 1.27 mm, around which 4 to 10 ring-shaped electrodes with a 1.3-2.5 mm height are wrapped [40].

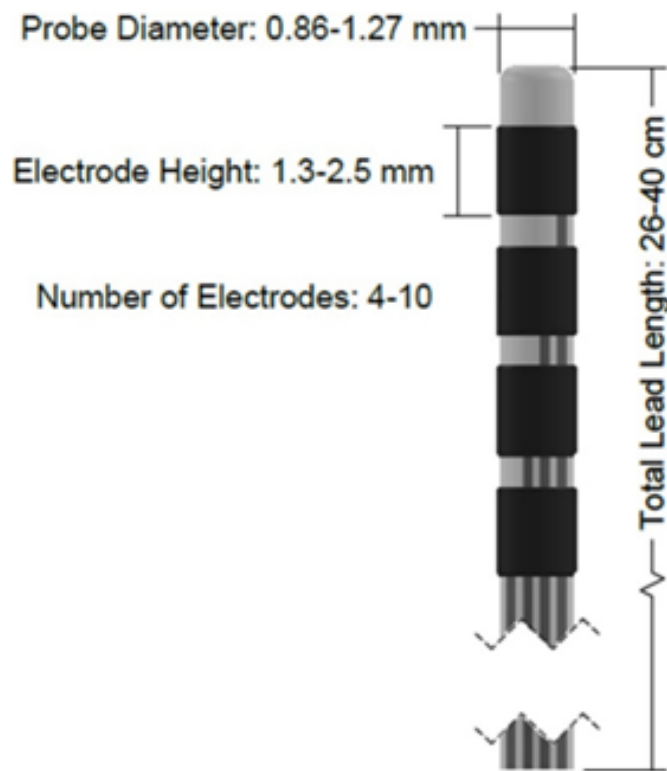


Figure 2.3: Typical SEEG and DBS probe [40]

Being a large size probe, it causes irreversible damage to the brain tissue due to its displacements [41]. Most SEEG and DBS probes are made of Pt or PtIr wires insulated by polymers. Several SEEG/DBS probes are clinically approved for various applications ranging from epilepsy diagnosis and treatment [42],[43] to treatment of movements diseases such as Parkinson's disease and essential tremors [44], [45]. Other neurological conditions, such as depression and obsessive-compulsive disorder, could benefit from the use of DBS treatments and several studies are being conducted in that way [44][45][46][47].

2.3.2 Microwires

Microwires structure, as shown in Figure 2.4, is similar to that of SEEG/DBS, a long cylindrical probe with a smaller outer diameter ranging from 25 to 80 μm [40]. Microwires are commonly made of metals, such as tungsten, Pt or PtIr, wrapped by an insulating polymer coating made of polyimide or parylene C, which leaves only the tip exposed. Each microwire is a single electrode and the small size of the conductive tip allows to record single unit signal [48]. Currently there is no commercial microwire approved, while there are some microwires with larger outer diameter used in DBS applications [40].

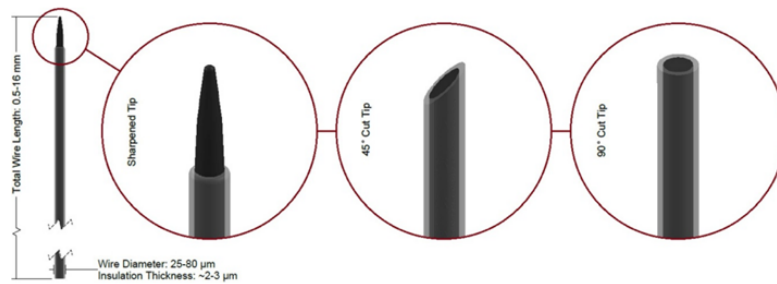


Figure 2.4: Microwire structure [40]

Several issues need to be addressed when using microwires, such as the possible insulation material failure, the metal corrosion, and the inflammation [49].

2.3.3 Carbon fibers

Carbon fibers, which structure is shown in Figure 2.5, are very similar to microwire for both the shape and the function. They are cylindrical fibers coated in glass or polymer with an exposed conductive tip with a diameter from 3.5 μm up to 40 μm [40]. Each electrode can record single units and can be assembled to obtain arrays for high density recordings.

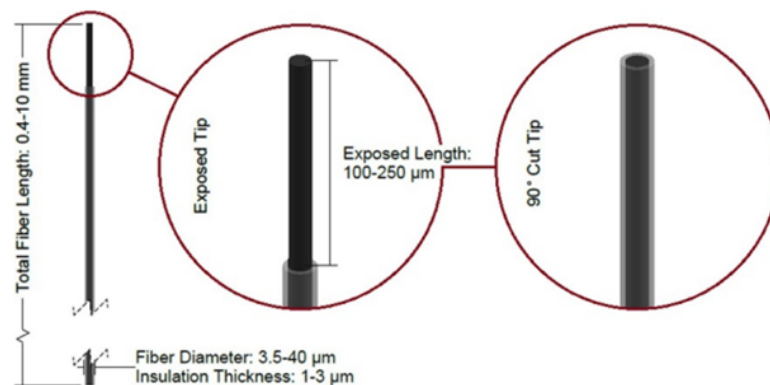


Figure 2.5: Carbon fiber [40]

2.3.4 Utah arrays

The Utah electrode array (UEA) is a silicon based neural μ electrodes array, first developed during the 1990s, in which up to 256 needles are vertically positioned on a substrate. The Neuroport array, shown in Figure 2.6, is approved by the FDA as an investigational device [50]. The platform is glass insulated and it measures 4.2x4.2 mm, the shaft is made of p-doped Si coated with parylene C and it has a diameter of 80 μ m and a length ranging from 0.5 mm to 1.5 mm for research purpose and from 1 mm to 1.5 mm for clinical purpose. The exposed tip can be coated with Pt (400 k Ω @ 1kHz) or with IrOx (50 k Ω @ 1kHz) [50].

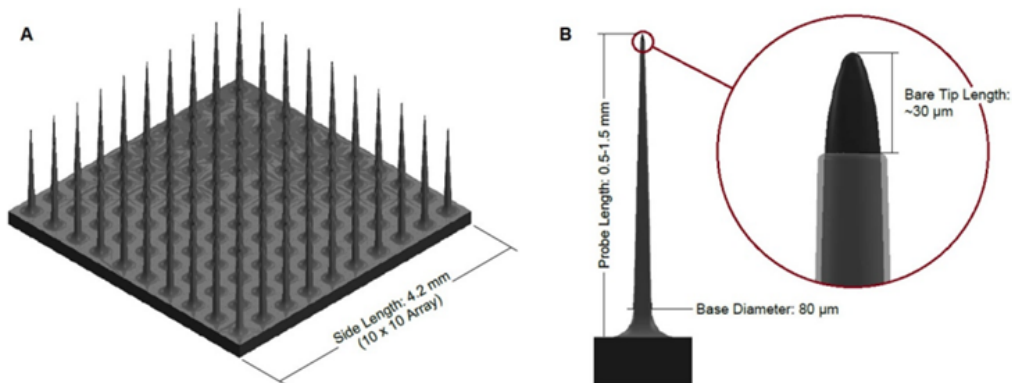


Figure 2.6: Utah array A) Full array, and B) Single probe with a close view of the tip [40].

The standard UEA is suitable for a central nervous system (CNS) interface since, being the electrodes of the same length, the conductive tips reach the same depth in the brain. On the other hand, it would be a poor choice in a peripheral nervous system (PNS) interface, which stimulation would allow to restore sensory or motor function. A valid solution to this issue is represented by the Utah slanted electrode array (USEA) shown in Figure 2.7. USEA differs from the UEA only in the length of the electrode across the array, which varies from 0.5 mm to 1.5 mm, giving access to a greater number of nerve fibers [51].

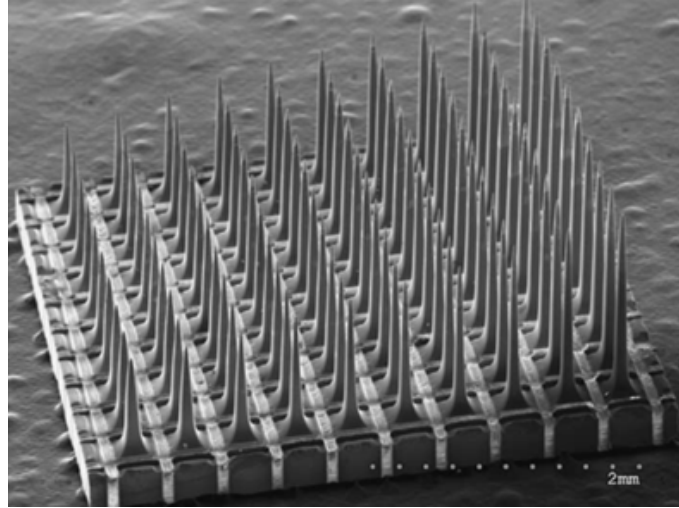


Figure 2.7: Utah slanted array [51].

2.3.5 Multisite silicon arrays

Multisite silicon array, shown in Figure 2.8, are planar probes with multiple electrodes, with a diameter ranging from 10 to 30 μm , per each shank [40]. With respect to microwires, these probes provoke an intensified immune response, which increases further if an array of probes is inserted, due to their bigger size. Currently multisite silicon arrays are used in animals, such as rodents and large mammals, but there is no device approved for human use.

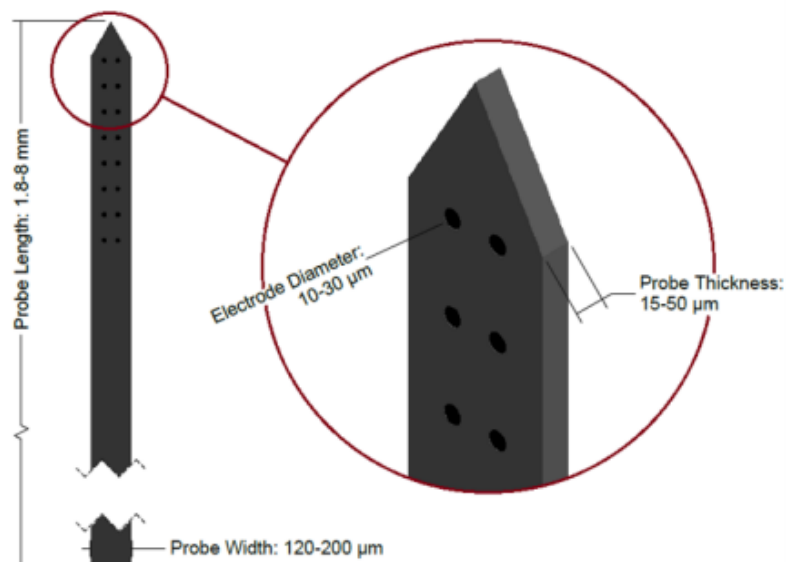


Figure 2.8: Multisite silicon probe [40]

2.3.6 Neural dust

Since the innovation brought by the neural dust technology and its characteristics have already been discussed in the previous chapter (subchapter 1.4 “Smart neural dust”), this session will report a further example of the technology. The work of D. Seo et al. was the first in vivo demonstration of a neural dust device for recording [52]. The device, which size is larger than that of the theoretical one (0.8x1x3 mm) has been implanted in the peripheral nerves of rodents, successfully recording, and reconstructing of EMG of the rodent’s sciatic nerve [52].

Probes	Shape/Size	Electrodes	Applications	FDA approved	REF.
SEEG/DBS	Cylindrical $\phi = 0.86 - 1.27\text{mm}$	ring-shaped $h = 1.3-2.5\text{mm}$	Parkinson's disease Essential tremors Epilepsy COD Depression	Yes No	[42][43][44][45] [46][47][48][49]
Microwires	Cylindrical $\phi = 25 - 80\mu\text{m}$	exposed tip	Single-unit recording High density recording	No	[40][50]
Carbon	Cylindrical $\phi = 35 - 40\mu\text{m}$	exposed tip	Single-unit recording High density recording	No	[40]
Utah array (UEA/USEA)	Needles $\phi = 80\mu\text{m}$ $h = 0.5-1.5\text{mm}$	exposed tip	CNS stimulation PNS stimulation	Yes	[52][53]
Multisite silicon array	Planar	circular $\phi = 10 - 30\mu\text{m}$	Single -unit recording	No	[40]

Table 2.2: Summary of the current penetrating devices

Chapter 3

Materials and Methods

3.1 Microelectrodes

All the used μ electrodes listed below are commercial monopolar μ electrodes purchased from MICROPROBES:

- 500 k Ω monopolar PtIr μ electrodes (PI2003.05A3) with an exposed tip of around 25 μm and an area of about 334 μm^2 ;
- 100 k Ω monopolar PtIr μ electrodes (PI2003.05A3) with an exposed tip of around 35 μm and an area of about 850 μm^2 ;
- 50 k Ω monopolar PtIr μ electrodes (PI2003.05A3) with an exposed tip of around 70 μm and an area of about 1600 μm^2 ;
- 10 k Ω monopolar PtIr μ electrodes (PI2003.05A3) with an exposed tip of around 170 μm and an area of about 7550 μm^2 ;
- Custom-made monopolar PtIr μ electrodes (PI2003.05A3) with an exposed tip of 75 μm and an area of about 1800 μm^2 ;

The electrodes are of PtIr insulated with a parylene C layer exposing only the conductive tips; on the bottom the electrode is connected to a gold pin to allow electrical connections. The geometric surface area (GSA) of the μ electrodes' tips is computed as shown below in Equation 3.1 and 3.2.

$$a = \sqrt{h^2 + (r_1 - r_2)^2} \quad (3.1)$$

$$GSA = a * \pi * (r_1 - r_2) \quad (3.2)$$

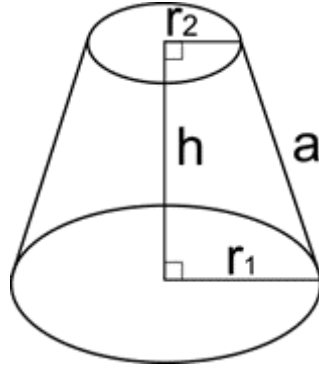


Figure 3.1: Conductive tip GSA

3.2 Coating materials

Three different coating materials, chosen based on the literature review, were investigated: PEDOT:PSS, IrOx and PtBlack.

3.2.1 PEDOT:PSS

As reported in the paper of Ferlauto et al. [38], an aqueous solution of 0.1 wt% 3,4-ethylenedioxythiophene (EDOT 97%, 483028, Sigma) and 4 wt% poly(4-styrenesulfonic acid) solution (PSS, $M_w \sim 75000$, 561223, Sigma) in deionized water (DI) was mixed by ultrasonication for 15 minutes and then mixed through vortex mixer until complete dissolution. The solution was then filtered with 0.2 μm PTFE filters (431229, Corning). The electropolymerization was obtained using a potentiostat (Compact Stat, Ivium). The μ electrodes were immersed in the PEDOT:PSS solution in a small volume with a silver/silver-chloride (Ag|AgCl) reference electrode ($\phi = 1$ mm), obtained by imposing a voltage of 1.4 V between a silver wire and a counter electrode in a 3M KCl solution, and a platinum counter electrode ($\phi = 0.25$ mm); the electropolymerization protocol was defined as follows: the potential was increased from 0.4 V to 0.9 V in 5 steps of 0.1 V and 2 seconds in duration and then it was held at 0.9 V for 40 seconds. Three attempts were made, repeating the electropolymerization protocol for a different number of times: twice for the first attempt, eleven times for the second and three times for the third. The μ electrodes were finally cured at 65 $^{\circ}\text{C}$ for 3 hours. Figure 3.2 shows all the material used.

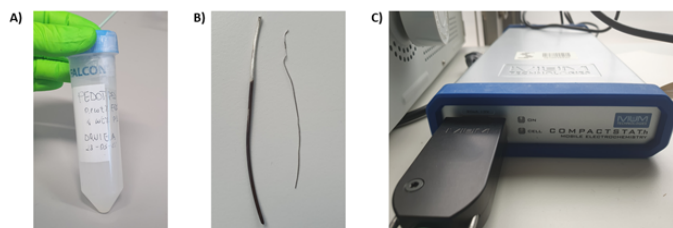


Figure 3.2: A) Aqueous solution of 0.1 wt% EDOT and 4 wt% PSS in DI; B) Ag|AgCl reference electrode on the left and Pt counter electrode on the right; C) Ivium potentiostat.

3.2.2 PtBlack

PtBlack solution is obtained by mixing 2g of Cl_6H_2Pt with 16 mg of $C_4H_6O_4Pb * 3H_2O$ in 58 g of H_2O . Deposition of PtBlack is achieved through electrodeposition using a precision LCR meter (4284A HEWLETT PACKARD). The μ electrode is immersed in the solution with a 99.9% platinum plate counter electrode for 10-15 s imposing a 700 mV potential at a frequency of 300 Hz. The μ electrodes, depending on the starting impedance magnitude, will reach a final impedance magnitude in the range of 2-12 k Ω with a coating thickness of the order of hundreds of nm (200 nm - 300 nm). Figure 3.3 shows all the material used.

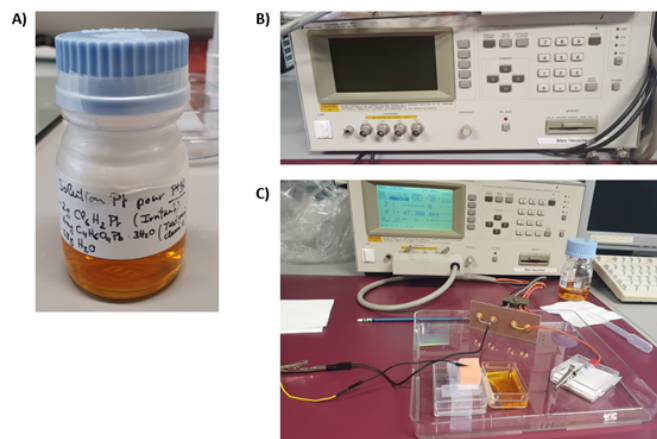


Figure 3.3: A) PtBlack solution; B) Precision LCR meter; C) Configuration used for electrodeposition.

3.2.3 IrOx

A layer of 200 nm of Iridium Oxide was sputtered on the μ electrode after the deposition of a thin layer of titanium used as an adhesion layer. The μ electrodes have a shank length of about 5 cm while the sputter can fit samples with a 2 cm maximum height, thus a single μ electrode was inserted in the sputter chamber horizontally exposing only the tip and repeating the deposition twice, turning the electrode of 180 ° after the first deposition. The process was performed in the clean room.

3.3 Electrochemical characterization

To characterize the three coating materials three different electrochemical methods have been used: cyclic voltammetry (CV), EIS and charge injection test. All the electrochemical tests were performed with Ivium potentiostat in a three-electrode cell using a Ag|AgCl wire as a reference electrode, a Pt wire as a counter electrode, with the same diameter as mention in the paragraph above (subchapter 3.2.1 “PE-DOT:PSS”), and the MICROPROBES μ electrodes as the working electrode in PBS. The three-electrode configuration is shown in Figure 3.4. A brief description of the principle of the three electrochemical methods and the parameters used will follow.

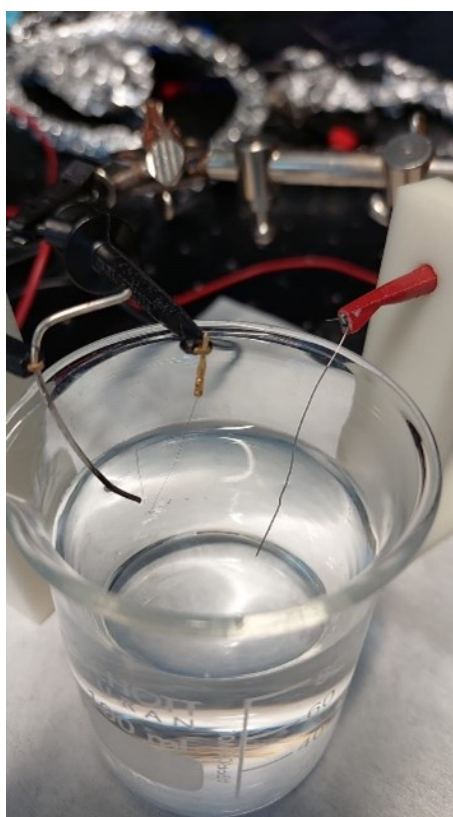


Figure 3.4: Three-electrode configuration, starting from the left: Ag|AgCl wire, working μ electrode and Pt wire.

3.3.1 CV

The CV measurements is a voltage-controlled technique in which the potential of a test electrode, compared to a noncurrent-carrying reference electrode, is swept cyclically between two voltage limits at a constant rate and the current flowing through the test and the counter electrode is measured over time. The voltage needs to remain within the limits to prevent irreversible reactions at the electrode-electrolyte interface; a common range used is the so-called water windows that is the voltage interval between the water oxidation and reduction potential calculated with respect to the chosen reference electrode, Ag|AgCl in this work. For the bare

pelectrode, i.e., PtIr, and the PtBlack and IrOx coated pelectrodes the water window is -0.6 V and 0.8 V, while for PEDOT:PSS coated pelectrodes is -0.9 V and 0.6 V [23]. There are two main reasons for which the CV is calculated in this work: first it gives insights about the presence of electrochemical reactions happening and provides information about the reversibility of these reactions, secondly charge storage capacity (CSC) can be calculated from the CV curve. The CSC, as shown in Equation 3.3, is calculated as the time integral of either the cathodic current, known as the cathodic charge storage capacity (CSC_c), or the anodic current, known as the anodic charge storage capacity (CSC_a). The CSC_c , which gives an idea of the total amount of charge available for stimulation pulse, is calculated at low current density and near-equilibrium conditions. The charge injection capacity (CIC) could be 5% to 20% of the CSC_c .

$$CSC = \frac{\int |Currentdensity|d(Voltage)}{sweep\ rate} \quad (3.3)$$

When comparing CV measurements, the fact that this method is highly dependent on the sweep rate, the GSA and the roughness of the electrode must be considered. For all the CV measurements performed in this work a speed rate of 50 mV/s was used. The Ivium potentiostat records 6 cycles for each CV measurement, the first cycle is not considered and the average value of the remaining five is calculated.

3.3.2 EIS

EIS measurements are usually of great interest concerning recording electrodes since a low impedance magnitude results in a higher SNR. Despite not having the same relevance for stimulating electrode, EIS measurements still help provides a complete picture of the electrochemical properties of the coatings, thus they are included in this work. Furthermore, it needs to be considered that a stimulating electrode with lower impedance magnitude requires lower supplied voltage to inject a certain amount of charge. EIS is performed by applying a sinusoidal voltage between the test and the counter electrode and measuring the current flowing between the test and counter electrode and the voltage between the test and the reference electrode over a broad frequency range (1 Hz - 10^5 Hz). In this way impedance magnitude and phase shift are computed. Figure 3.5 shows the schematic diagram of the configuration used for EIS measurements.

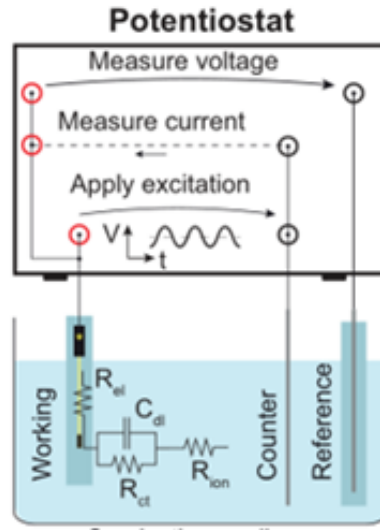


Figure 3.5: Schematic diagram of the three electrodes configuration with the Ivium potentiostat to compute EIS measurements [53]

3.3.3 Charge injection test

The charge injection test is used to estimate the maximum charge that can be injected in a current- controlled stimulation pulse; to do so the voltage transient (VT) method is used. In Figure 3.6 the schematic configuration for VT measurements is shown: a current pulse is applied between the test and counter electrode and the voltage fall between the test and the reference electrode is measured. The parameters of interested obtainable from this measurement are the most negative (E_{mc}) and the most positive (E_{ma}) polarization across the electrode-electrolyte interface. For a stimulation pulse to be safe, those limits potential cannot exceed the water electrolysis window as defined above (subparagraph 3.3.1 “CV”); going above these limits could damage both the electrode and the tissue. E_{mc} and E_{ma} are calculated by taking the voltage value 10 μ s after the cathodic and the anodic phase respectively.

VT method present several limitations in the determination of CIC, in the specific case of 3D penetrating electrodes three major limits can be identified:

- CIC is highly dependent on the current density; thus, the measurements should be performed at each current density of interest;
- The potential measured is an average across the whole surface, but the tip of the electrode will be at more extreme potentials;
- An additional nonuniformity in potential can happen through the coating thickness.

The CIC is computed by performing the VT by stimulating with a certain pulse at increasing current until either the E_{mc} or E_{ma} exceed the water window’s limits. The stimulation pulse, of which parameters are listed below, is shown in Figure 3.7:

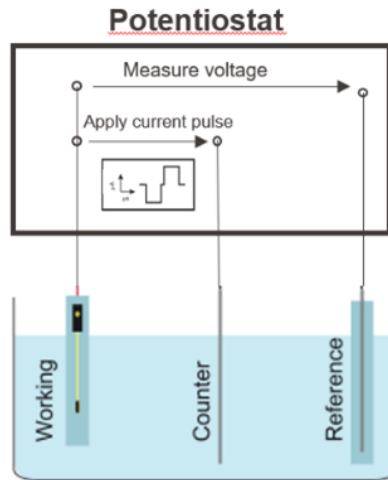


Figure 3.6: Schematic diagram of the three electrodes configuration with the Ivium potentiostat to compute VT measurements.

- Pulse width (PW) = 300 μs ;
- Frequency = 1 kHz;
- Interpulse = 20 μs ;

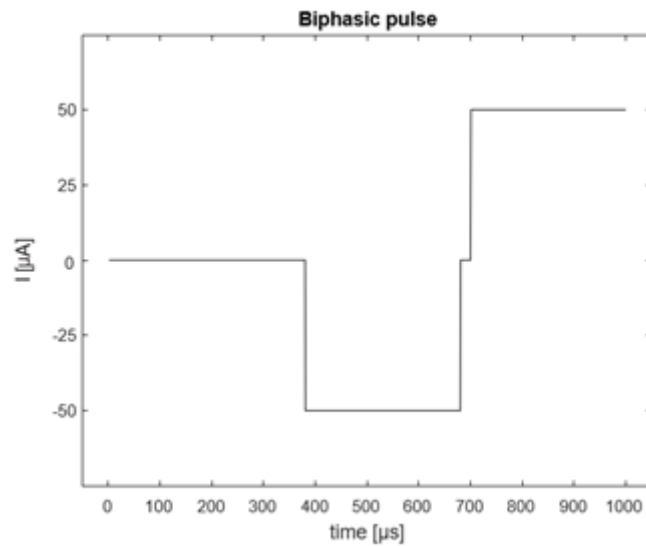


Figure 3.7: Cathodic first, balanced biphasic pulse at $\pm 50 \mu\text{A}$ current.

Equation 3.4 shows the formula to calculate CIC.

$$CIC = \frac{I * PW}{A} \quad (3.4)$$

3.4 Long-term stimulation

The long-term stimulation test has been performed using a stimulator (STG4002 Multichannel system) to stimulate the test electrode with a protocol in which the basic biphasic stimulus showed in the paragraph above (subchapter 3.3 “Charge injection test”) is repeated 7 times with a 10 Hz frequency, as shown in Figure 3.8. Four different long-term stimulation experiments have been carried out:

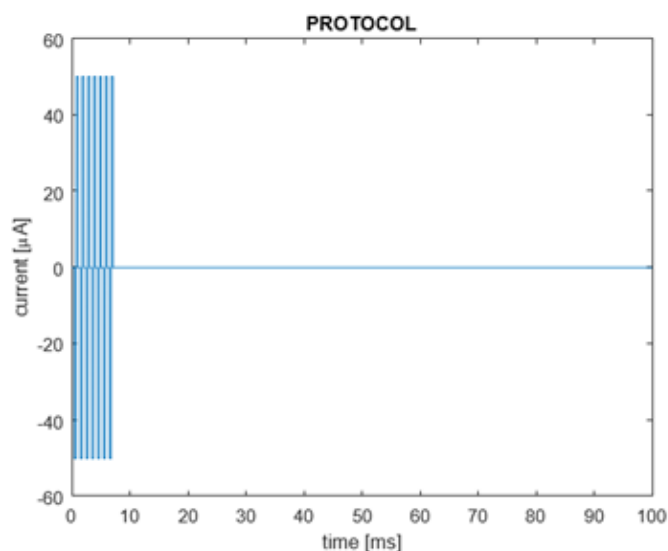


Figure 3.8: Stimulation protocol.

- Experiment 1 was performed on a single μ electrode by stimulating with a current of $\pm 50 \mu\text{A}$ for 150k train of pulses for four times resulting in 600k train of pulses;
- Experiment 2 was performed on two pairs of μ electrodes by stimulating with a current of $\pm 50 \mu\text{A}$ for 162k train of pulse for four times resulting in 648k train of pulses;
- Experiment 3 was performed on a single pair of μ electrodes by stimulating with a current of $\pm 50 \mu\text{A}$ up to 1.293M train of pulses with an intermediate step at 468k train of pulses;
- Experiment 4 was performed on two pairs of μ electrodes by stimulating for 8h/d for 5 consecutive days, with a current of $\pm 25 \mu\text{A}$ in the first case and of $\pm 50 \mu\text{A}$ in the second trial.

At each set point CV, EIS and VT measurements were acquired to monitor changes in the electrochemical properties of the coating. The stimulation happens between the test electrode and the platinum counter electrode, while for the electrochemical measurements the usual three-electrodes configuration was exploited.

3.5 Bipolar microelectrodes

For the in vivo application the monopolar μ electrodes will be cut at 1.5 mm length and they will be attached to the 200x200 μm square chip at an interelectrode distance of 75 to 100 μm . To test how the electrochemical properties of the coated μ electrodes would change, several pairs of μ electrodes were manually created. Two μ electrodes were linked under an optic microscope (LEICA S9i), by putting them at about 100 μm distance and gluing them with silicon. About 5 to 10 minutes were needed to let the silicon glue dry.

3.6 Visual inspection

Besides the electrochemical characterization of the μ electrodes, a visual inspection was performed to check the integrity of the conductive tips, the goodness of the coating and the changes in the coating after the stimulation protocol. Both optical microscopy and SEM imaging were used.

3.6.1 Optical microscopy

Two different optical microscopes have been used, both shown in Figure 3.9:

- LEICA S9i was mainly used as an aid to link two μ electrodes together;
- LEICA DVM6, a microscope with greater magnitude, used both to check the integrity of the conductive tips before proceeding with the coating and their electrochemical characterization and to do a first inspection of the coating.

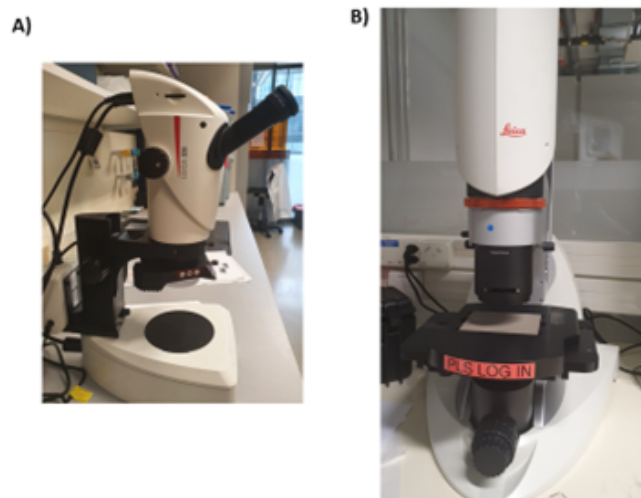


Figure 3.9: A) LEICA S9i; B) LEICA DVM6.

3.6.2 SEM imaging

SEM imaging has been performed using a SU5000, shown in figure 3.10, firstly to obtain the exact measures of the tips to compute the area for the CSC_c and the CIC calculation, then to examine in the detail the coating morphology. Below the parameters used to capture the images are listed:

- Energy = 10 keV;
- Intensity = 30 (observation mode);
- Distance of the plate = 1 mm;
- Mode = high vacuum (SE(L)).



Figure 3.10: SEM SU5000

3.7 Brain-like agarose gel

To test the insertion and the electrochemical performances after the insertion of the pelectrodes in a brain like material a brain-like agarose gel has been used. To make the brain-like agarose gel, a solution of 0.25% w/v of Agarose (Agarose standard

3810.2, Roth) in DI water underwent magnetic stirring until complete mixing and then was microwaved until bubbles were formed. Rhodamine B (R6626-25G, SIGMA) was added to obtain the pink color. The solution was poured in a brain like mold and was left overnight in the fridge to cool. Figure 3.11 shows the solution obtained and the mold used.

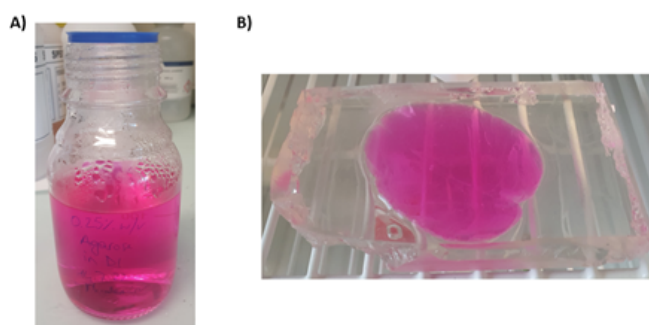


Figure 3.11: A) 0.25% w/v agarose solution in DI water and rhodamine B; B) Brain-like mold.

Chapter 4

Results and discussion

4.1 Electrochemical characterization

This chapter will report and discuss the electrochemical measurements, CV and EIS, performed on both the uncoated μ electrodes and the three coatings deposited on the $500\text{ k}\Omega$ μ electrodes (tip length of about $25\text{ }\mu\text{m}$ and area of the expose tip of about $334\text{ }\mu\text{m}^2$). A final comparison in quantitative (impedance magnitude and CSC_c) and qualitative (ease and quality of the coating process) terms will be provided in order to select the most appropriate coating material for the following steps.

4.1.1 Uncoated microelectrodes

In Figure 4.1 is shown the CV curve of the bare $500\text{ k}\Omega$ μ electrodes calculated as average \pm standard error (SEM) over 4 electrodes and the impedance magnitude and phase shift calculated as average \pm standard deviation (SDM), used as a mean of comparison.

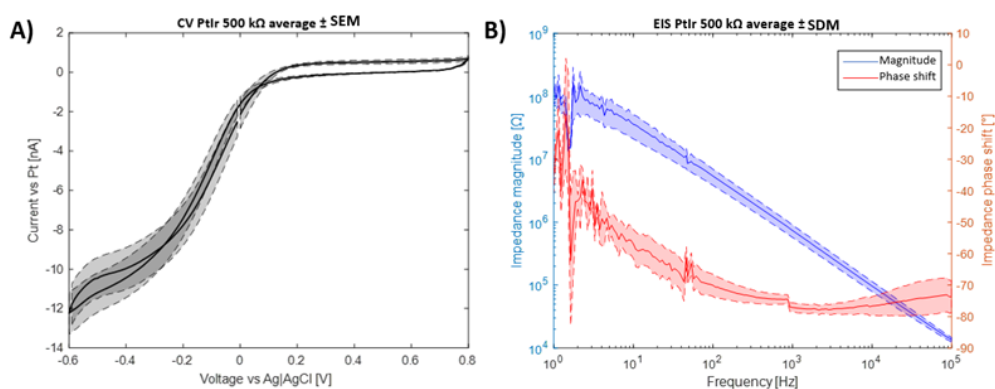


Figure 4.1: A) CV average \pm SEM of PtIr $500\text{ k}\Omega$ μ electrodes, and B) EIS average \pm SDM of PtIr $500\text{ k}\Omega$ μ electrodes.

4.1.2 PEDOT:PSS

PEDOT:PSS was deposited through electropolymerization as describes in the previous chapter (subchapter 3.2.1 “PEDOT:PSS”). Three different attempts were made, each one is singularly discussed below with a final comparison between the three:

- For the first attempt the electropolymerization was repeated twice;
- For the second attempt the electropolymerization was repeated 11 times;
- For the third attempt the electropolymerization was repeated 3 times.

Figures 4.2 and 4.3 show the CV and EIS curves for the first and the second attempt respectively, while no electrochemical measurements has been performed on the third pelectrode because of the mediocre results obtained after the electropolymerization, in which the coating was deposited on the insulated part on the pelectrode leaving the tip uncoated. As expected, given the increased repetitions of electropolymerization,

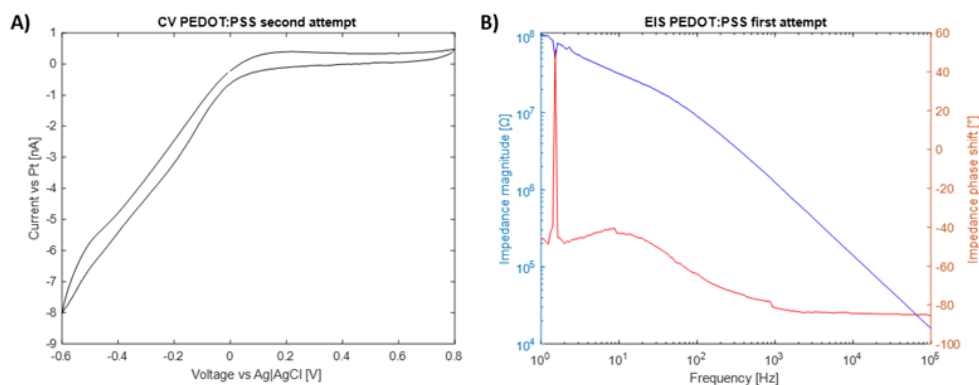


Figure 4.2: PEDOT:PSS first attempt on 500 k Ω electrode A) CV, and B) EIS.

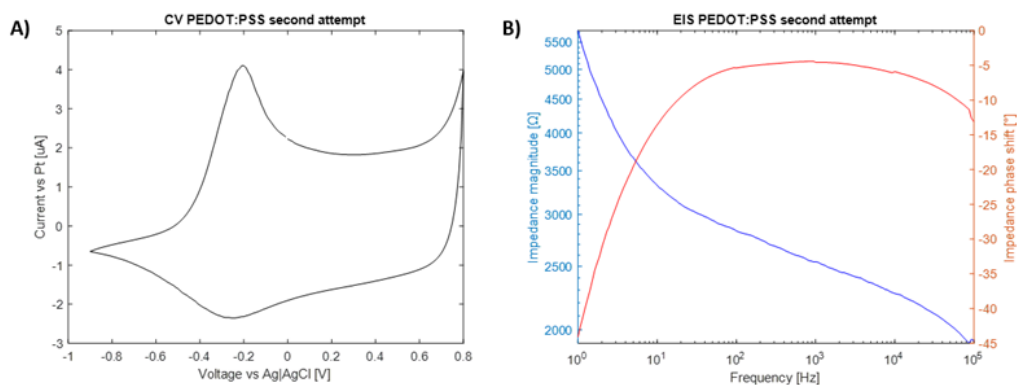


Figure 4.3: PEDOT:PSS second attempt on 500 k Ω electrode A) CV, and B) EIS.

the CV curve resulted from the second attempt is greatly larger and the decrease of the impedance magnitude is sharper. In Figure 4.4 the electrochemical measurements obtained from the two attempts are compared between them and with that of

the bare μ electrode, providing information about the values of the CSC_c and of the impedance magnitude for a quantitative comparison. PEDOT:PSS provides

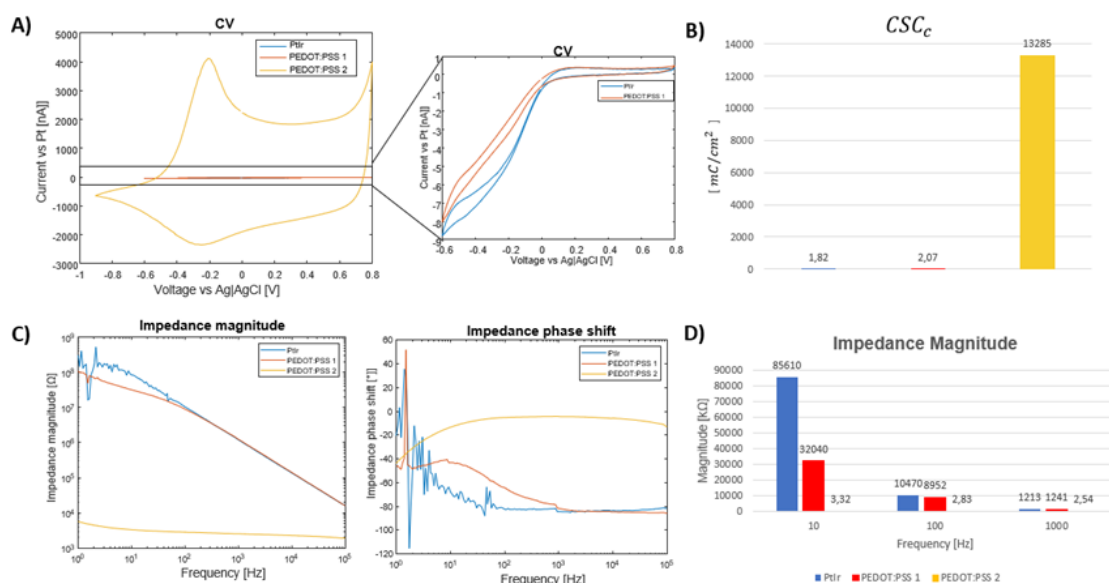


Figure 4.4: Comparison between PEDOT:PSS and PtIr (500 k Ω μ electrodes) A) CV of the three μ electrodes with a close up to show in detail the first attempt of PEDOT:PSS and PtIr, B) CSC_c , C) EIS impedance and phase shift of the three μ electrodes, and D) Impedance magnitude values @ 10 Hz, 100 Hz and 1 kHz.

advantages with respect to PtIr μ electrodes for both the CSC_c and the impedance magnitude, the extent of these advantages relies on the number of times that the electropolymerization was repeated. Despite having a slight increase in CSC_c with the first attempt of PEDOT:PSS with respect to the bare μ electrode, the improvement is not significant, and the impedance magnitudes are comparable. On the other hand, the second μ electrode coated with PEDOT:PSS gives a CSC_c greater by a factor of 10000 and an impedance magnitude at 1 kHz smaller by a factor of 1000. As the impedance decreases the noise detectable in the EIS measurements decreases too.

4.1.3 PtBlack

Only one 500 k Ω μ electrode was coated with PtBlack through electrodeposition as described in the previous chapter (subchapter 3.2.2 “PtBlack”). The results obtained from the electrochemical measurements performed are shown in Figure 4.5, while in Figure 4.6 they are displayed with that of the bare electrode and CSC_c and impedance magnitude are computed as a mean of comparison between the two. Owing to the PtBlack coating the CSC_c increases by one order of magnitude while the impedance magnitude at 1 kHz decreases by at least two orders of magnitude. The fall in impedance magnitude is not great enough to get rid of the noise detected in the EIS measurements, which is still clearly visible.

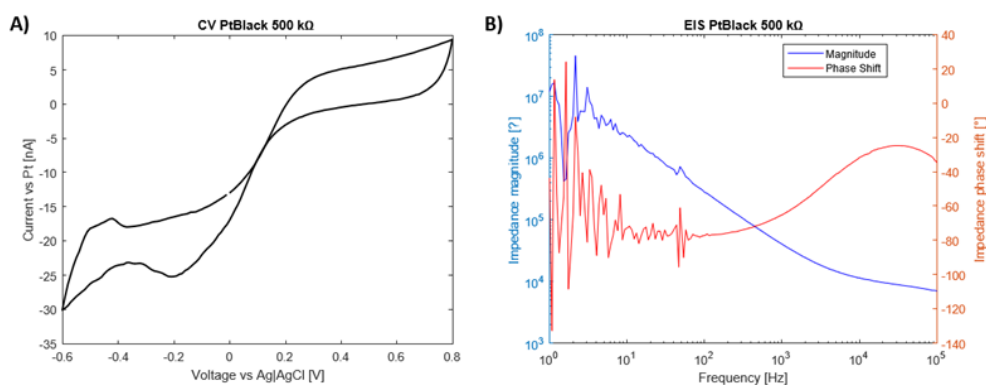


Figure 4.5: PtBlack on 500 kΩ electrode A) CV, and B) EIS.

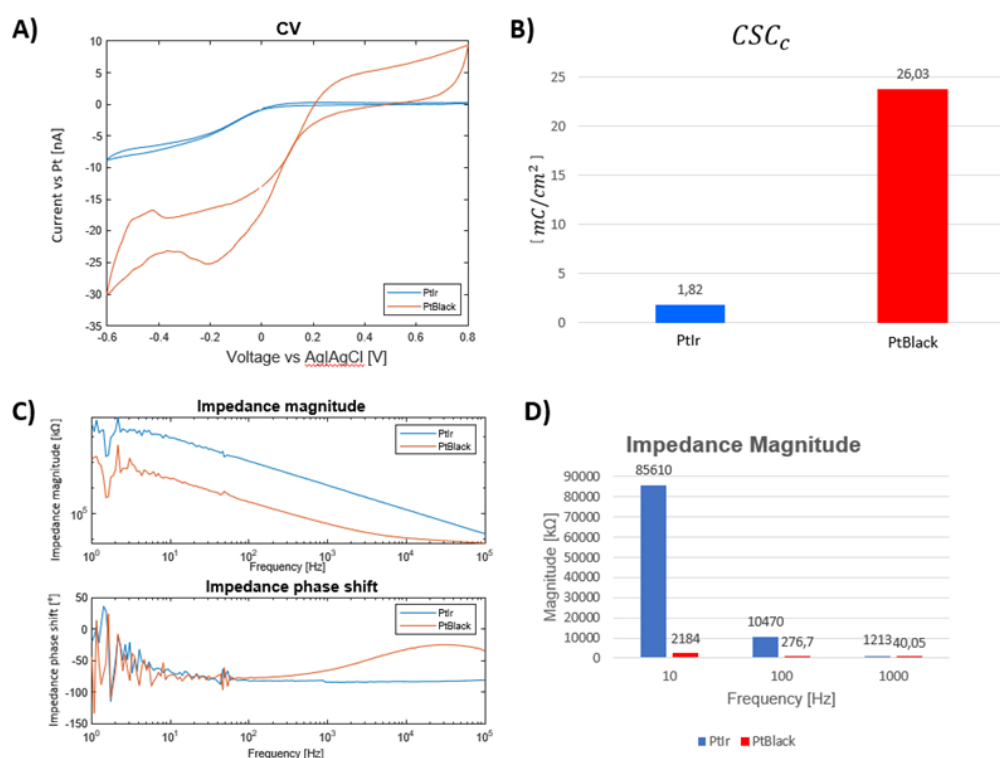


Figure 4.6: Comparison between PtBlack and PtIr (500 kΩ electrodes) A) CV of the two electrodes, B) CSC_c , C) EIS impedance and phase shift of the two electrodes, and D) Impedance magnitude values @ 10 Hz, 100 Hz and 1 kHz.

4.1.4 IrOx

Electrochemical characterization will not be provided for IrOx because it was not possible to achieve a satisfying deposition. It was possible to introduce vertically inside the sputter chamber samples with a maximum height up to 2 cm. The electrodes used in this work are 2 inches long (~5 cm), thus they could not fit vertically into the chamber. An attempt was made by placing the electrode horizontally into the chamber and repeating the deposition twice, once for each side.

The so obtained coating was uneven, with a thicker deposition on the sides of the tip, which were exposed twice. An additional problem is the difficulty of isolation of the conductive tip. A PDMS square and an aluminum foil were used to cover the length of the μ electrode, but given the small size of the tip, it was tricky to manually control the exposed part.

4.1.5 Comparison

To select the material which will be used further in this work, the electrochemical measurements of the two materials which gave successful coatings and that of the bare μ electrode are compared in qualitative and quantitative terms.

Figures 4.7 and 4.8 show CV and EIS measurements respectively, giving also quantitative information about the CSC_c and the impedance magnitude values at 1 kHz.

Concerning the impedance magnitude value at 1 kHz, PtBlack shows far better

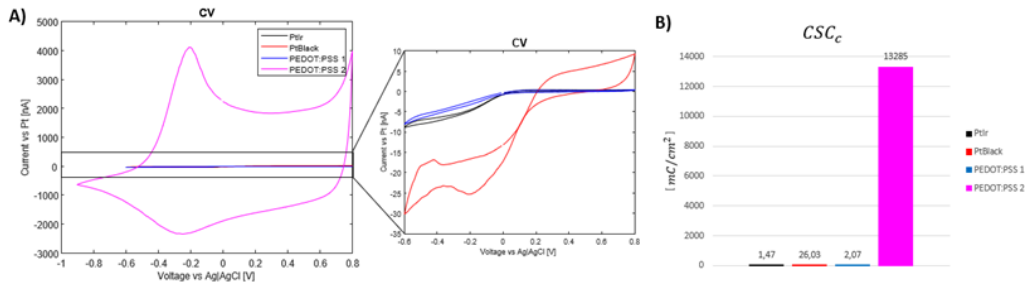


Figure 4.7: A) Comparison between the CV measurements of PtIr, PtBlack and the two attempts of PEDOT:PSS 500 k Ω μ electrodes with a close up to better show the differences between PtIr, PtBlack and the first attempt of PEDOT:PSS, and B) CSC_c values.

performances than PtIr and the first attempt of PEDOT:PSS, which impedance magnitude is higher than 1000 k Ω , reaching an impedance of 40 k Ω . The second attempt of PEDOT:PSS is the better results with the impedance magnitude going down to around 3 k Ω .

The same trend can be detected in the CV measurements. PtBlack reaches a CSC_c of 26 mC/cm^2 , one order of magnitude greater than both PtIr and the first attempt of PEDOT:PSS, which CSC_c value swing around 2 mC/cm^2 . The second attempt of PEDOT:PSS reaches a CSC_c value of over 10000 mC/cm^2 .

PEDOT:PSS and PtBlack both have qualities and drawbacks. PtBlack is characterized by an easier deposition process and provides good improvements in terms of impedance magnitude and CSC_c , but, being a stiff material, it creates mechanical mismatch when in contact with the tissue. On the other hand, PEDOT:PSS is a soft material, and it provides the highest CSC_c and the lowest impedance magnitude.

Despite PEDOT:PSS showing better electrochemical performances, the coating process is less reliable and repeatable than PtBlack electrodeposition, thus PtBlack is the material that will be used for the following steps performed in this work.

This decision will be further validated by the SEM images of the two different coatings which will be shown in the next subchapter.

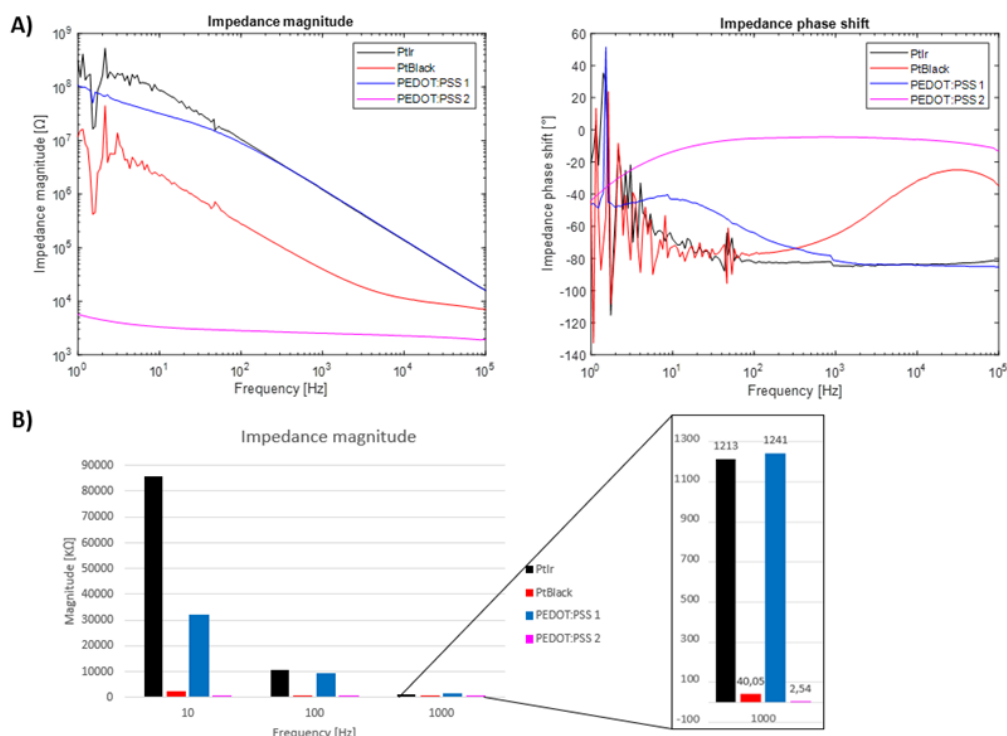


Figure 4.8: Comparison between the EIS measurements (impedance magnitude and phase shift) of PtIr, PtBlack and the two attempts of PEDOT:PSS 500 kΩ µelectrodes, and B) impedance magnitude values @ 10, 100 and 1000 Hz with a close up @ 1 kHz.

4.2 Visual inspection

To obtain a complete picture of the characteristics of the coatings, images were taken using both optical microscopy and SEM imaging.

4.2.1 Uncoated µelectrodes

Figure 4.9 shows an optical image of the uncoated µelectrode next to the SEM image of a close up of the conductive tip in PtIr and a SEM image used to highlight the dimensions used to compute the area.

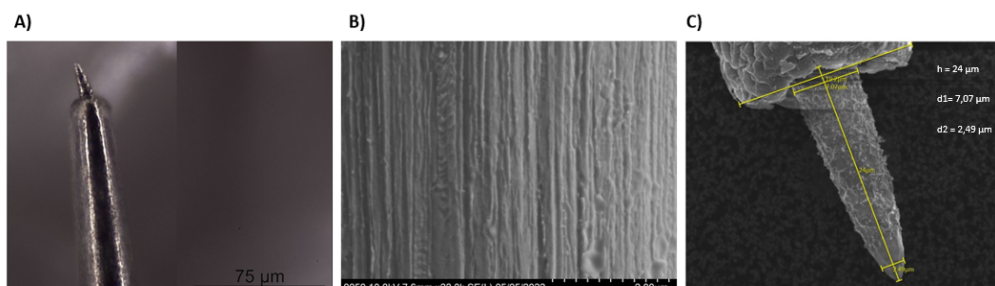


Figure 4.9: Images of the bare µelectrode A) optical image, B) SEM, and C) SEM image to compute the area.

4.2.2 PEDOT:PSS

Figure 4.10 shows optical microscope images acquired for the three attempts made for PEDOT:PSS coating. The coating is not visible in the first attempt confirming the results obtained from its electrochemical measurements, in which it showed performances comparable to that of PtIr. As mentioned in the paragraph above (subchapter 4.1.2 “PEDOT:PSS”), the third attempt failed and PEDOT:PSS deposited on the insulation. The second attempt gave the best results, but the coating is not restricted to the conductive tip and is not homogeneous, as shown more in detail in Figure 4.11 with a SEM image.

The electropolymerization of PEDOT:PSS is hard to control and to replicate.

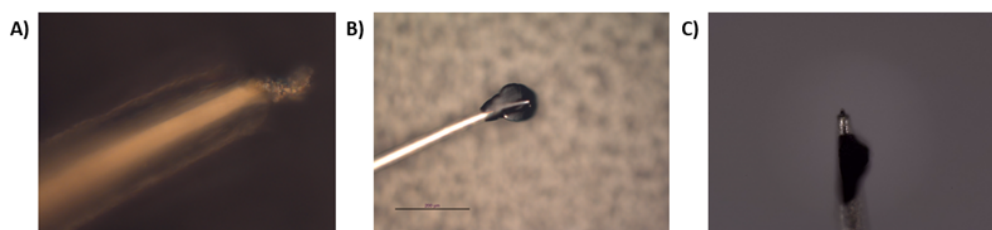


Figure 4.10: Optical images of PEDOT:PSS A) first attempt, B) second attempt, and C) third attempt.

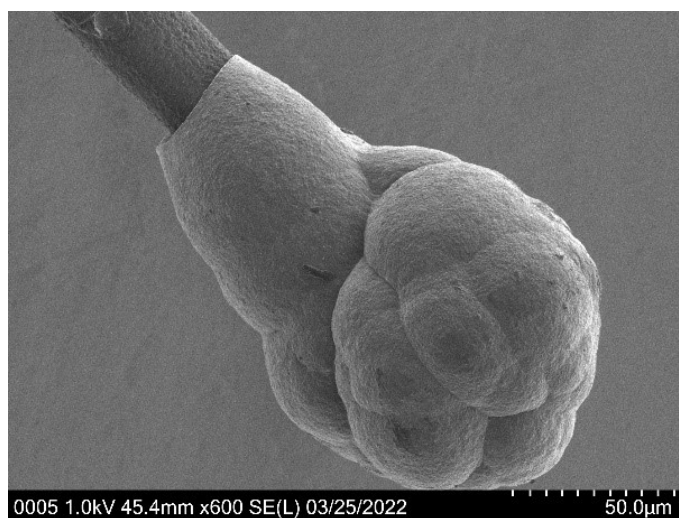


Figure 4.11: Optical images of PEDOT:PSS A) first attempt, B) second attempt, and C) third attempt.

4.2.3 PtBlack

Figure 4.12 shows the images of PtBlack captured by the optical microscope. Given the small size of the conductive tips, optical microscope images cannot be used on their own to provide a good inspection of the coating. In order to observe the coating obtained, Figure 4.13 shows the SEM images of two different PtBlack coated µelectrodes and the zoom up to 2 µm scale that highlights the cauliflower-like

nanostructures.



Figure 4.12: Optical microscope image of PtBlack coated μ electrodes.

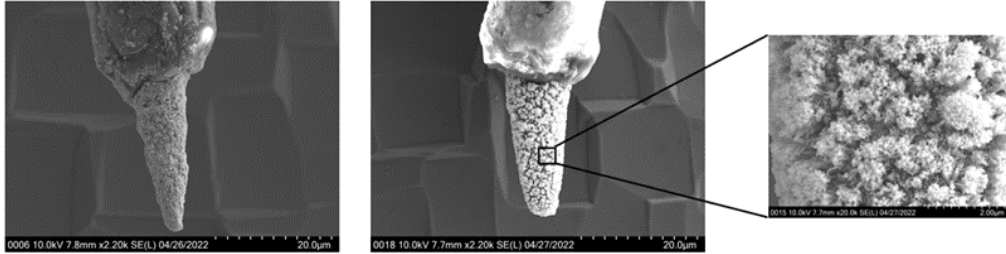


Figure 4.13: SEM images of PtBlack coated μ electrodes and zoom up to 2 μ m scale.

The SEM images show how the electrodeposition of PtBlack is repeatable and successful.

4.3 Electrode area

Having decided the coating material for the penetrating μ electrodes, the next step of this work is to compare the electrochemical performances of PtBlack coated μ electrodes with different conductive tip GSA. Four different GSA are investigated:

- GSA of $334 \mu\text{m}^2$, corresponding to a tip length of $\sim 25 \mu\text{m}$;
- GSA of $850 \mu\text{m}^2$, corresponding to a tip length of $\sim 35 \mu\text{m}$;
- GSA of $1600 \mu\text{m}^2$, corresponding to a tip length of $\sim 70 \mu\text{m}$;
- GSA of $7550 \mu\text{m}^2$, corresponding to a tip length of $\sim 170 \mu\text{m}$;

For uncoated μ electrodes CV, and EIS measurements were performed, while on PtBlack coated μ electrodes voltage transient measurement is added to the two mentioned above to accurately compute the CIC.

Firstly, a comparison between the four different GSA for uncoated μ electrodes is provided, then the same it's repeated for PtBlack coated μ electrodes to assess the influence of the coating as the area changes, and, finally, after having selected the most appropriate GSA, the electrochemical measurements before and after the coating are provided.

4.3.1 Uncoated microelectrodes

The electrochemical measurements were performed on the bare μ electrodes to have a term of comparison. Multiple uncoated μ electrodes for each impedance value were available, thus for each set of μ electrodes the average value and the standard error/standard deviation were calculated for both CV and EIS:

- Nr. 4 500 k Ω μ electrodes (tip length of ~ 25 μm , area of ~ 334 μm^2);
- Nr. 2 100 k Ω μ electrodes (tip length of ~ 35 μm , area of ~ 852 μm^2);
- Nr. 5 50 k Ω μ electrodes (tip length of ~ 70 μm , area of ~ 1600 μm^2);
- Nr. 2 10 k Ω μ electrodes (tip length of ~ 170 μm , area of ~ 7550 μm^2);

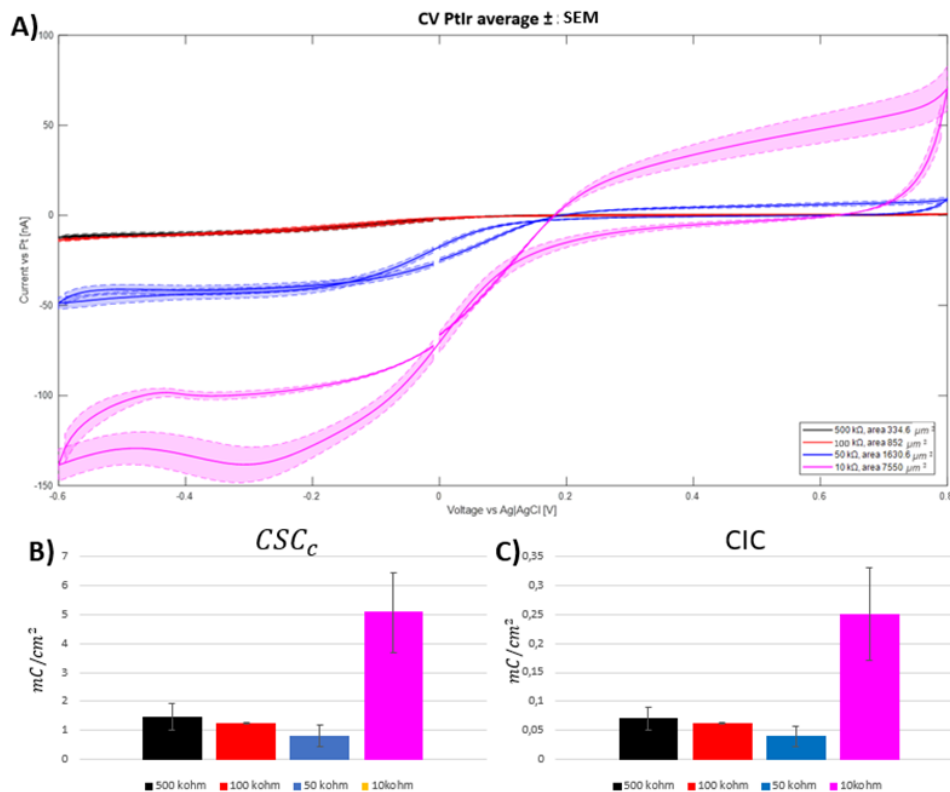


Figure 4.14: A) CV average \pm SEM for the four sets of PtIr μ electrodes, B) CSC_c average \pm SEM computed for the for sets of μ electrodes. C) CIC estimated as the 5% of the CSC_c .

In Figure 4.14 all the four curves are shown in the same plot and the CSC_c and the predicted CIC values are displayed in a bar diagram. The CV curve expands when the μ electrode area increases, reaching more extreme current values. The 500 and 100 k Ω μ electrodes are characterized by a range of current going from \sim 15 nA to \sim 1 nA, while the limits for 50 k Ω μ electrodes are -50 nA and 10 nA going up to -150 nA to 70 nA for the 10 k Ω μ electrodes.

The CSC_c does not swing significantly for the three smaller area μ electrodes settling around 0.5-1 mC/cm^2 , while that of the μ electrodes characterized by an area of 7550 μm^2 reaches 5 mC/cm^2 .

In Figure 4.15 the results obtained for the EIS measurements are shown as average \pm standard deviation. The impedance magnitude is calculated for three values of frequencies: 10 Hz, 100 Hz, and 1000 Hz, the latter being the frequency of main interest.

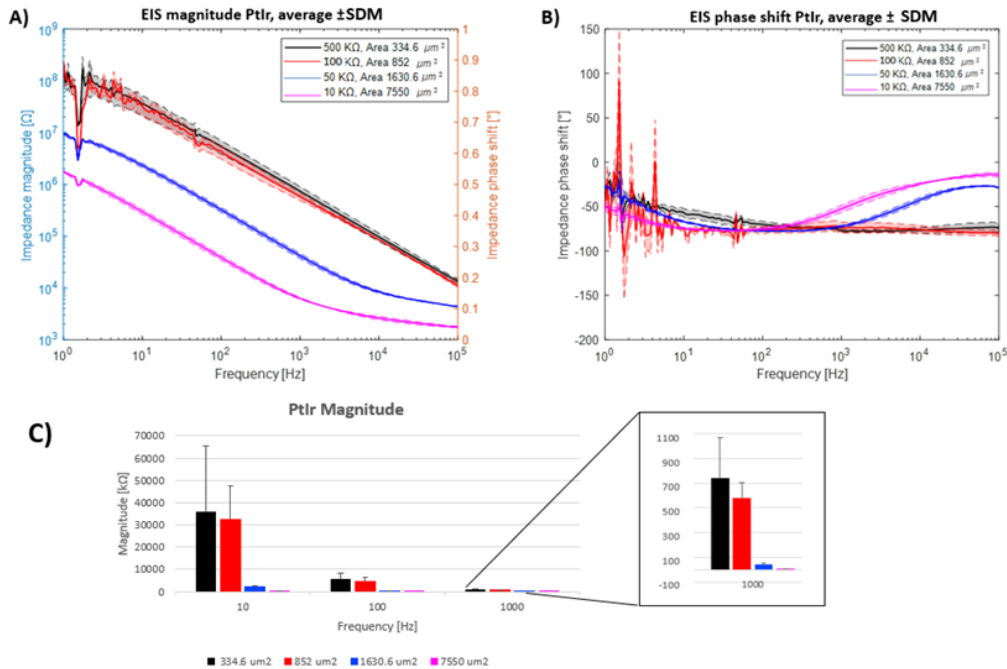


Figure 4.15: A) EIS magnitude curves calculated as average \pm SDM for the four sets of PtIr μ electrodes, B) EIS phase shift curves calculated as average \pm SDM for the four sets of PtIr μ electrodes, and C) Impedance magnitude values @ 1 kHz.

The impedance magnitude decreases as the GSA increases, with the highest gap being between 100 k Ω and 50 k Ω μ electrodes.

4.3.2 PtBlack

Multiple PtBlack μ electrodes for each impedance value were available, thus for each set the average value and the standard error/standard deviation were calculated for both the CV and the EIS:

- Nr. 1 500 k Ω μ electrodes (tip length of ~ 25 μm , area of ~ 334 μm^2);
- Nr. 2 100 k Ω μ electrodes (tip length of ~ 35 μm , area of ~ 850 μm^2);
- Nr. 5 50 k Ω μ electrodes (tip length of ~ 70 μm , area of ~ 1600 μm^2);
- Nr. 2 10 k Ω μ electrodes (tip length of ~ 170 μm , area of ~ 7550 μm^2);

First the EIS measurements will be discussed. The impedance magnitude and phase shift of the 4 μ electrodes with different GSA are displayed in Figure 4.16, together with the impedance magnitude values at 10, 100, and 1000 Hz.

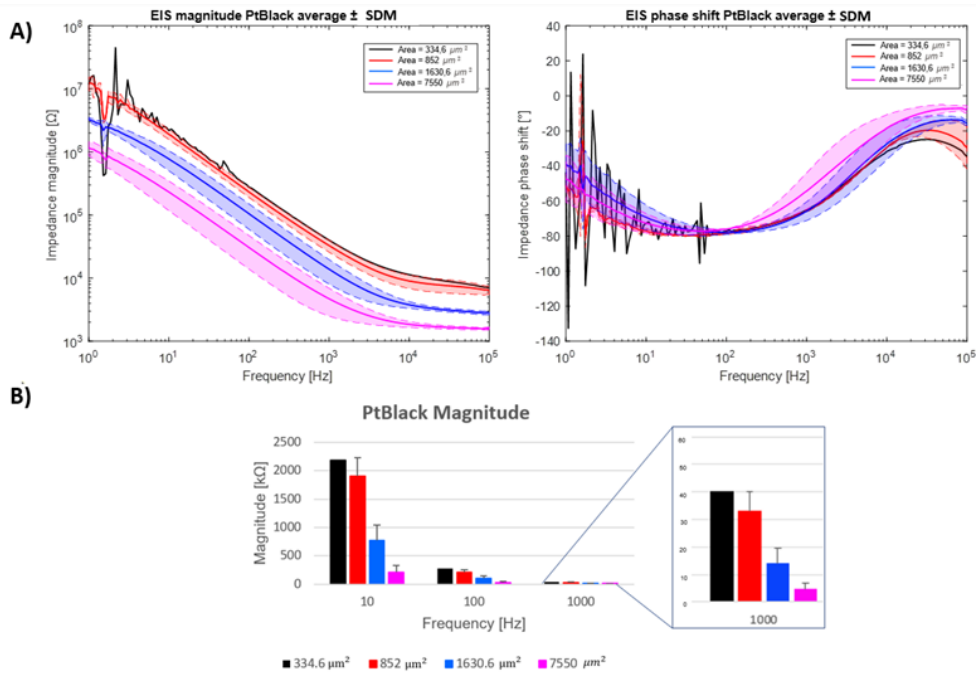


Figure 4.16: A) EIS magnitude and phase shift curves calculated as average \pm SDM for the four sets of PtIr μ electrodes, and B) Impedance magnitude values @ 1 kHz.

As the GSA increases there is a consequential decrease in the magnitude impedance, which, at 1 kHz, is about 40 k Ω for a GSA of 334 μm^2 , 30 k Ω for a GSA of 850 μm^2 , 12 k Ω for a GSA of 1600 μm^2 , and going down to 5 k Ω for a GSA of 7550 μm^2 .

Figure 4.17 shows the four CV curves on the same plot and the CSC_c values are displayed in a bar plot. As for the PtIr μ electrodes, the CV curve clearly enlarges as the GSA of the exposed conductive tip increases, but CSC_c does not follow the same trend. This is explained because the CSC_c is calculated over the area, thus its value it's not supposed to change significantly when there is an increase in GSA. The same can be said for the CIC, which is a property dependent on the material and on the pulse width. Considering a given value of CIC, increasing the area it's possible to inject a higher current, which is the parameter we are interested in.

Voltage transient measurements are performed to calculate the injectable current.

At first the measurements are performed without considering the bias, i.e., the voltage value measured respect to the Ag|AgCl reference electrode when no current is injected, to have an idea of the maximum injectable current. The results for each GSA electrode are displayed in Figure 4.18.

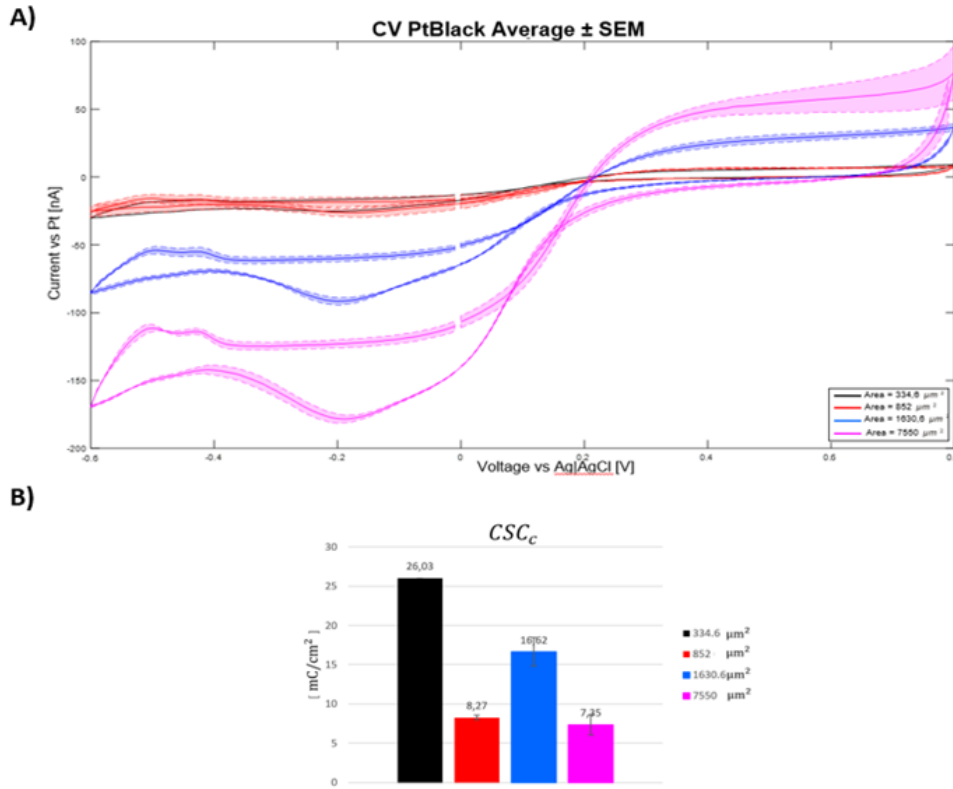


Figure 4.17: A) CV average \pm SEM for the four sets of PtBlack electrodes, B) CSC_c average \pm SEM computed for the sets of electrodes.

Increasing the area, the injectable current increase considerably. The goal is to inject a current of $\pm 50 \mu\text{A}$, thus the electrodes with a GSA of 1600 and 7550 μm^2 (50 and 10 $\text{k}\Omega$ respectively) would reach the goal, injecting 120 μA and 320 μA respectively. The target organ will be the layer 4c of the visual cortex, which is extended for about 100 μm , thus the electrode tip cannot exceed that measure. The 7550 μm^2 electrode has an exposed tip of 170 μm , making it not suitable for the application. Furthermore, proceeding with the 50 $\text{k}\Omega$ electrode would allow to obtain a stimulation with a higher spatial selectivity. Analyzing the results, it is clear that PtBlack benefits from a positive bias, but in the in vivo application the bias will not be applied. Thus, the voltage transient has been measured for the initial bias at 0 V to control if the E_{mc} and E_{ma} are still within the water window (-0.6 V 0.8V). This measurement has been performed on three custom-made electrodes (exposed tip of 75 μm and overall area of about 1800 μm^2) and their voltage transient together with the E_{mc} and E_{ma} values are shown in Figure 4.19. In each case the injectable current is above the desired one, thus the electrodes with an exposed tip of 75 μm and a GSA of 1800 μm^2 are the ones used in this work for the following steps.

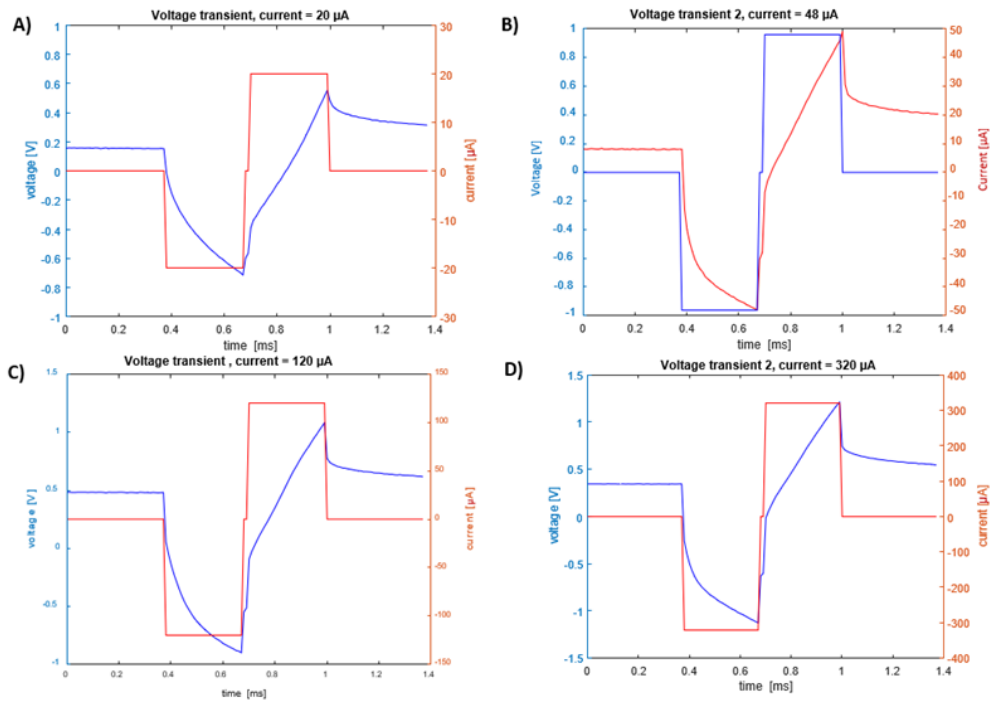


Figure 4.18: Voltage transient measurements A) GSA of $334 \mu m^2$, B) GSA of $850 \mu m^2$, C) GSA of $1600 \mu m^2$, and D) GSA of $7550 \mu m^2$.

Before proceeding with the creation of the bipolar pelectrodes and the long-term stimulation experiments, the next subsection will be dedicated to the comparison of the electrochemical performances of our μ electrodes with the ones already in use for research or clinical studies, already listed in chapter 2 (subchapter 2.3 “Current penetrating clinical and research probes”).

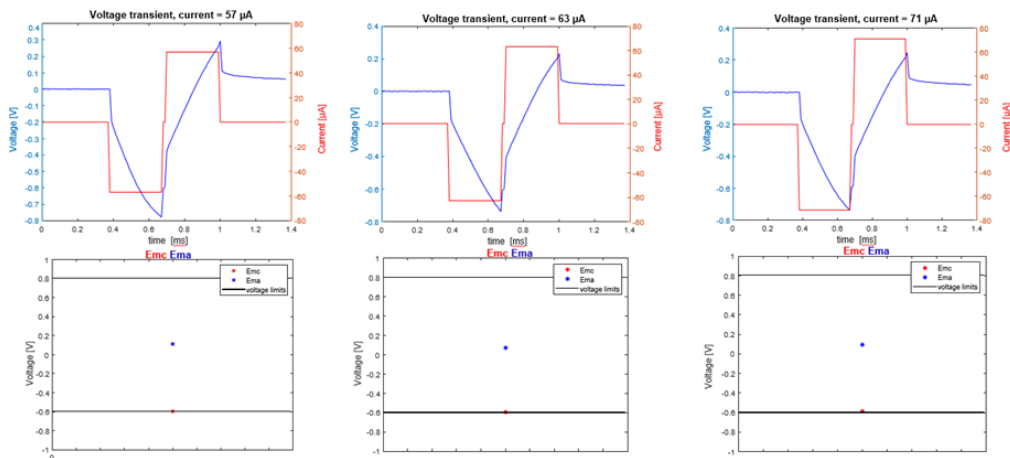


Figure 4.19: Voltage transient measurement with a 0 V bias.

4.4 Comparison with current penetrating stimulating clinical and research probes

Our PtBlack coated μ electrodes with a GSA of about $1800 \mu m^2$ have an impedance of around $12 k\Omega$ at $1 kHz$, and, when they are stimulated by a cathodal first pulse with a pulse width (PW) of $300 \mu s$, they show a CIC of $1.1 mC/cm^2$ at a $0 V$ bias, resulting in a charge per phase of $19.5 nC/ph$. Among the current penetrating clinical and research probes discussed in chapter 2, the ones used for stimulation are the probes used in DBS and the Utah array.

DBS probes are characterized by ring electrodes with an overall GSA ranging from 3 up to $90 mm^2$. The GSA is greatly larger of our μ electrodes GSA, thus only Utah array coated with AIROF or SIROF will be used as a comparison.

Rebecca A Frederick et al. characterized AIROF coated μ electrodes with a GSA of around $2000 \mu m^2$ by their impedance at $1 kHz$ and their CIC [54]. The μ electrodes impedance was in alignment to that of PtBlack. The AIROF coated μ electrodes benefit from a positive bias of $0.6 V$ reaching a CIC value of $2.81 mC/cm^2$, resulting in a charge per phase of around $36 nC/ph$. Another study from Cogan et al. characterized AIROF coated μ electrodes with a GSA of around $1100 \mu m^2$ [55]. The PW in this work was of $400 \mu s$ and the resulting CIC, for a positive bias of $0.5 V$, was $1.8 mC/cm^2$, with a charge per phase of $19 nC/ph$. The impedance magnitude at $1 kHz$ was about $10 k\Omega$.

Two reference studies are reported for SIROF coated μ electrodes with a GSA of $2000 \mu m^2$. The study of Cogan et al. characterized μ electrodes with an impedance magnitude of around $2.6 k\Omega$ and a CIC of around $5 mC/cm^2$ for a PW of $400 \mu s$ and a positive bias of $0.6V$ [**cinquinatacinque**]. A Ghazavi et al. characterized the SIROF coated μ electrodes by their CIC at a bias of $0 V$, resulting in an injectable charge of about $1.5 mC/cm^2$ for a PW of $200 \mu s$ [56].

Felix Deku et al characterized a EIROF (electrodeposited iridium oxide) coated carbon fiber with a GSA of $1500 \mu m^2$ which showed an impedance magnitude of around $50 k\Omega$ and, for a PW of $300 \mu s$, a CIC of about $5 mC/cm^2$ with a $0.6 V$ positive bias going down to $1 mC/cm^2$ with a $0 V$ bias [57].

This thesis PtBlack coated μ electrodes show electrochemical performances comparable to that of the other discussed μ electrodes. When the bias is $0 V$, as it will be in the in vivo application, the CIC is significantly lower than that of AIROF and SIROF with a positive bias of $0.6 V$, but comparable with that of SIROF with a $0 V$ bias. The injectable current is enough for the cortex stimulation [22]. Douglas et al. estimated that the threshold to exceed to effectively stimulate the cortex is $1-3 nC/ph$ [58], while Kane et al. estimated the safety threshold to be of $8 nC/ph$ [59]. The PtBlack coated μ electrodes can inject a charge density of around $20 nC/ph$, which greatly exceed the minimum value needed for the stimulation. The stimulation pulse for this electrode has a PW of $300 \mu s$ and a desired current of $\pm 50 \mu A$ resulting

in a charge density of 15 nC/ph, exceeding the safety limit. In vivo studies must be performed to investigate this aspect. The results are summed up in Table 4.1.

Material	Area [μm^2]	Bias [V]	PW [μs]	CIC [mC/cm^2]	I_{inj} [μA]	Charge density [nC/ph]	Z [$\text{k}\Omega$]	REF.
PtBlack	1800	0	300	1.1	~65	~19.5	~10	
	1600	0.5		2.1	~120	~36.04	~12	
AIROF	2000	0.6	200	2.81	187	~56.2	~10	[54]
	1100	0.5	400	1.8	49.5	~20	~10	[55]
SIROF	2000	0.6	400	~5	250	~100	~3	[60]
	2000	0	200	~1.5	140	~30		[59]
EIROF	1500	0	300	~1	50	~15	~50	[56]
		0.6		~5	250	~75		

Table 4.1: Comparison of penetrating stimulating pelectrodes.

4.5 Bipolar microelectrodes

Before proceeding with the long-term stimulation, to mimic the in vivo situation, two pelectrodes are attached together as described in chapter 3 “Materials and methods” (subchapter 3.4 “Bipolar microelectrodes”). This chapter will firstly discuss about the efficiency of the linking process and then it will provide some images of the pairs acquired with both the optical microscope and the SEM.

4.5.1 Electrochemical characterization

The pelectrodes have been electrochemically characterized before and after having been linked together by means of CV, EIS, and voltage transient.

Figure 4.20 shows the results obtained in CV and EIS measurements, together with the values of CSC_c and of impedance magnitude at the three frequencies of 10, 100, and 1000 Hz. All the parameters are calculated over a sample of 5 pairs of pelectrodes and the results are given computed as average value \pm SEM, for CV curves and CSC_c values, and average value \pm SDM, for EIS curves and impedance magnitude values. The linking process damages the pelectrodes worsening their electrochemical performances affecting both their CSC_c and impedance magnitude. The CSC_c was around 18 mC/cm^2 and went down to about 11 mC/cm^2 and the impedance magnitude at 1 kHz doubled, going up to $18 \text{ k}\Omega$.

Figure 4.21 shows the voltage transient measurements and the E_{mc} and E_{ma} values. Despite showing a slight change in voltage transient shape, E_{mc} and E_{ma} values remain stable and inside the limits. Thus, the bipolar pelectrodes can be used in long-term stimulation experiments. Nevertheless, some pairs were further ruined due to the handling of the pelectrodes, which would eliminate some of the coating from the tips.

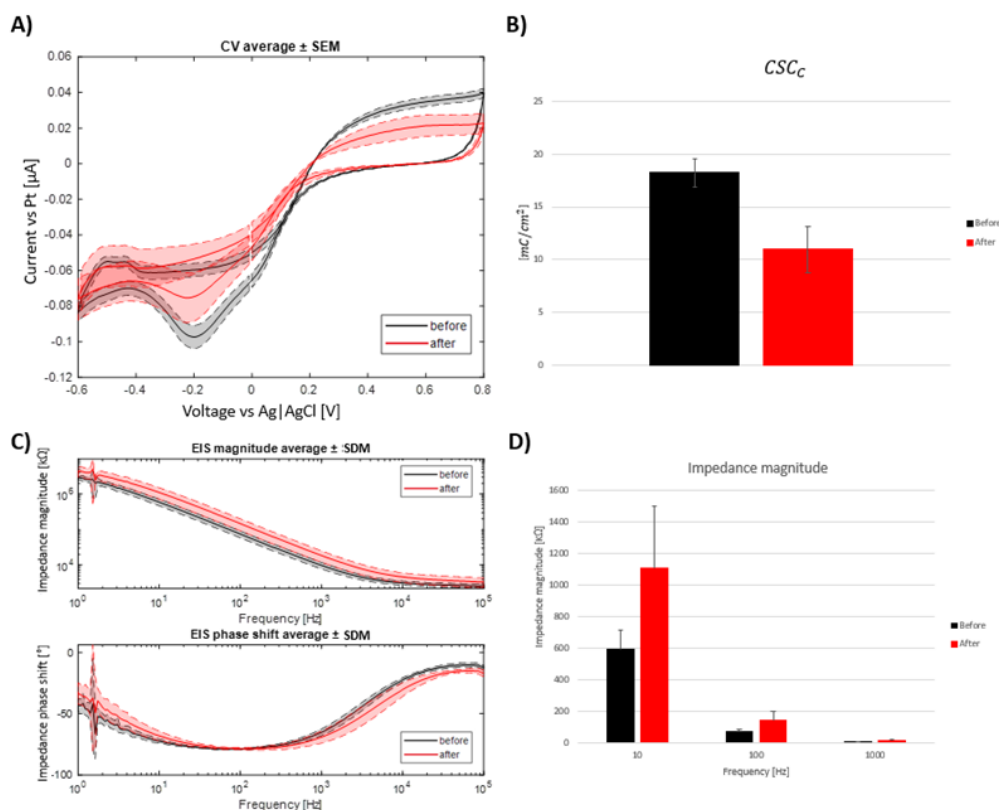


Figure 4.20: Electrochemical measurements before and after linking two μ electrodes together calculated over 10 μ electrodes. A) CV, B) CSC_c , C) EIS, and D) impedance magnitude.

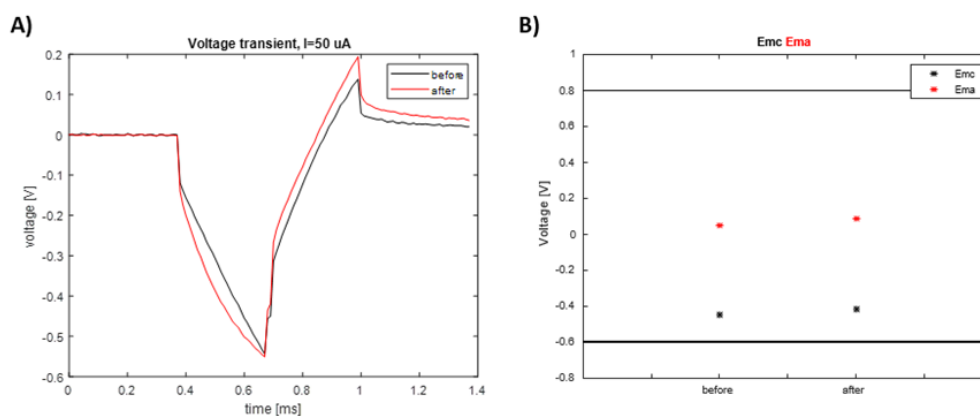


Figure 4.21: A) Voltage transient, and B) E_{mc} and E_{ma} .

4.6 Visual inspection

Figure 4.22 shows images taken with both the optical microscope and the SEM. With the process made by hand several issues have been encountered. Firstly, despite the process being carried out under the optical microscope, it's hard to control the distance between the tips. Moreover, as shown in one of the images in Figure 4.22 A, the μ electrodes are relatively flexible, and they can be bend during the process.

Finally, as mentioned above, manually handling the μ electrodes can ruin the coating worsening the electrochemical performances.

In this study, for further experiments, the bipolar μ electrodes obtained with this process are sufficient. Nevertheless, the process should be improved. A possible solution is to create a structure which would help to place the electrode at the desired distance and to give support limiting the handling and thus the damage. Manually creating the bipolar μ electrodes will not be needed in the final application in which only the top 1.5 mm of the μ electrodes will be placed in the chip.

The obtain pairs of bipolar μ electrodes will be used in this study to perform

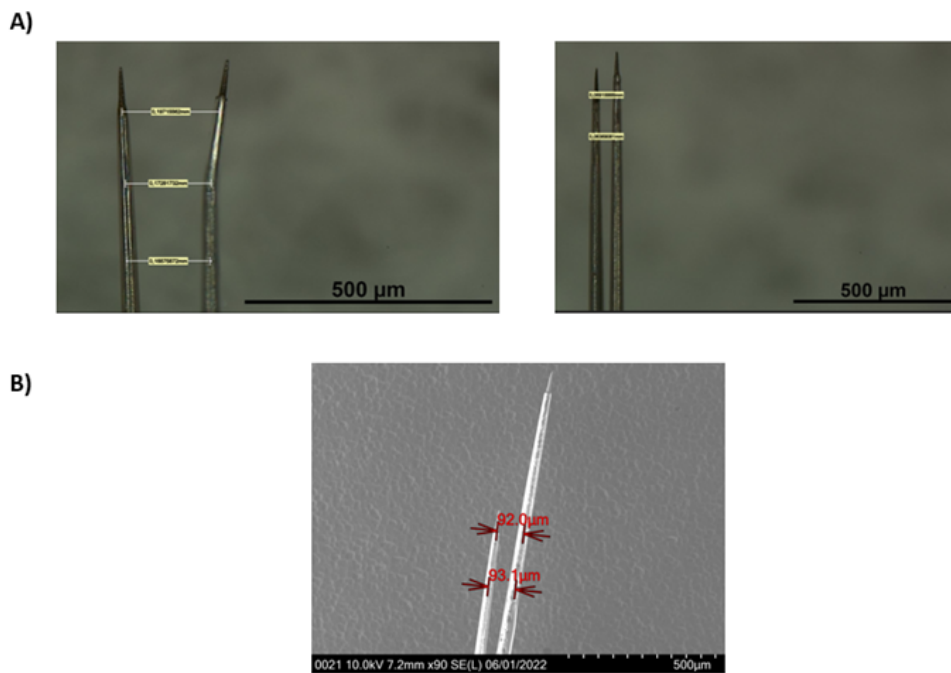


Figure 4.22: Visual inspection of the bipolar μ electrodes. A) Images taken with optical microscope, and B) SEM images.

long-term stimulation experiments, which will be discussed in the next subchapter.

4.7 Long-term stimulation

Four long-term stimulation experiments, differing for number of pulses, have been performed on a total of 5 pairs of μ electrodes and one single μ electrode. Each experiment will be discussed in detail, providing the complete electrochemical characterization (CV, EIS, and voltage transient) for both the stimulating and counter μ electrodes at each step of the stimulation. Finally, a morphological characterization will be provided through SEM images acquired after the experiments.

Positive and negative peaks appear on the CV curves of the stimulating μ electrode after the first round of stimulation as well as a step in the EIS measurements corresponding to 200 Hz. This could be an error owe to the measuring device and it can

be resolved by repeating the measurements as many times as needed. Figure 4.23 shows how the peaks, and the steps in the CV and EIS curves are attenuated till their disappearance. In some cases, a high number of repetitions would be needed to eliminate the error, thus this was not done for each μ electrode. Instead, the CSC_c was calculated on the original curves obtained just by cutting out the peaks, while no adjustment was necessary for the EIS measurements since the error occurred after the device measured the impedance at 1 kHz.

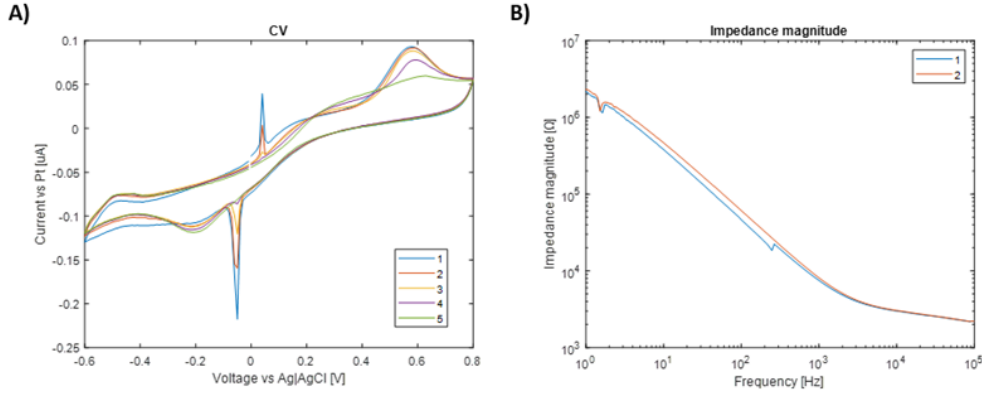


Figure 4.23: Adjusting CV and EIS curves by eliminating the peaks. A) CV, and B) impedance magnitude.

4.7.1 Experiment 1

One single μ electrode has been subjected to this protocol: it has been stimulated by the repetition of the basic stimulation protocol, described in Chapter 3 “Materials and methods” (subchapter 3.3.4 “Long-term stimulation”), for 150 k times for 4 steps, for a total of 600 k train of pulses and 4.2 M single pulses. A platinum wire has been used as a counter electrode. Figure 4.24 shows the CV curves for the stimulating μ electrode and the CSC_c values over the whole stimulation. After the first round of stimulation the CV curve enlarges with a consequential increase in the CSC_c which goes from 10 mC/cm^2 up to around 100 mC/cm^2 , remaining relatively stable over the following rounds of stimulation but with the highest value of 124 mC/cm^2 .

Figure 4.25 displays the EIS curves and the respective impedance magnitude calculated at 1 kHz over the whole stimulation. While the CSC_c increases, the impedance magnitude decreases reaching 6-7 k Ω . This value does not swing significantly over the following stimulation steps.

Voltage transient curves are shown in Figure 4.26 together with the corresponding E_{mc} and E_{ma} values. Overall, both positive and negative maximum polarization values do not exceed the limits of the water window, except for the E_{mc} value measures after 300 k train of pulses (-0.65 V).

The results show that the μ electrode survived the first experiment.

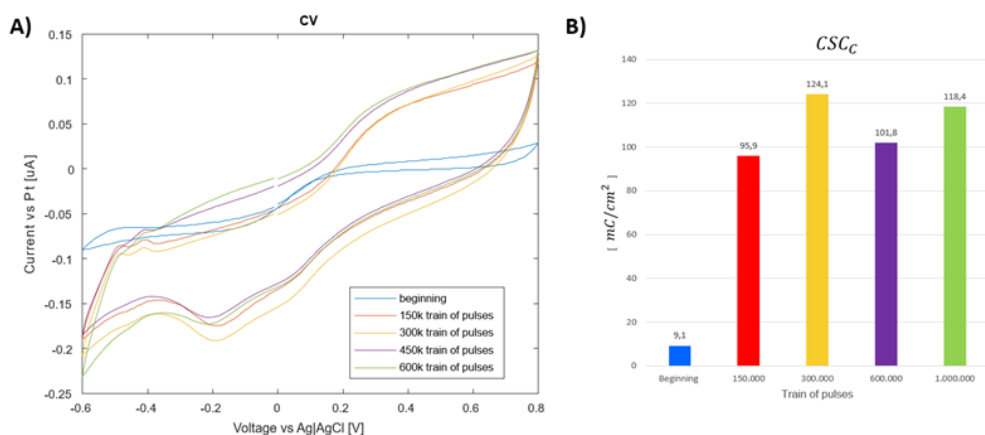


Figure 4.24: CV measurement for the first long-term stimulation experiments. A) CV curves, and B) CSC_c values.

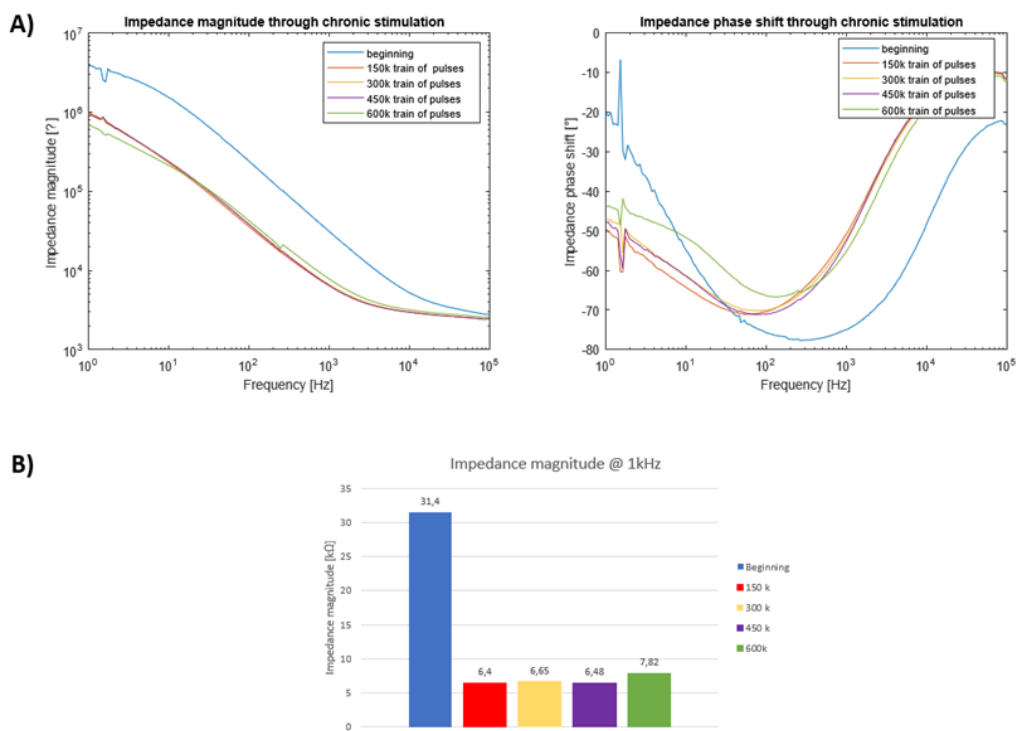


Figure 4.25: EIS measurements for the first long-term stimulation experiment. A) EIS magnitude and phase shift curves, and B) impedance magnitude values at 1 kHz.

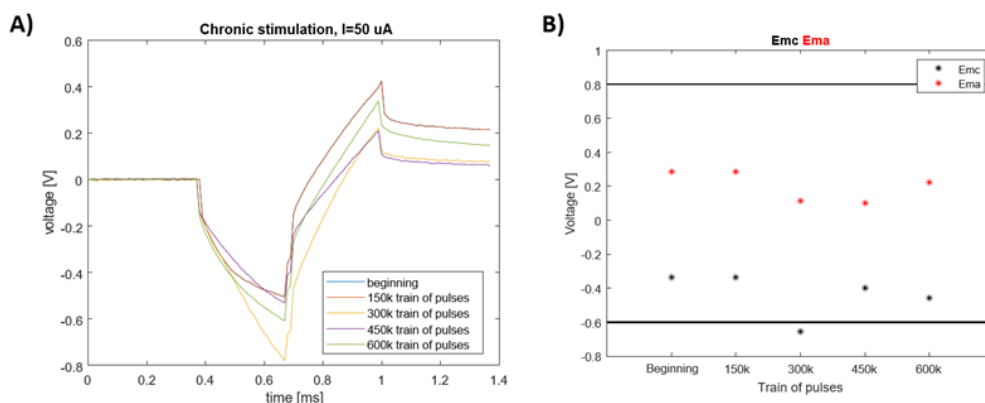


Figure 4.26: Voltage transient measurement for the first long-term stimulation experiments. A) Voltage transient curves, and B) E_{mc} and E_{ma} values.

4.7.2 Experiment 2 - Experiment 3

Two pairs of bipolar μ electrodes were used for the second experiment, for which they were stimulated in four steps each with the maximum number of train of pulses the stimulator can provide continuously, i.e., 162 k, for a total of 648 k train of pulses and 4.5 M single pulses. In experiment 3, one pair of bipolar μ electrodes has been stimulated with 1.296 M train of pulses, for a total of 9 M single pulses. Stimulating and counter μ electrodes have the same GSA and are made of the same material.

Regarding the second experiment, for the first pair the electrochemical measurements have been performed only on the stimulating μ electrode, while results for both stimulating and counter μ electrodes are provided for the second pair. Figure 4.27 shows the CV curves together with the CSC_c values for both pairs.

Concerning the CSC_c , all the three μ electrodes show the same trend of the first experiment, but for the stimulating μ electrode of the second pair the increase in CSC_c is less marked with the value increasing only of the 25% of the initial value. The EIS curves and the corresponding impedance magnitude values calculated at 1 kHz are displayed in Figure 4.28. The results obtained from the first experiment are confirmed, with the impedance magnitude decreasing in all three μ electrodes, going down to 5-9 k Ω .

Figure 4.29 shows the voltage transient curve and the oscillation of the E_{mc} and E_{ma} values. Both the most positive and the most negative maximum polarization remain within the limits of the water window during the whole long-term stimulation protocol.

The electrochemical measurements for the third experiment have been acquired only for 2 sets points, the first after 486k train of pulses and the second after 1.293M train of pulses. The trends in CSC_c , impedance magnitude and E_{mc} and E_{ma} values are confirmed.

Figure 4.30 shows the three final graphs collecting the results from all the three experiments for the parameters of main interest: CSC_c , impedance magnitude and E_{mc} and E_{ma} values.

The electrochemical performances of all three pairs of bipolar μ electrodes are still satisfying after the long-term stimulation.

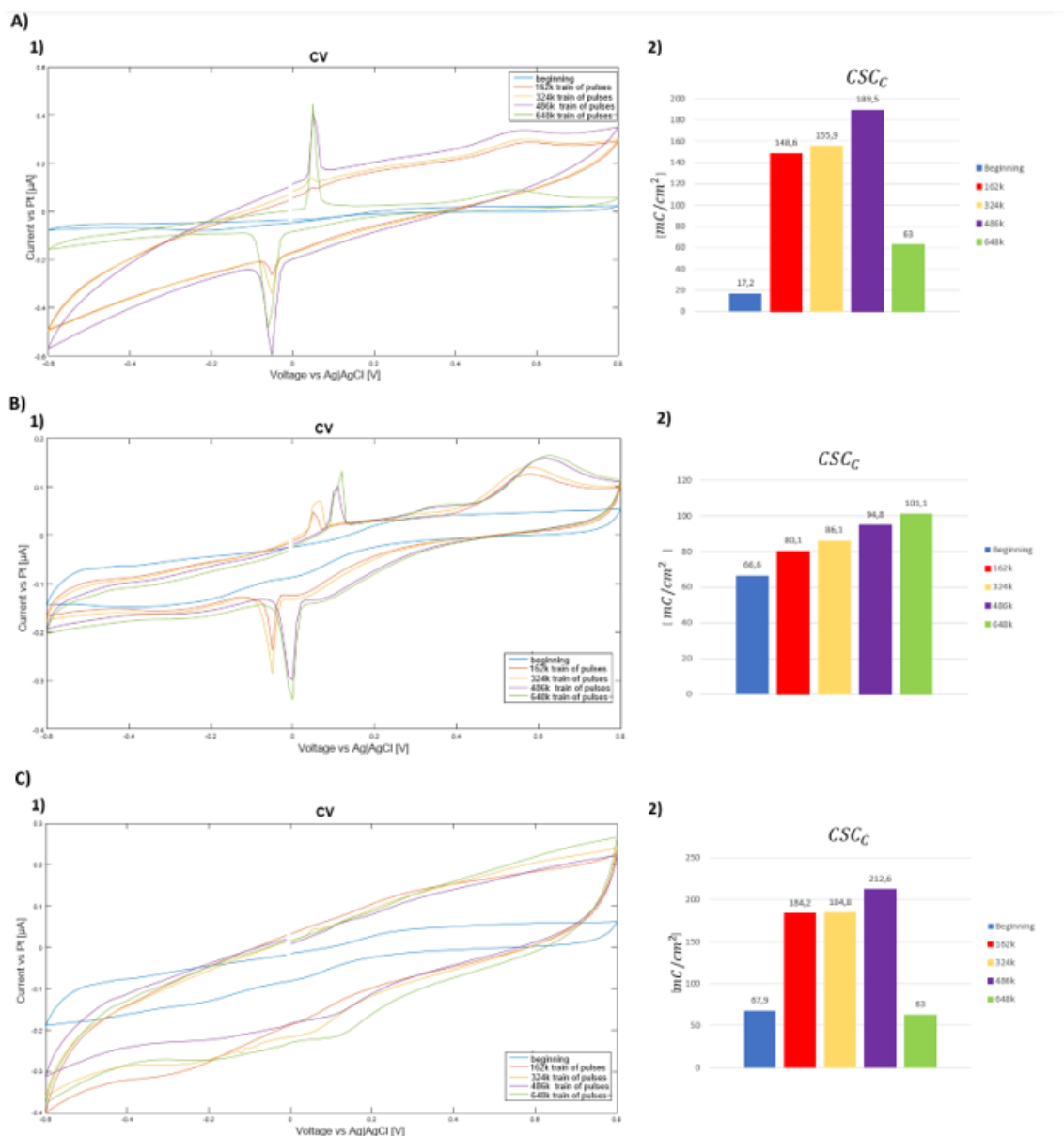


Figure 4.27: CV curves and CSC_c for the second long-term stimulation experiment. A) Stimulation μ electrode of the first pair, B) stimulating μ electrode of the second pair, and C) reference μ electrode of the second pair.

4.7.3 Experiment 4

As for the final long term stimulation protocol, the in vivo situation was simulated, stimulating two pairs of μ electrodes for 5 days for 8 hours per day continuously. One of the pair was stimulated with 25 μ A; a lower current was necessary because

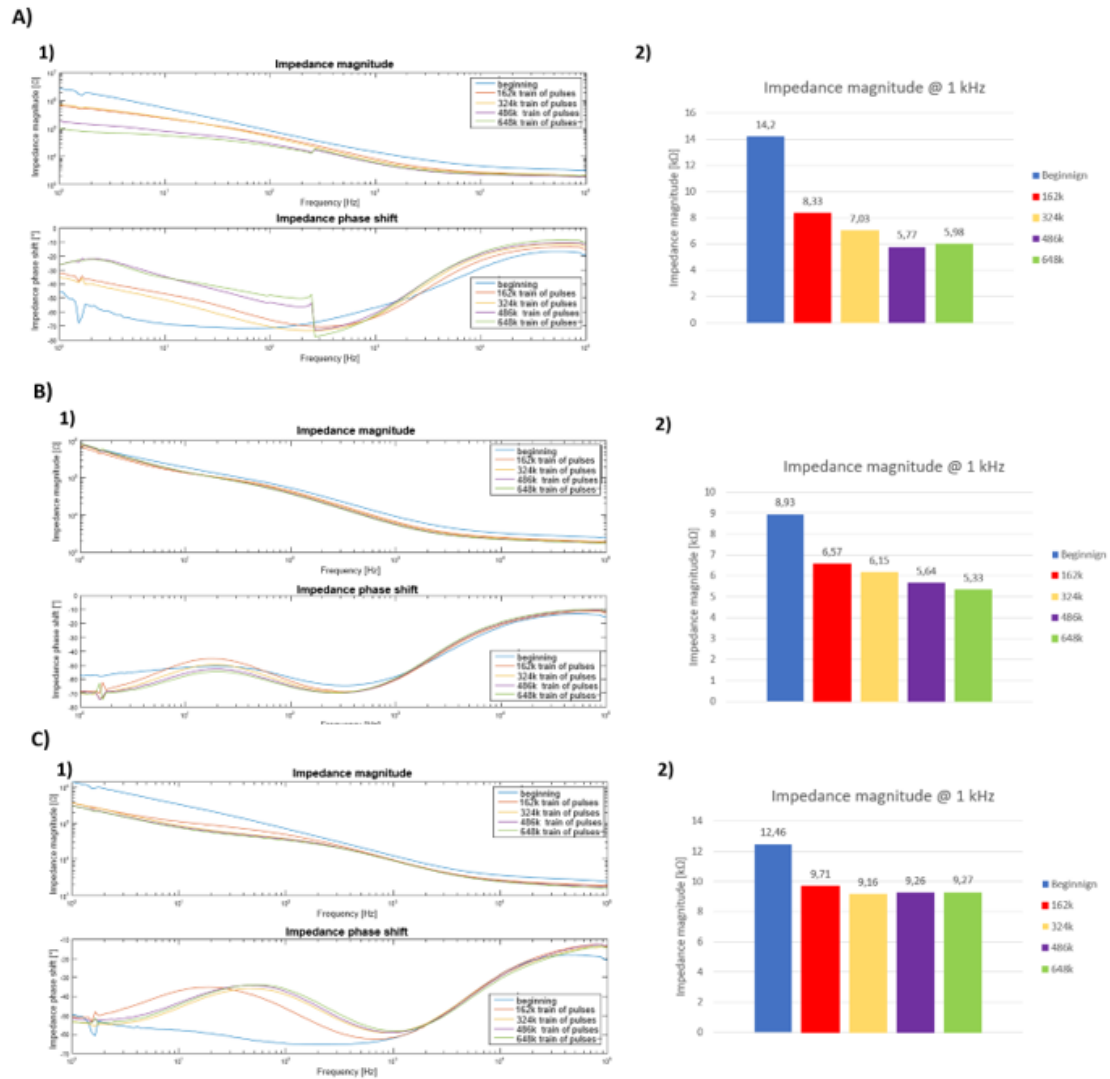


Figure 4.28: EIS curves and impedance magnitude values for the second long-term stimulation experiment. A) Stimulation pelectrode of the first pair, B) stimulating pelectrode of the second pair, and C) reference pelectrode of the second pair.

this pair of pelectrodes was ruined while they were being linked, decreasing their CIC.

CV, EIS and voltage transient curves are shown only for the stimulating pelectrodes of both pairs, while the final graphs assembling the results of the three parameters of interested CSC_c , impedance magnitude and E_{mc} and E_{ma} are provided for both stimulating and counter pelectrodes.

CV curves and CSC_c values are shown in Figure 4.31. For both pairs of pelectrodes, there is an increase in CSC_c , but it is sharper for the pelectrode stimulated by $50 \mu\text{A}$. In this case, there is no visible decrease in the impedance magnitude, as shown in Figure 4.32. Figure 4.33 displays the voltage transient curves and the E_{mc} and E_{ma} values. For the stimulating pelectrodes the E_{mc} and E_{ma} values are stable during the whole stimulation.

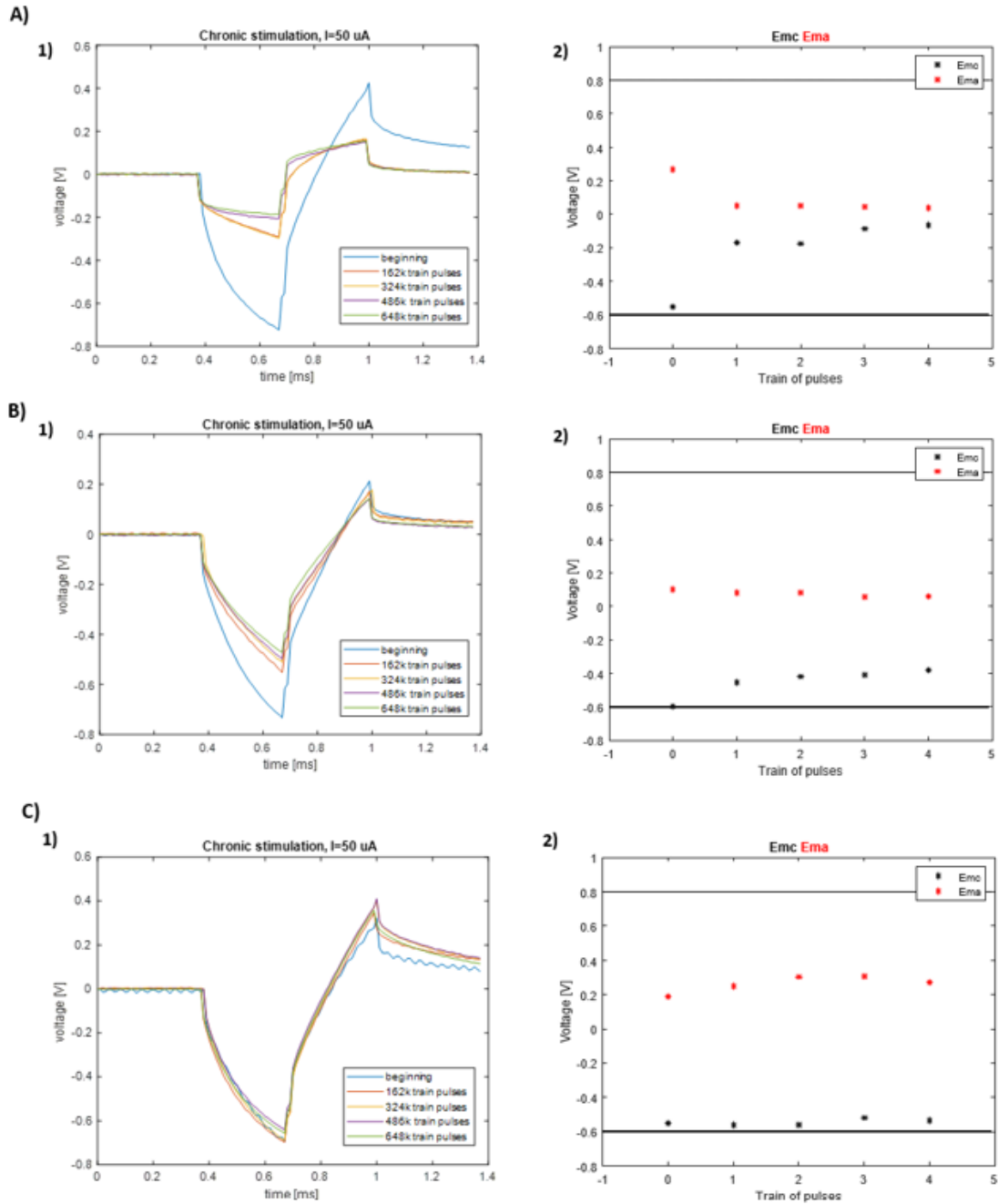


Figure 4.29: Voltage transient curves and E_{mc} and E_{ma} values for the second long-term stimulation experiment. A) Stimulation pelectrode of the first pair, B) stimulating pelectrode of the second pair, and C) reference pelectrode of the second pair.

After the 5 days of stimulation the CIC of the four pelectrodes has been computed again. There is an increased in the current injectable with the stimulating pelectrode with respect to the counter; after the experiment, the stimulating pelectrode stimulated with $25 \mu\text{A}$ can inject a maximum current of $43 \mu\text{A}$, while the pelectrode stimulated with $50 \mu\text{A}$ can inject a maximum current of $77 \mu\text{A}$. The bar plot reporting the maximum injectable current for the stimulating and current pelectrodes for

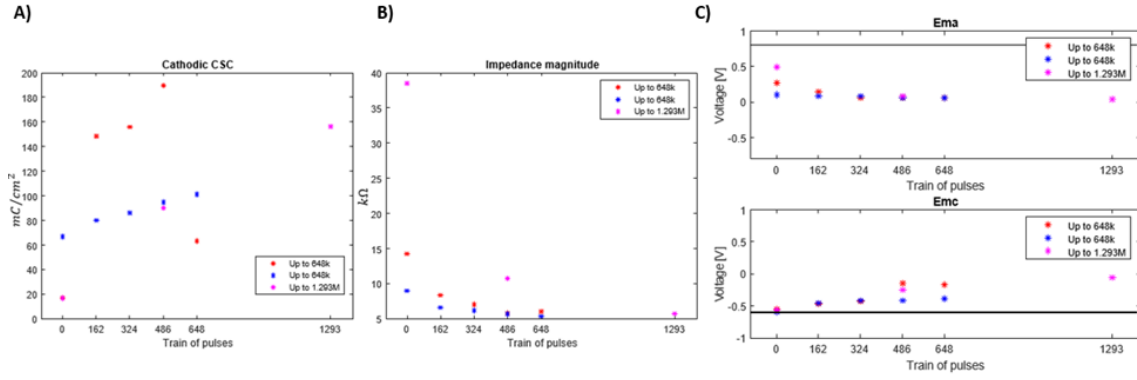


Figure 4.30: Final graphs for the second and third long-term stimulation experiments. A) CSC_c , B) impedance magnitude at 1 kHz, and C) E_{mc} and E_{ma} values.

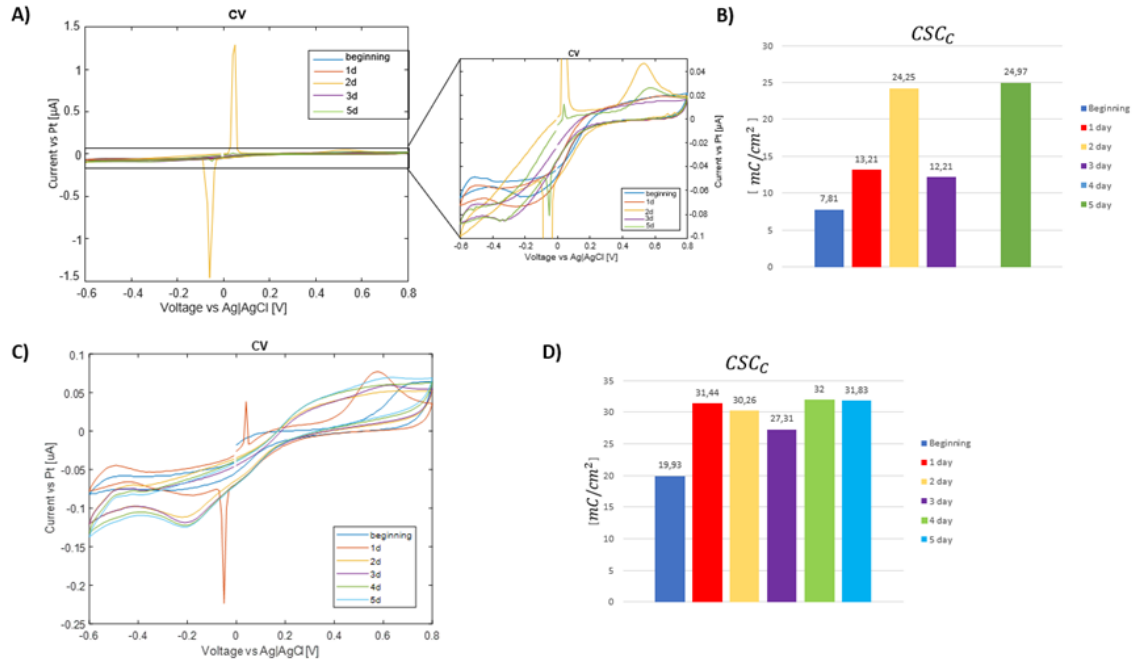


Figure 4.31: CV measurements for the stimulating μ electrodes of the two pairs of the fourth experiment. A) CV curves for the first pair, B) CSC_c for the first pair, C) CV curves for the second pair, and D) CSC_c for the second pair.

both pair is shown in Figure 4.34. This suggests that PtBlack could be activated during the stimulation, in higher measure for the stimulating μ electrode. The graphs that assemble the results of interest (CSC_c , the impedance magnitude and the E_{mc} and E_{ma} values) are displayed in Figure 4.35. The counter μ electrode of the pair stimulated by 25 μA was further damaged during the linking process, resulting in the E_{mc} exceeding the water oxidation potential before starting the long-term stimulation experiment. However, the E_{mc} goes back into the limits as the stimulation goes on. Both pairs of μ electrodes are still functional after this experiment, demonstrating that the PtBlack coating is suitable for a long-term stimulation up to 1.4 M of train of pulses with a current of 50 μA .

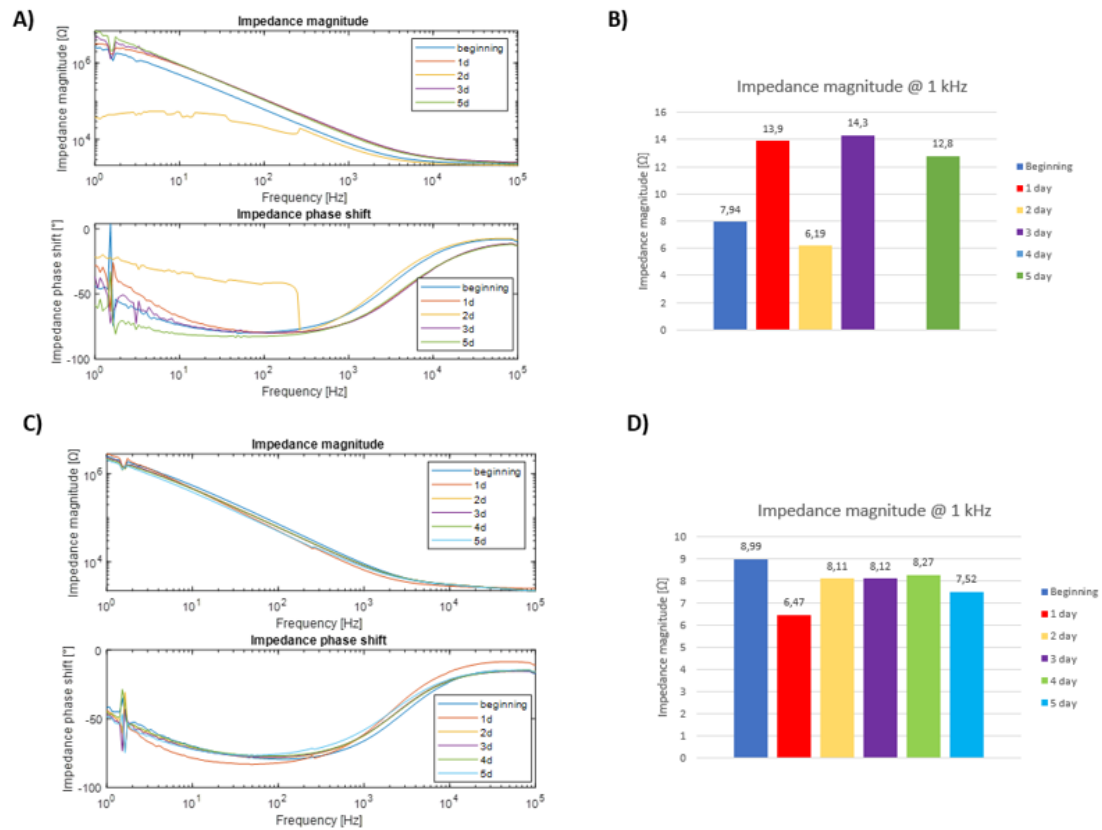


Figure 4.32: EIS measurements for the stimulating μ electrodes of the two pairs of the fourth experiment. A) EIS curves for the first pair, B) impedance magnitude values for the first pair, C) EIS curves for the second pair, and D) impedance magnitude values for the second pair.

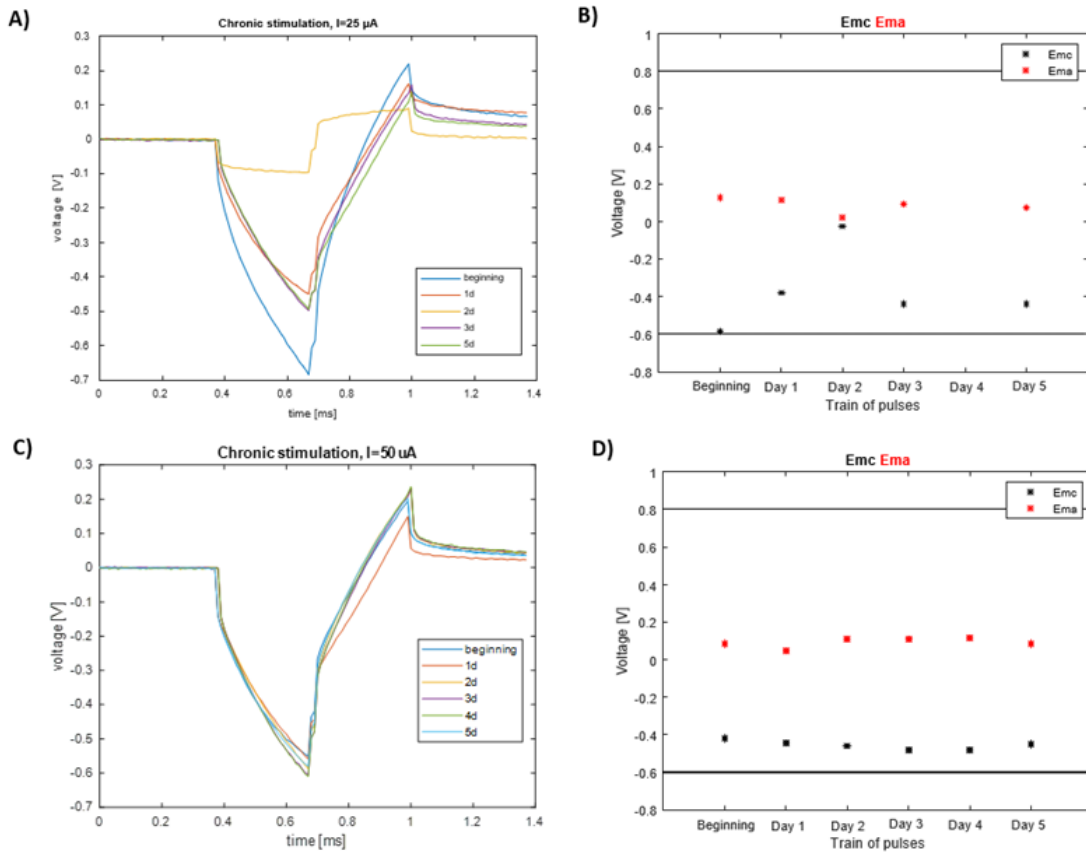


Figure 4.33: Voltage transient measurements for the stimulating pelectrodes of the two pairs of the fourth experiment. A) Voltage transient curves for the first pair, B) E_{mc} and E_{ma} values for the first pair, C) voltage transient curves for the second pair, and D) E_{mc} and E_{ma} values for the second

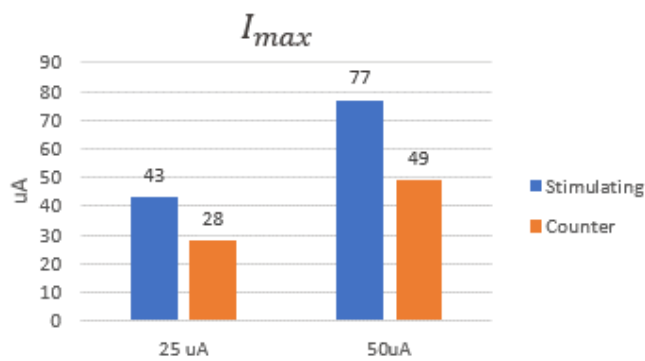


Figure 4.34: Bar plot for the maximum injectable currents for stimulating and counter pelectrode for both the pairs of the fourth long-term stimulation experiment.

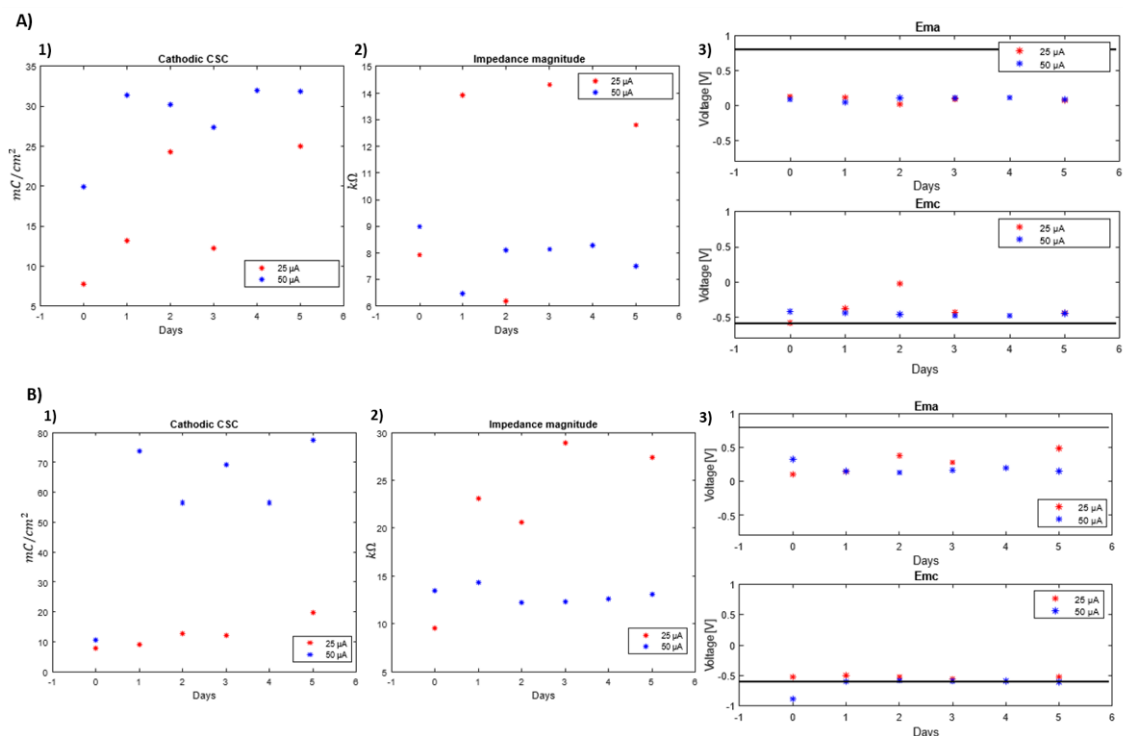


Figure 4.35: Final graphs for the fourth long-term stimulation experiments. A) Stimulating μ electrodes (1) CSC_c , 2) impedance magnitude at 1 kHz, and 3) E_{mc} and E_{ma} values), and B) counter μ electrodes (1) CSC_c , 2) impedance magnitude at 1 kHz, and 3) E_{mc} and E_{ma} values).

4.8 Visual inspection

Figure 4.36 shows the SEM images of the PtBlack coating before and after the stimulation for both the stimulating and the counter μ electrode. The coating is still clearly visible on the μ electrodes, confirming that they outlived the long-term stimulation test. The coating for the stimulating μ electrode is more hydrated with respect to the counter; this confirms the results obtained from the electrochemical measurements performed.

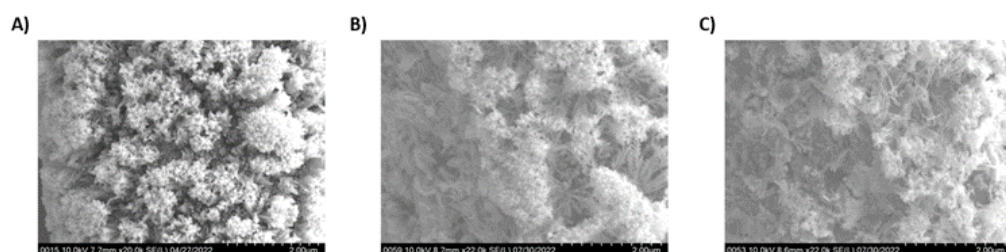


Figure 4.36: SEM images. A) Before the long-term stimulation, B) stimulating μ electrode after the long-term stimulation, and C) counter μ electrode after the long-term stimulation.

4.9 Insertion in the brain-like agarose gel

One μ electrode has been inserted in a brain-like agarose gel to check if the insertion would make the coating detach from the μ electrode. Figure 4.37 shows the μ electrode inserted in the brain-like agarose gel.

The μ electrode was electrochemically characterized before and after the insertion by means of CV and EIS measurements, presented in Figure 4.38, and finally SEM images, shown in Figure 4.39, were acquired after the insertion to see if residues of the agarose gel stucked to the μ electrode.

The electrochemical performances did not significantly change, there was a slight increase in impedance magnitude at 1 kHz from 9 k Ω up to 11 k Ω and a minor increase of the CSC_c , which went from 20.4 mC/cm^2 up to 21.5 mC/cm^2 .

From the SEM image, the coating appears intact, but on the side of the μ electrode there is residues of the agarose gel. It is not clear if the gel stucked to the μ electrode during the insertion or the extraction of the μ electrode. To analyze the electrochemical performances of the μ electrodes once they are inserted into the brain, an ex vivo experiment with an extracted pig brain can be performed.

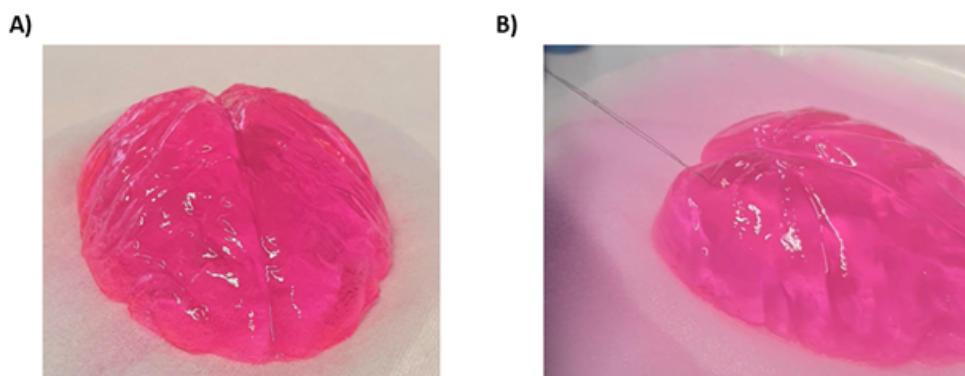


Figure 4.37: A) Brain-like agarose gel, and B) μ electrode insertion.

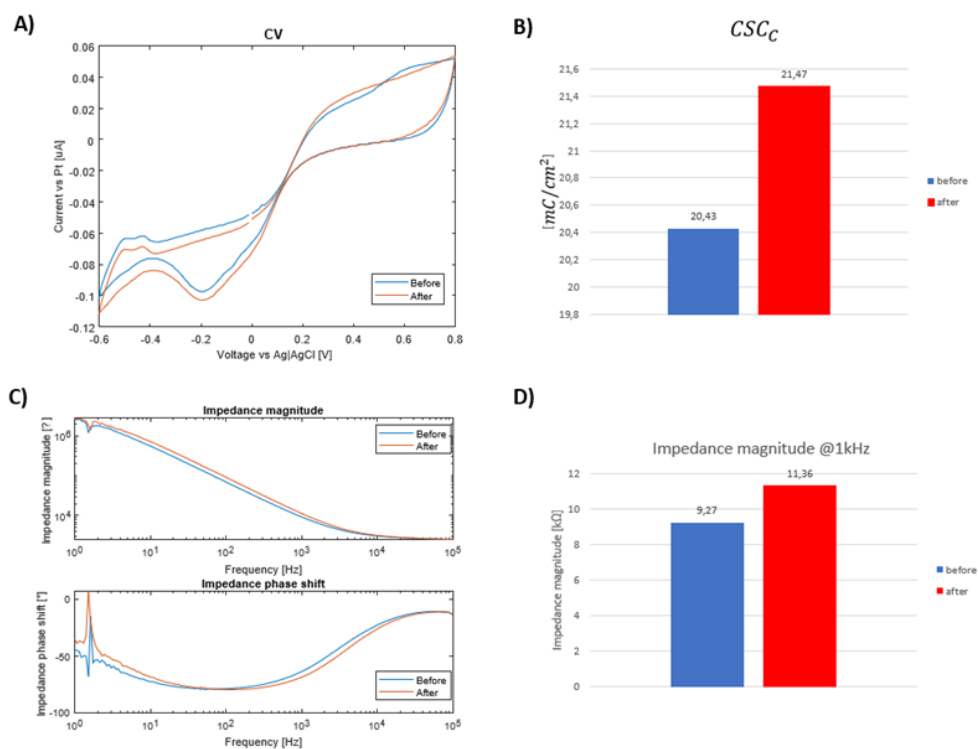


Figure 4.38: Electrochemical measurements performed before and after the insertion in the brain-like agarose gel. A) CV curves, B) CSC_c values, C) EIS curves, and D) impedance magnitude values.

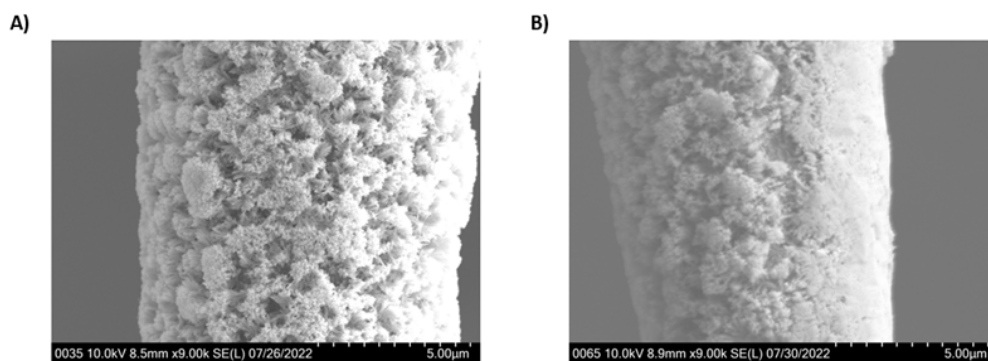


Figure 4.39: SEM images. A) Before the insertion in the brain-like agarose gel, and B) after the insertion in the brain-like agarose gel.

Chapter 5

Conclusions and prospects

Blindness is a disease affecting 43.3 million people worldwide which has a severe personal and economic impact. Visual prostheses are an innovative and effective solution to vision impairment that exploit neuromodulation to create an artificial sense of vision by stimulating the neurons of the visual pathway at some point beyond the lesion site. Among the other visual prostheses, cortical prostheses arouse particular interest. The cortical approach offers both several advantages and disadvantages. Stimulating directly on the cortex allows to treat most causes of blindness and the large area of the cortex could permit to place many electrodes and to have a lower stimulation threshold. However, the presence of wires limits the number of electrodes and thus the spatial resolution of the stimulation and, furthermore, the surgery is very invasive. The project “Smart neural dust to revert blindness” aims to develop a freestanding array of thousands of individually addressable CMOS- μ electrodes to wirelessly stimulate the visual cortex.

This Master Thesis developed and characterized a coating material for the commercial penetrating PtIr μ electrodes used in the smart neural dust system, with the ultimate goal of injecting a current of $\pm 50 \mu\text{A}$. The μ electrodes play a crucial role in a BMI, since they act as an interface between the neural tissue and all the electronics behind. When selecting a material for a neural interface, several aspects need to be addressed; firstly, the mechanical mismatch between the tissue and the electrodes can cause the death of a larger number of neurons; then electrochemical performances need to be optimized in order to increase the CIC of the μ electrodes and to decrease their impedance magnitude; finally, the long-term reliability of the interface needs to be assessed.

IrOx, PEDOT:PSS, and PtBlack have been compared by means of CV, EIS, and voltage transient measurements as well as morphological characterization.

The characterization of IrOx coated μ electrodes was not possible since the sputtering of IrOx encountered technical problems.

PEDOT:PSS is a soft material, reducing the mechanical mismatch with the tissue, with excellent electrochemical properties. The PEDOT:PSS coated μ electrodes showed a major improvement in both impedance magnitude, reaching the value of 2 k Ω , and in CSC_c , with an order of magnitude of 10 thousand of mC/cm^2 . However, the electropolymerization of PEDOT:PSS is hard to control and not repeatable.

PtBlack, being a metal, is stiffer than the brain and provoke a higher mechanical mismatch; but, on the other hand, its electrodeposition is a reliable and repeatable process, and its electrochemical performances are satisfactory. PtBlack was deposited on five μ electrodes with different GSA ($334 \mu m^2$, $850 \mu m^2$, $1600 \mu m^2$, $1800 \mu m^2$, and $7550 \mu m^2$). The μ electrodes with a GSA of 1800 and $7550 \mu m^2$ satisfy the main requirement, being able to inject more than $\pm 50 \mu A$, but the exposed conductive tip of the former with a $75 \mu m$ length has a more appropriate size for a more spatial selective stimulation of the layer 4c of the visual cortex. In detail, the so obtained μ electrodes have a CIC of $1.1 mC/cm^2$ and a maximum I_{inj} of around $70 \mu A$.

The monopolar μ electrodes have been linked in pairs to obtain a bipolar μ electrode. The manual linking process is very delicate and it slightly ruined the μ electrodes, worsening their electrochemical performances.

Four long-term stimulation experiments have been performed on the PtBlack coated μ electrodes and the electrochemical measurements have been performed after the stimulation protocols to evaluate if they have been destructive for the μ electrodes. The most significant parameters (CSC_c , impedance magnitude, and E_{mc}) and E_{ma} values) have been computed as well as the SEM images for a morphological evaluation. Both the stimulating and the counter μ electrodes maintain good electrochemical performances after being stimulated with 4 million of single pulses.

The master thesis has reached the main goal: the electrodeposition of the Pt-Black is easy and repeatable, the impedance magnitude value is low, the injectable current is sufficient for efficiently stimulate the visual cortex, and the μ electrodes are reliable over a long-term period.

However, several issues need to be resolved. Increasing the area up to $2200 \mu m^2$ (obtainable with a conductive tip length of about $90 \mu m$) would still provide a stimulation with a high spatial selectivity while ensuring a safety margin, providing a maximum injectable current of $90 \mu A$. Another aspect to improve is the linking process. Using a μ structure would help to link the two monopolar μ electrodes at a fixed distance and with a minor probability of ruining them by taking away the coating. The mechanical mismatch cannot be improved unless using a softer coating material. Going in that direction, PEDOT:PSS coating process could be tune and optimized taking into account the particular shape of the μ electrodes which currently makes the coating uneven.

Appendix A

Matlab Codes

A.1 Charge Storage Capacity

```
1 function [csc, csc_cathodic, csc_anodic, csc_tot, expected_max_curr,
2 cv_mean]=calcolo_csc_nolimit(cv)
3 volt=(cv(:,1));
4 [row, columns]=size(cv);
5 a=1;
6 %
7 %parameters for electrode area , in cm
8 %500 kohm 1
9 %h=24*10^-4;
10 %r1=(7.07/2)*10^-4;
11 %r2=(2.49/2)*10^-4;
12 % % %
13 % % 100 kohm 2
14 % h=34.1*10^-4;
15 % r1=(12.3/2)*10^-4;
16 % r2=(2.99/2)*10^-4;
17 %
18 % %50 kohm
19 % h=75*10^-4;
20 % r1=(12.2/2)*10^-4;
21 % r2=(3.61/2)*10^-4;
22 %
23 % %10 kohm
24 % h=179.4*10^-4;
25 % r1=(18.06/2)*10^-4;
26 % r2=(8.42/2)*10^-4;
27 ap= sqrt((h^2)+((r1-r2)^2));
28 A1=pi*ap*(r1+r2);
29 A2=(4*pi*r2^2)/2;
30 A=A1+A2;
31 for i=2:5:columns
32     b=i+4;
33
34     cv_mean=cv(:,2);
```

```

35 % you need the *10-3 (10-6 in nA) if you have uA; 0.05 is the scan
    rate in V/s; A in cm2 and final result in mC/cm2
36 csc(a,1)=(((abs(trapz(volt,cv_mean(:,a))))*(10-3))/0.05)/A;
37
38 cathodic_index=find(cv_mean(:,a)<=0);
39 csc_cathodic(a,1)=(((abs(trapz(volt(cathodic_index),cv_mean(
    cathodic_index,a))))*(10-3))/0.05)/A;
40
41 anodic_index=find(cv_mean(:,a)>0);
42 csc_anodic(a,1)=(((abs(trapz(volt(anodic_index),cv_mean(
    anodic_index,a))))*(10-3))/0.05)/A;
43
44 csc_tot(a,1)=csc_anodic(a,1)+csc_cathodic(a,1);
45 a=a+1;
46 end
47 end

```

A.2 Charge Injection Capacity

```

1 clear all
2 close all
3 clc
4
5 %takes the Ivium data, and computes Emc and Ema
6 %goes in the folder to select the wanted ivium data and return to
    current
7 %folder
8 currdir= cd
9 % specify the folder you want to take the excel's files from
10 cd C:\Users\danie\Desktop\Tesi\CIC\
11 [file , path] = uigetfile('*.xlsx');
12 currentfile=[path, file];
13 data=xlsread(currentfile);
14 cd(currdir)
15
16 %the first coloumn is the time in ms , the
17 %second coloumn is the voltage (in V)
18 %the time needs to start from 0 ms, so you subtract the first time
    value from
19 %the entire frequency vector
20 time= data(:,1);
21 time = time-time(1);
22 %calculate Emc and Ema from the curve without bias ( translate the
    curve to
23 %0)
24 voltage = data(:,2)-data(1,2);
25 %definition of the pulse characteristics (in ms)
26 pw= 0.3; %pulse width
27 inter_phase =0.02;
28 inter_pulse = 0.38;
29 ratio=1;
30 n_pulses = 1;

```

```
31 % Emc is computed at 0.01 ms after the end of the cathodic pulse and  
    Ema is  
32 % computed at 0.01 ms after the end of the anodic pulse  
33 fixed_increment_Emc = inter_pulse + pw + 0.01;  
34 frequency_multiplier = inter_pulse + pw + inter_phase + pw/ratio; %  
    length of a stimulus in time;  
35 fixed_increment_Ema = inter_pulse + pw + inter_phase+pw/ratio+0.01;  
36  
37 for i=1:n_pulses;  
38  
39     idx_cathodic(i)=find(abs(time-(fixed_increment_Emc+  
    frequency_multiplier*(i-1)))<0.001);  
40     Ecm(i)=voltage(idx_cathodic(i));  
41  
42     idx_anodic(i)=find(abs(time-(fixed_increment_Ema+  
    frequency_multiplier*(i-1)))<0.001);  
43     Eam(i)=voltage(idx_anodic(i));  
44  
45 end
```

Bibliography

- [1] E Fernandez, F Pelayo, S Romero, M Bongard, C Marin, A Alfaro, and L Merabet. «Development of a cortical visual neuroprosthesis for the blind: the relevance of neuroplasticity». In: *Journal of neural engineering* 2.4 (2005), R1 (cit. on p. 1).
- [2] Bourne et al. «Trends in prevalence of blindness and distance and near vision impairment over 30 years: An analysis for the Global Burden of Disease Study». In: *The Lancet Global Health* 9 (Feb. 2021), e130–e143 (cit. on p. 1).
- [3] Ana Patricia Marques et al. «Global economic productivity losses from vision impairment and blindness». In: *EClinicalMedicine* 35 (2021), p. 100852 (cit. on p. 1).
- [4] Perkins school for the blind. *The visual pathway from the eye to the brain*. URL: <https://www.perkins.org/the-visual-pathway-from-the-eye-to-the-brain/> (cit. on p. 2).
- [5] Carlos Gustavo De Moraes. «Anatomy of the visual pathways». In: *Journal of glaucoma* 22 (2013), S2–S7 (cit. on pp. 2, 3).
- [6] Cleveland Clinic. *Retina*. URL: <https://my.clevelandclinic.org/health/body/22694-retina-eye> (cit. on p. 3).
- [7] Dr Melanie Gibson. *The Optic Nerve (CN II) and Visual Pathway*. URL: <https://teachmeanatomy.info/head/cranial-nerves/optic-cnii/> (cit. on p. 3).
- [8] Satya Mahesh Muddamsetty. «Spatio-temporal saliency detection in dynamic scenes using color and texture features». PhD thesis. Université de Bourgogne, 2014 (cit. on p. 3).
- [9] Louis Pizzarello et al. «VISION 2020: The Right to Sight: a global initiative to eliminate avoidable blindness». In: *Archives of ophthalmology* 122.4 (2004), pp. 615–620 (cit. on pp. 2, 3).
- [10] Paul Mitchell, Gerald Liew, Bamini Gopinath, and Tien Y Wong. «Age-related macular degeneration». In: *The Lancet* 392.10153 (2018), pp. 1147–1159 (cit. on p. 2).
- [11] Dyonne T Hartong, Eliot L Berson, and Thaddeus P Dryja. «Retinitis pigmentosa». In: *The Lancet* 368.9549 (2006), pp. 1795–1809 (cit. on p. 2).
- [12] Damianos Sakas, IG Panourias, BA Simpson, ES Krames, et al. «An introduction to operative neuromodulation and functional neuroprosthetics, the new frontiers of clinical neuroscience and biotechnology». In: *Operative neuromodulation* (2007), pp. 3–10 (cit. on p. 3).

- [13] Francisco Velasco. «Neuromodulation: an overview». In: *Archives of Medical Research* 31.3 (2000), pp. 232–236 (cit. on p. 4).
- [14] *Global Neuromodulation Devices Market Outlook 2021: Global Opportunity and Demand Analysis, Market Forecast to 2028*. 2022 (cit. on p. 4).
- [15] *Visual Prosthesis Market: Information By Type (Retina Implant Alpha AMS, Implantable Miniature Telescope, Argus II), By Indication, End User and Regional Outlook — Forecast Till 2026*. 2021 (cit. on p. 4).
- [16] Eduardo Fernandez. «Development of visual Neuroprostheses: trends and challenges». In: *Bioelectronic medicine* 4.1 (2018), pp. 1–8 (cit. on pp. 4, 5).
- [17] Eleonora Borda and Diego Ghezzi. «Advances in visual prostheses: engineering and biological challenges». In: *Progress in Biomedical Engineering* 4.3 (2022), p. 032003 (cit. on p. 4).
- [18] Soroush Niketeghad and Nader Pouratian. «Brain machine interfaces for vision restoration: the current state of cortical visual prosthetics». In: *Neurotherapeutics* 16.1 (2019), pp. 134–143 (cit. on p. 4).
- [19] Joseph M Kahn, Randy H Katz, and Kristofer SJ Pister. «Next century challenges: mobile networking for “Smart Dust”». In: *Proceedings of the 5th annual ACM/IEEE international conference on Mobile computing and networking*. 1999, pp. 271–278 (cit. on p. 5).
- [20] Dongjin Seo, Jose M Carmena, Jan M Rabaey, Elad Alon, and Michel M Maharbiz. «Neural dust: An ultrasonic, low power solution for chronic brain-machine interfaces». In: *arXiv preprint arXiv:1307.2196* (2013) (cit. on p. 5).
- [21] Sandro Carrara and Pantelis Georgiou. «Body dust: Miniaturized highly-integrated low power sensing for remotely powered drinkable cmos bioelectronics». In: *arXiv preprint arXiv:1805.05840* (2018) (cit. on p. 6).
- [22] Eduardo Fernández et al. «Visual percepts evoked with an intracortical 96-channel microelectrode array inserted in human occipital cortex». In: *The Journal of clinical investigation* 131.23 (2021) (cit. on pp. 6, 44).
- [23] Stuart F Cogan et al. «Neural stimulation and recording electrodes». In: *Annual review of biomedical engineering* 10.1 (2008), pp. 275–309 (cit. on pp. 8, 11, 13, 24).
- [24] Yo Han Cho, Young-Geun Park, Sumin Kim, and Jang-Ung Park. «3D electrodes for bioelectronics». In: *Advanced Materials* 33.47 (2021), p. 2005805 (cit. on pp. 9–13).
- [25] Christian Boehler, Diego M Vieira, Ulrich Egert, and Maria Asplund. «NanoPt—a nanostructured electrode coating for neural recording and microstimulation». In: *ACS applied materials & interfaces* 12.13 (2020), pp. 14855–14865 (cit. on p. 10).
- [26] Jeffrey Abbott et al. «A nanoelectrode array for obtaining intracellular recordings from thousands of connected neurons». In: *Nature biomedical engineering* 4.2 (2020), pp. 232–241 (cit. on p. 10).

- [27] Jisoo Yoo et al. «Long-term intracellular recording of optogenetically-induced electrical activities using vertical nanowire multi electrode array». In: *Scientific reports* 10.1 (2020), pp. 1–10 (cit. on p. 10).
- [28] David F Williams. «On the mechanisms of biocompatibility». In: *Biomaterials* 29.20 (2008), pp. 2941–2953 (cit. on p. 11).
- [29] M Alcaide, A Taylor, M Fjorback, V Zachar, and CP Pennisi. *Boron-Doped Nanocrystalline Diamond Electrodes for Neural Interfaces* (cit. on p. 11).
- [30] Kezhong Wang, Christopher L Frewin, Dorna Esrafilzadeh, Changchun Yu, Caiyun Wang, Joseph J Pancrazio, Mario Romero-Ortega, Rouhollah Jalili, and Gordon Wallace. «High-performance graphene-fiber-based neural recording microelectrodes». In: *Advanced materials* 31.15 (2019), p. 1805867 (cit. on p. 11).
- [31] Dong-Wook Park et al. «Graphene-based carbon-layered electrode array technology for neural imaging and optogenetic applications». In: *Nature communications* 5.1 (2014), pp. 1–11 (cit. on p. 11).
- [32] Gaëlle Piret et al. «3D-nanostructured boron-doped diamond for microelectrode array neural interfacing». In: *Biomaterials* 53 (2015), pp. 173–183 (cit. on p. 11).
- [33] Mohammad Reza Abidian and David C Martin. «Experimental and theoretical characterization of implantable neural microelectrodes modified with conducting polymer nanotubes». In: *Biomaterials* 29.9 (2008), pp. 1273–1283 (cit. on p. 12).
- [34] Eduardo Fernández and Pablo Botella. «Biotolerability of intracortical microelectrodes». In: *Advanced Biosystems* 2.1 (2018), p. 1700115 (cit. on p. 12).
- [35] Peikai Zhang, Nihan Aydemir, Maan Alkaisi, David E Williams, and Jadranka Travas-Sejdic. «Direct writing and characterization of three-dimensional conducting polymer PEDOT arrays». In: *ACS applied materials & interfaces* 10.14 (2018), pp. 11888–11895 (cit. on p. 12).
- [36] Hyunwoo Yuk, Baoyang Lu, Shen Lin, Kai Qu, Jingkun Xu, Jianhong Luo, and Xuanhe Zhao. «3D printing of conducting polymers». In: *Nature communications* 11.1 (2020), pp. 1–8 (cit. on p. 12).
- [37] Nina M Carretero, Mathieu P Lichtenstein, Estela Pérez, Laura Cabana, Cristina Suñol, and Nieves Casañ-Pastor. «IrOx-carbon nanotube hybrids: A nanostructured material for electrodes with increased charge capacity in neural systems». In: *Acta Biomaterialia* 10.10 (2014), pp. 4548–4558 (cit. on p. 12).
- [38] Laura Ferlauto, Antonio Nunzio D’Angelo, Paola Vagni, Marta Jole Ildelfonsa Airaghi Leccardi, Flavio Maurizio Mor, Estelle Annick Cuttaz, Marc Olivier Heuschkel, Luc Stoppini, and Diego Ghezzi. «Development and characterization of PEDOT: PSS/alginate soft microelectrodes for application in neuroprosthetics». In: *Frontiers in Neuroscience* 12 (2018), p. 648 (cit. on pp. 12, 21).
- [39] Lei He, Demeng Lin, Yanping Wang, Yinghong Xiao, and Jianfei Che. «Electroactive SWNT/PEGDA hybrid hydrogel coating for bio-electrode interface». In: *Colloids and Surfaces B: Biointerfaces* 87.2 (2011), pp. 273–279 (cit. on p. 12).

- [40] Brianna Thielen and Ellis Meng. «A comparison of insertion methods for surgical placement of penetrating neural interfaces». In: *Journal of neural engineering* 18.4 (2021), p. 041003 (cit. on pp. 14–17, 19).
- [41] Donald E Richardson and Huda Akil. «Pain reduction by electrical brain stimulation in man: Part 2: chronic self-administration in the periventricular gray matter». In: *Journal of neurosurgery* 47.2 (1977), pp. 184–194 (cit. on p. 14).
- [42] *Ad-Tech Medical Instrument Corporation 2021 Depth Electrodes*. URL: <https://adtechmedical.com/depth-electrodes> (cit. on pp. 14, 19).
- [43] *NeuroPace, Inc. 2021 NeuroPace RNS System*. URL: <https://www.neuropace.com/the-rns-system/> (cit. on pp. 14, 19).
- [44] Allison T Connolly et al. «Local field potential recordings in a non-human primate model of Parkinsons disease using the Activa PC+ S neurostimulator». In: *Journal of neural engineering* 12.6 (2015), p. 066012 (cit. on pp. 14, 19).
- [45] Kim J Burchiel, Shirley McCartney, Albert Lee, and Ahmed M Raslan. «Accuracy of deep brain stimulation electrode placement using intraoperative computed tomography without microelectrode recording». In: *Journal of neurosurgery* 119.2 (2013), pp. 301–306 (cit. on pp. 14, 19).
- [46] Jürgen Germann, Manuel Mameli, Gavin JB Elias, Aaron Loh, Alaa Taha, Flavia Venetucci Gouveia, Alexandre Boutet, and Andres M Lozano. «Deep brain stimulation of the habenula: systematic review of the literature and clinical trial registries». In: *Frontiers in Psychiatry* 12 (2021), p. 730931 (cit. on pp. 14, 19).
- [47] Andrew H Smith, Ki Sueng Choi, Allison C Waters, Amy Aloysi, Helen S Mayberg, Brian H Kopell, and Martijn Figee. «Replicable effects of deep brain stimulation for obsessive-compulsive disorder». In: *Brain Stimulation: Basic, Translational, and Clinical Research in Neuromodulation* 14.1 (2021), pp. 1–3 (cit. on pp. 14, 19).
- [48] Andrew B Schwartz, X Tracy Cui, Douglas J Weber, and Daniel W Moran. «Brain-controlled interfaces: movement restoration with neural prosthetics». In: *Neuron* 52.1 (2006), pp. 205–220 (cit. on pp. 15, 19).
- [49] Geon Hwee Kim, Kanghyun Kim, Eunji Lee, Taechang An, WooSeok Choi, Geunbae Lim, and Jung Hwal Shin. «Recent progress on microelectrodes in neural interfaces». In: *Materials* 11.10 (2018), p. 1995 (cit. on pp. 15, 19).
- [50] *Blackrock Microsystems 2018 Utah Array*. URL: <https://blackrockneurotech.com/research/products/> (cit. on pp. 16, 19).
- [51] Almut Branner, Richard B Stein, Eduardo Fernandez, Yoichiro Aoyagi, and Richard A Normann. «Long-term stimulation and recording with a penetrating microelectrode array in cat sciatic nerve». In: *IEEE transactions on biomedical engineering* 51.1 (2004), pp. 146–157 (cit. on pp. 16, 17).
- [52] Dongjin Seo, Ryan M Neely, Konlin Shen, Utkarsh Singhal, Elad Alon, Jan M Rabaey, Jose M Carmena, and Michel M Maharbiz. «Wireless recording in the peripheral nervous system with ultrasonic neural dust». In: *Neuron* 91.3 (2016), pp. 529–539 (cit. on pp. 18, 19).

- [53] Giuseppe Schiavone, Xiaoyang Kang, Florian Fallegger, Jérôme Gandar, Grégoire Courtine, and Stéphanie P Lacour. «Guidelines to study and develop soft electrode systems for neural stimulation». In: *Neuron* 108.2 (2020), pp. 238–258 (cit. on pp. 19, 25).
- [54] Rebecca A Frederick, I Yasmine Meliane, Alexandra Joshi-Imre, Philip R Troyk, and Stuart F Cogan. «Activated iridium oxide film (AIROF) electrodes for neural tissue stimulation». In: *Journal of Neural Engineering* 17.5 (2020), p. 056001 (cit. on pp. 44, 46).
- [55] Stuart F Cogan, Philip R Troyk, Julia Ehrlich, Timothy D Plante, and David E Detlefsen. «Potential-biased, asymmetric waveforms for charge-injection with activated iridium oxide (AIROF) neural stimulation electrodes». In: *IEEE Transactions on Biomedical Engineering* 53.2 (2006), pp. 327–332 (cit. on pp. 44, 46).
- [56] Atefeh Ghazavi, Jimin Maeng, Michael Black, Shreyas Salvi, and SF Cogan. «Electrochemical characteristics of ultramicro-dimensioned SIROF electrodes for neural stimulation and recording». In: *Journal of neural engineering* 17.1 (2020), p. 016022 (cit. on pp. 44, 46).
- [57] Felix Deku, Alexandra Joshi-Imre, Alket Mertiri, Timothy J Gardner, and Stuart F Cogan. «Electrodeposited iridium oxide on carbon fiber ultramicroelectrodes for neural recording and stimulation». In: *Journal of The Electrochemical Society* 165.9 (2018), p. D375 (cit. on p. 44).
- [58] Douglas McCreery, Albert Lossinsky, Victor Pikov, and Xindong Liu. «Micro-electrode array for chronic deep-brain microstimulation and recording». In: *IEEE transactions on biomedical engineering* 53.4 (2006), pp. 726–737 (cit. on p. 44).
- [59] Sheryl R Kane, Stuart F Cogan, Julia Ehrlich, Timothy D Plante, Douglas B McCreery, and Philip R Troyk. «Electrical performance of penetrating microelectrodes chronically implanted in cat cortex». In: *IEEE Transactions on Biomedical Engineering* 60.8 (2013), pp. 2153–2160 (cit. on pp. 44, 46).
- [60] Stuart F Cogan, Julia Ehrlich, Timothy D Plante, and Rick Van Wagenen. «Penetrating microelectrode arrays with low-impedance sputtered iridium oxide electrode coatings». In: *2009 Annual International Conference of the IEEE Engineering in Medicine and Biology Society*. IEEE. 2009, pp. 7147–7150 (cit. on p. 46).